Niobia-silica and silica membranes for gas separation

Vittorio Boffa

Chairman:	Prof. G. J. Vancso	University of Twente
Promotor:	Prof. D. H. A. Blank	University of Twente
Assistant promotor:	Dr. J. E. ten Elshof	University of Twente
Members:	Prof. K. Kuroda	Waseda University
	Prof. L. Lefferts	University of Twente
	Prof. E. Montoneri	Università di Torino
	Prof. M. Wessling	University of Twente
Referent:	Dr. J. Vente	ECN

The research described in this thesis was carried out in the Inorganic Material Science group at the University of Twente and has been financially supported by stw (Dutch Technology Foundation), project number 790.36.030.

Niobia-silica and silica membranes for gas separation,
Ph.D. thesis, University of Twente, The Netherlands
ISBN 978-90-365-2636-4

Printed by PrintPartners Ipskamp, The Netherlands

NIOBIA-SILICA AND SILICA MEMBRANES FOR GAS SEPARATION

DISSERTATION

to obtain
the degree of doctor at the University of Twente,
on the authority of the rector magnificus,
prof.dr. H.W.M. Zijm,

on account of the decision of the graduation committee,
to be publicly defended
on Friday the 22nd of February at 16.45

by

Vittorio Boffa

born on the 22nd of October 1978

in Chieri, Italy

The dissertation is approved by the promotor Prof. dr. ing. D.H.A. Blank
and the assistant promotor Dr. ir. J.E. ten Elshof

Summary

This thesis describes the development of ceramic membranes suitable for hydrogen separation and CO_2 recovery from gaseous streams. The research work was focused on the three different parts of which gas-selective ceramic membranes are composed, i.e., the microporous gas-selective silica layer, the mesoporous interlayer and the macroporous support.

Very high retention of CO_2 was achieved by introducing Nb^{5+} ions in the microporous silica framework of the silica top layer. Niobia-silica membranes were fabricated by coating an asymmetric γ-alumina disk with a niobia-silica polymeric sol prepared from metal alkoxide precursors. The sol had a Nb : Si molar ratio equal to 0.33. The film was fired at 500 °C. Generally, the permeance of the gases in this membrane decreased steadily with molecular size. Helium and hydrogen showed thermally activated transport through the membrane. The permeance of carbon dioxide deviated strongly from the general trend and was more than 5 times lower than the permeability of SF_6. The interaction of CO_2 with the pores was studied by ATR-FTIR on a thin film, and is probably due to a relatively strong interaction between Nb-bound hydroxyl groups and CO_2. The promising results obtained with this membrane initiated further optimization of its microstructure.

Small angle X-ray scattering (SAXS) analysis of different niobia-silica sols showed that the fractal dimension (D_f) of the sol particles increased as a function of time, to remain constant at an upper value equal to 1.9, when tetraethyl orthosilicate (TEOS) is used as silica source. The gyration radius (R_g) of these sols grew proportionally to $t^{0.5}$. For this reason a diffusion limited growth mechanism was proposed. Dilution and moderate reaction temperatures can be employed to slow down the reaction rate in order to

control the size of the particles more precisely. Sols with higher Nb : Si molar ratios showed a higher degree of condensation. This is due to the higher reactivity of the niobia precursors compared to TEOS. Higher growth rates were measured for sols with higher water contents. The concentration of acid can also promote the growth rate of polymeric particles, especially in the early stages of synthesis when a reaction limited growth mechanism cannot be excluded.

Disk membranes were prepared from two of the sols studied by SAXS, and the resuting permeabilities were compared with that of the first niobia-silica membrane. This indicated that less developed sols have a tendency to penetrate into the pores of the support, which yields membranes with a high resistance even to small gases like helium and hydrogen. A strong decrease of helium pearmeance was also observed when the Nb : Si ratio in the sol was increased from 0.33 to 0.8. This is probably due to the higher density of the material with the highest Nb loading.

A tubular niobia-silica membrane was prepared by coating the outer part of an alumina support. Despite a certain amount of defects on the membrane surface, the hydrogen and helium ideal selectivities of the tubular membrane towards other gases were higher than the selectivity of the support. Hence, although the coating procedure could be optimized further, there are indications that Nb / Si oxide membranes could find applications in real separation modules.

The hydrothermal stability of niobia-silica membranes was investigated and compared with the stability of pure silica membranes by exposing them to 0.56 bar of steam for 70 h at 150 and 200 °C. Single gas permeation experiments were performed before and after these treatments. The results showed that both membranes were densified by steam exposure. However, the decrease of helium and hydrogen permeability was less marked for niobia-silica than for pure silica.

The second part of research was focused on the development of novel mesoporous interlayers, with the aim of improving the hydrogen permeance of this membrane component. It was shown that a surfactant-containing

polymeric sol of silica nanoparticles, could be coated on an α-alumina support with 80-90 nm larges pores, simply by varying its rheological properties. The deposition method allowed the preparation of a templated silica membrane directly on macroporous α-alumina in a facile way. Some penetration of silica particles into the α-alumina support was encountered, and they prepared layers were equally permeable to hydrogen as γ-alumina. It was shown that doping of the silica phase with about 2-3 mol% Zr increased the hyrothermal stability of the mesoporous silica phase considerably.

In the final part of the thesis a method is presented to employ silicon nitride microsieves with hexagonally ordered 500-1000 nm wide perforations as highly permeable support for silica-based membranes. Due to the high perforation density and the low effective thickness of the sieve (~ 1 μm), the resistance of this type of support to gas flow is negligible. The challenge was to cover the perforations with a thin self-standing templated mesoporous silica film. A transfer technique was developed to transfer the preformed silica film onto the microsieve. A sacrificial polymeric layer was used to cover the inside of the perforations and ensure a smooth support surface for the silica film. No penetration of the silica film into the perforations was observed. The method allows to overcome the conventional stacked-layers architecture of ceramic membranes, which is also common in gas selective membranes. This novel method can in principle be used for all kinds of materials and can be exploited in a large number of applications: sensing, microreactors, microfluidic devices, etc. The thin layers that were prepared according to this method do not permit selective gas separation yet, due to the presence of a small number of defects. However, the mesoporous nature of the film, and the absence of a high concentration of macroscopic defects was demonstrated by selective liquid-phase ion transport experiments.

Samenvatting

Dit proefschrift beschrijft de ontwikkeling van keramische membranen voor scheiding van kleine gassen als waterstof en kooldioxide (CO_2) uit gasstromen. Er is getracht de permeabiliteit en hydrothermale stabiliteit van deze membranen te verhogen, en hun selectiviteit voor verschillende gassen te beïnvloeden. Het onderzoek richtte zich daartoe op alle onderdelen waaruit gasscheidingsmembranen worden opgebouwd, nl. de silica toplaag, de mesoporeuze tussenlaag en de drager.

De microporeuze silica membranen bleken een zeer hoge retentie voor CO_2 te vertonen indien Nb^{5+} in de microporeuze silica fase aanwezig was. Deze niobia-silica membranen werden gemaakt door een γ-alumina membraan te coaten met een polymeer niobia-silica sol, dat op zijn beurt was gemaakt uit metaal-alkoxide precursors. De permeabiliteit van het membraan nam af naarmate de kinetische diameter van de gasmolekulen toenam van 2.6 Å (He) tot 5.5 Å (SF_6). Uitzondering op deze trend vormde CO_2 (3.3 Å), dat een zes maal lagere permeabiliteit had dan werd verwacht op basis van zijn grootte. Infrarood onderzoek toonde aan dat dit waarschijnlijk het gevolg is van een relatief sterke interactie tussen Nb-OH groepen en CO_2.

Small angle X-ray scattering (SAXS) analyse van verschillende solen wees uit dat de deeltjes een vertakte polymere structuur hebben, en dat de mate van vertakking toeneemt naarmate er meer niobium aanwezig is. Op basis van het SAXS onderzoek konden ontwerpregels worden opgesteld waarmee grootte en mate van vertakking van de solen tijdens de synthese gecontroleerd kunnen worden.

Kleine solen hadden tijdens het coaten de neiging om weg te zakken in de onderliggende mesoporeuze γ-alumina laag. Dit resulteerde in membranen met

een hoge transportweerstand. Indien de deeltjes groot genoeg waren om niet in de mesoporiën te kunnen penetreren, trad dit effect niet meer op. Langdurige blootstelling aan hydrothermale omstandigheden (150-200°C, 0.56 bar stoom) toonde aan dat de mate van verdichting van de microstructuur van microporeus silica minder werd als er niobium in het materiaal aanwezig was, m.a.w. de ontwikkelde niobia-silica membranen zijn hier structureel beter tegen bestand dan puur silica.

Het tweede onderdeel van het onderzoek was gericht op de ontwikkeling van een nieuwe mesoporeuze tussenlaag, met als doel de totale permeabiliteit van waterstof te verhogen t.o.v. op γ-alumina gebaseerde systemen. Hiertoe werd een mesogestructureerd mesoporeus silica sol met de juiste rheologische eigenschappen ontwikkeld, om depositie in dunne lagen op een macroporeuze drager van α-alumina mogelijk te maken. Tevens werd aangetoond dat toevoeging van 2-3 mol% Zr aan de mesoporeuze silica fase een grote verbetering van de hydrothermale stabiliteit te zien gaf.

In het laatste deel van het proefschrift wordt een methode gepresenteerd om de macroporeuze drager te vervangen door silicium nitride microzeven met heaxgonaal geordende perforaties van 0.5-1.0 μm diameter. Vanwege de hoge dichtheid aan perforaties, en de minimale dikte van de zeven (~1 μm) vertonen deze een vrijwel verwaarloosbare weerstand tegen gasstroming. De uitdaging was om een zeer dunne, 50-200 nm dikke, mesoporeuze silica film over de perforaties heen te leggen, zonder dat enige penetratie van de silica fase in de perforaties optrad. Dit bleek mogelijk met een speciaal hiertoe ontwikkelde transfer techniek. De selectiviteit van de resulterende membranen is aangetoond door experimenten met selectief ionentransport in water.

Table of contents

CHAPTER 1

General introduction

1.1. Context

The increasing public concern about climate change and international agreements demanding cuts in CO_2 emissions [1] highlights the importance of technologies which enable separation of CO_2 from gaseous streams and eventually capture it into geological formations.

These technologies can be of interest for the treatment of post-combustion gases of power plants [2], exploitation of traditional gases resources [3] like oil and natural gas fields, the development of renewable energy sources such as biogases [4] and the gradual transition towards the so-called hydrogen economy [5]. For instance, before being stored and used, hydrogen needs to be separated from the reaction mixture by which it is formed. Since hydrogen is mainly produced from hydrocarbons by steam reforming (SR) or catalytic partial oxidation (CPO), followed by the water-gas-shift (WGS) reaction, as depicted in Figure 1.1, the separation H_2/CO_2 is of key importance.

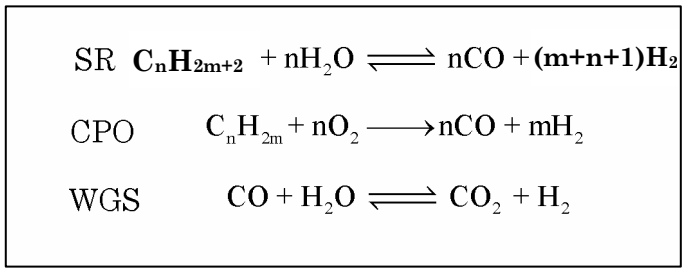

Figure 1.1. Hydrocarbon conversion to hydrogen by SR (steam reforming), CPO (catalytic partial oxidation) and WGS (water-gas-shift).

The separation of CO_2 from gaseous streams containing hydrogen or hydrocarbons can be attained by physical adsorption, chemical reaction, cryogenic recovery, or a membrane process [6]. At present, absorption is the most commonly used approach. However, membrane separation is also a promising technology, because it can be applied to continuous processes, it is energy efficient and easy to upscale or to employ in mobile applications.

The work described in this thesis was carried out in the framework of the STW (Dutch Technology Foundation) project number 790.36.030. The aim of the project was to develop a reactor concept to convert CPO gas to WGS. This included catalyst development and membrane development. The general idea behind this project is a two step process system to convert gasoline to hydrogen onboard of a car. The two step process follows the scheme CPO + WGS, as illustrated in Figure 1.1. First the gasoline is partially oxidized to carbon monoxide. Then, in a second step, this gas mixture is allowed to react with steam yielding carbon dioxide and hydrogen. Hydrogen is produced in both steps. A membrane is needed to separate the hydrogen from the gas mixture of the WGS reactor, in order to supply a pure H_2 feed to the fuel cell.

1.2. Aim of the thesis

This thesis concerns membranes. A membrane is defined by IUPAC as "a structure, having lateral dimension much greater than its thickness, through which mass transfer occurs under a variety of driving forces" [7]. This is the most general definition about membranes. However this description does not include the main function of a membrane. Membranes are prepared for separating things. Membrane processes are characterized by the fact that the feed flow is divided in two streams called the retentate and the permeate [7]. The permeant is what passes through the membrane; the stream containing the permeant that leaves a membrane module is called permeate. The retentate is the stream that has been separated from the permeant by the membrane [7].

The aim of this thesis is to develop membranes for CO_2 separation, for separation of large amount of gaseous strems, eventually enable to recover hydrogen in a WGS membrane reactor.

Thus such membranes have to satisfy two requirements:

1. they must to be highly permeable to hydrogen in order to reduce the size of the separation steps.

2. they must be stable under working conditions.

Based on these two requirements we focused our attention on the development of ceramic membranes. Indeed truly organic materials cannot be applied because of the high temperatures that must be reached inside the reactor. Also metallic dense membranes are not functional because of their low permeability. For these reasons porous ceramic membranes become indispensable for industrial applications.

1.3. The architecture of an inorganic ceramic membrane

Ceramic membranes for gas separation are asymmetric systems consisting of a α-alumina support, a γ-alumina intermediate layer and a thin silica top-layer. This structure is illustrated in Figure 1.2. The function of the support is to confer a high mechanical strength to the membrane. As support for the membranes presented in this thesis generally were used 2 mm thick disks, which can withstand many bars of pressure. The average diameter of the pores in such supports is 80-100 nm.

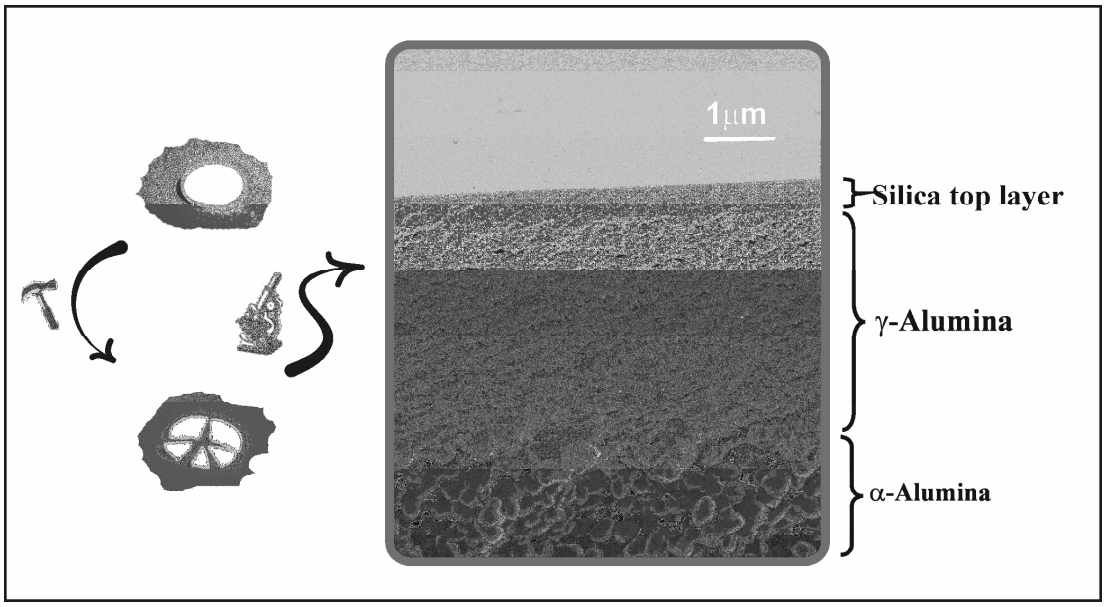

Figure 1.2. Pictures and SEM magnification of a ceramic microporous gas-sieving disk.

The top layer of the membrane can be thinner than 100 nm and its pores are

smaller than 0.5 nm. This is the gas selective layer, which has to be applied on top of the α-alumina support. However the particles of the polymeric silica sol are far smaller than the pores of the support. Thus an intermediate layer is required. For this reason, we deposited a coating of a boehmite sol, which consists of particles of about 40 nm [10]. By calcining this film at 600 ºC, a γ-alumina layer with an average pore size of about 5 nm is obtained [11].

According to IUPAC, pores with widths exceeding 50 nm are called macropores; mesopores have widths between 50 nm and 2 nm and, if a pore has a width less than 2 nm, it is called a micropore [12]. Thus the disks that we used as substrate are macroporous supports, the γ-alumina phase is a mesoporous material and the gas selective silica film is a microporous top layer. In this thesis we will often make use of these terms, which are part of the jargon of membrane science.

1.4. Selective or permeable?

The efficiency of membranes is generally described in terms of permeance and selectivity.

Selectivity is quantitatively expressed by the separation factor (α):

$$(1.1)\ \alpha = \frac{x_{retentate}}{y_{retentate}} \cdot \frac{y_{permeate}}{x_{permeate}}$$ [12].

In the case of a gaseous mixtures, x and y are the partial pressures of the two components X and Y. The permeance (F) expresses how easy a membranes is crossed by the permeate. F [$mol \cdot m^{-2} \cdot s^{-1} \cdot Pa^{-1}$] is defined as the transport flux per unit of trans-membrane overpressure [12].

$$(1.2)\ F_a = \frac{J_a}{\Delta P_a},$$

where J_a is the flux of the species "a" across the membrane and ΔP_a is the difference in partial pressure of "a" between the two sides of the membrane. Using this parameter it is possible to compare data recorded at different pressures, assuming that the flow changes linearly with the overpressure. This assumption is valid for microporous membranes, as it will be demonstrated in

the second chapter of this thesis, where the different gas transport mechanisms that can occur in a membrane will be discussed.

The selectivity of a membrane in the separation of a binary mixture is often reported as the ratio of the two permeances:

$$(1.3)\ F_{a/b} = \frac{F_a}{F_b}.$$

This ratio is called ideal selectivity or permselectivity. For commercial applications a combination of high selectivity and high permeation is required. In other words it is necessary to have a good separation and at the same time to reduce the size (the cost and the space) of the membrane.

Unfortunately extremely high values of the separation factor can be obtained only for membranes with a really low permeance and *vice versa*. To better understand this issue one should think about two limiting cases: the pores are several times larger than the gas molecules (mesopores) or the pores have exactly the same size of the permeating gas molecules (molecular sieving). In the first case, large pores do not pose a large resistance (1/F) to gas flow. On the other hand, only a Knudsen-type separation is possible in this regime (see Chapter 2, 3 and 7); in the case of a mixture of carbon dioxide and hydrogen the maximum separation factor is only 4.7. On the other hand, if the pores are of the same size as the permeating gas molecules, the membrane works as a sort of yes-no filter with a very well defined cut-off. Nevertheless, at the same time the interactions between gas molecules and walls of the pores are so strong that the permeance decreases dramatically. Furthermore, molecules with a larger kinetic diameter can block the pores, reducing the permeate flux further.

The resistance of a membrane can be reduced by decreasing its thickness. However it is really difficult to coat extremely thin membrane without defects. Microporous silica membranes prepared via sol-gel can be as thin as 30 nm [14]. In summary, separation and permeation are two opposing requirements; therefore an optimal compromise has to be reached [15].

1.5. Hydrothermal stability of ceramic membranes

For being commercially applicable, membranes have to be stable under working conditions for the longest possible time, at least for few years. Because the final calcination of the membrane occurs at 400-600 °C, thermal resistance is not an issue. The major problem concerning the durability of a ceramic membrane is the chemical resistance [13]. The presence of steam at high temperature can, indeed, deteriorate the membrane. Because this thesis deals with membranes enable to separate hydrogen from carbon dioxide in WGS conditions, stability to steam is an important feature. Since we are dealing with an asymmetric three-layer system, we should consider three materials. α-Alumina is a inert substance, obtained by calcination of alumina powder at temperatures higher than 1100 °C [16]. It is well known that α-alumina can withstand harsher conditions than WGS.

The γ-alumina layer is formed by calcining at 600 ºC an aerogel obtained from a boehmite sol. The surface of γ-alumina is covered by a large number of hydroxyl groups, which increase the affinity of this material for polar substances such as water. It is well known that this material is chemically unstable, for instance at pH below 3 [17]. The hydrothermal instability of γ-alumina had also been demonstrated [10]. Despite the fact that doping with La is an affective solution for increasing the stability of γ-alumina [10]. Furthermore, γ-alumina can be replaced altogether by other mesoporous materials, such as doped or undoped zirconia and titania [17, 18].

Hence the chance to apply a ceramic membrane to reactions such as steam reforming and WGS depends on the stability window of the gas-selective top layer. Despite that amorphous dense silica is a extremely stable medium (crystallization does not occur below 1100 °C [19]), microporuos amorphous silica shows partial densification already during calcination. Thus the challenge here is not the intrinsic chemical stability of the material, but the stability of the microporous structure. In the presence of steam, microporous silica undergoes dramatic structural changes of the porous structure already at 180 °C [20]. Fotou et al. [21] tested the durability of microporous silica (pore

diameter around 0.6 nm, and a BET surface area of about 600 m^2 g^{-1}) in a 1:1 steam/air mixture at atmospheric pressure. They reported a substantial reduction of surface area after 30 h at 600°C, and complete densification at 800 °C.

Nam and Gavalas [22] studied the thermal and hydrothermal stability of hydrogen selective silica membranes that had been made by chemical vapour deposition (CVD). They noticed a reduction of H_2 permeance after high temperature exposure in wet nitrogen (440 °C, 0.04 bar). After the treatment, the permeance of nitrogen had increased, with a corresponding decrease of H_2/N_2 selectivity. According to Nam and Gavalas, the densification creates uneven shrinkage in the material which can result in the formation of "microcracks". The flux of hydrogen in these cracks is negligible compared to its diffusion through the microporous material, which is undergoing densification. On the contrary, the increase of the flux of nitrogen depends essentially on the formation of these defects. They also observed that the reduction of hydrogen flux is substantial at the beginning of the exposure, while it becomes negligible after five days. The selectivity of the membrane was further reduced by heating at 600 °C and 700 °C in wet nitrogen.

On the contrary, in the study of De Lange [23], the reduction of hydrogen permeance as a consequence of steam exposure was not always associated with a decrement of selectivity of the membrane. De Lange monitored the stability of unsupported and supported microporous silica membranes and reported densification both after thermal and steam aging. For unsupported porous materials calcination above 400 °C resulted in a strong reduction of porosity (calculated from the N_2 adsorption isotherm), with complete densification at 800 °C. The stability of the supported material to steam was tested in argon at 40 °C (60% relative humidity) and at 250 °C (with a steam partial pressure of 0.017 bar). After these treatments the hydrogen permeance decreased, but the H_2/hydrocarbon separation factor was not necessary lower due to the hydrothermal aging.

We can conclude that, in principle, the densification of the microporous structure due to hydrothermal aging is not necessarily negative for the

separation factor of a microporous membrane. Nevertheless, microcracks can be formed during the structural rearrangements of the material, yielding a less selective membrane. While the densification of the microporous material occurs to a large extent at the beginning of the exposure to steam, microcrack formation is an unpredictable event. It depends on a large number of variables, such as water concentration, temperature, film preparation, etc. The drop of selectivity of a microporous membrane can also occur after a few days of exposure to steam.

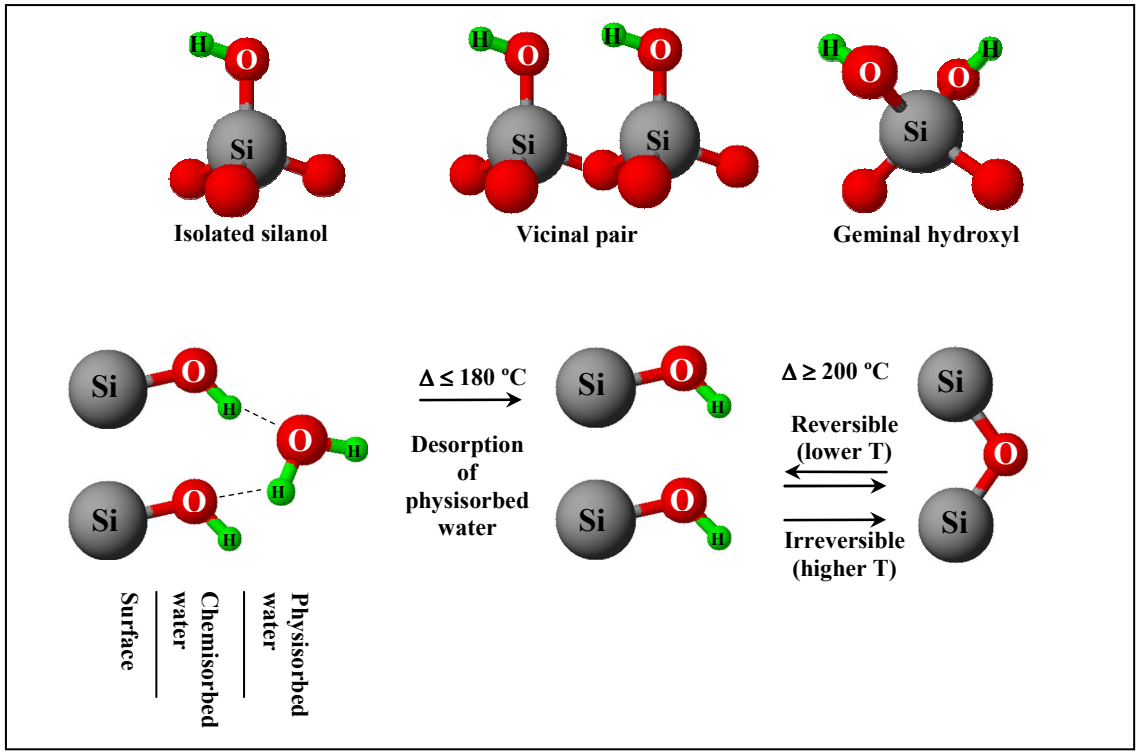

Figure 1.3. Interactions of water with the silica surface at different temperatures.

The hydrothermal instability of microporous silica is generally ascribed to its hydrophilic nature, which depends on the presence of hydroxyl groups on its surface. This was proved by Giessler et al. [24], by monitoring the structural changes of templated and non-templated silica after hydrothermal treatment by ^{29}Si-NMR. They reported that "hydrotreatment of silica-derived materials shows large structural collapse for samples that contain a high contribution of silanols groups, which promote hydrophilicity [24]." Thus, in order to understand the hydrothermal degradation process, it is necessary to focus on

the interaction of the silica surface with water molecules. At room temperature the silica surface is covered by chemisorbed and physisorbed water. These two different interactions of water with silica surface are shown in Figure 1.3.

Chemisorbed water corresponds to the presence of hydroxyl (OH) groups on its surface; physically adsorbed water is hydrogen-bonded to these groups. Silanol groups can be isolated, vicinal or geminal. By heating it is possible to selectively remove first the physically adsorbed water (weakly bound) and then the OH groups that are chemically bound to silica. Thermogravimetric analysis (TGA) can be used for the quantitative measurement of physically and chemically adsorbed water. Physisorbed water desorbs in the range from 105 to 180 °C, depending on pore size [25]. Upon heating above 200 °C it is possible to remove most of the chemically bonded hydroxyls from the silica surface. At 1000 °C hydroxyls are still present, but at a large distance from one another (2.3 nm [25]). The disilanolisation is to a certain extent a reversible process; but the higher is the calcination temperature, the harder the silanol groups will reform after cooling [25].

Silica structural modification under hydrothermal conditions can be explained according to the process described in Figure 1.4, which was originally proposed by Himai et al. [20].

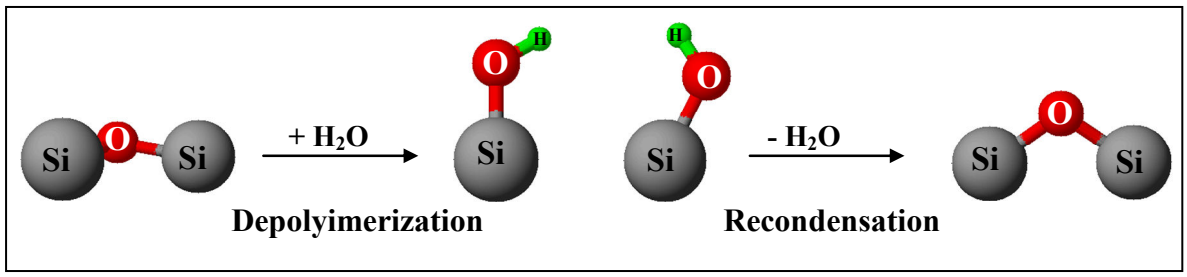

Figure 1.4. Densification mechanism under hydrothermal conditions.

Weak bonds can be broken by interaction with steam, creating vicinal hydroxyl pairs [26], which are subject to recondensation due to the high temperature. This mechanism, which consists of the cyclic destruction and reconstruction of the Si-O-Si network, confers flexibility to the material. Eventually, it can reorganise itself in the most stable state: dense glass.

A more elaborate study on the hydrothermal modification of silica was done by

Leboda and Mendyk [27]. They focused their study on mesoporous silica, measuring structural changes of the material after hydrothermal treatment with steam and with liquid water at different pH. As working hypothesis, they considered mesoporous silica as a packing of spherical dense particles. Their results suggest the same mechanism as reported in Figure 1.4. According to Leboda and Mendyk the hydroxylation of silica ends in a real depolymerization process. During steam exposure, silicic acid dissolves in the thin film of water that is covering the material. The depolymerisation of silica is comparable to a dissolution process. Such process occurs fastest on the areas with the greatest convex curvature [27], such as small particles or rough particles. The dissolved silicic acid is free to migrate through the sorbed water layer until, due to saturation, it precipitates and repolymerizes with the silica matrix. The repolymerization of dissolved silica occurs essentially in the regions with smaller curvature, like in the proximity of larger particles or at the contact point between two particles. The growth of larger particles at the expense of smaller ones leads to a denser material with larger pores. This picture, proposed by Leboda and Mendyk for silica, can be extended to other mesoporous materials, but with a different intensity. The densification process due to the hydrothermal curing can be compared to a sintering process. Indeed, as with sintering, the effect of hydrothermal treatment of a mesoporous material is a reduction of the pore volume and an increase of the average pore size.

We expect that this process is more prominent in microporous silica, where the pores have larger curvature than in mesoporous silica and they are already filled by water, even at small steam partial pressures. In the case of a material with pores smaller than 0.5 nm, as the silica used for the preparation of gas-selective membranes, the dissolution/repolymerization process described above will lead to a completely dense material. Indeed, in this case, the porosity is not due to packing of dense particles, but it is an intrinsic property of the material. The pores have a size close to the length of a Si-O bond, and the migration of silicic acid will eventually lead to complete occlusion of micropores.

Stabilisation of the microporous silica network can be achieved by introducing transition metal ions in the silica network. These metals usually have coordination numbers larger than silicon, which has a coordination number equal to 4. Asaeda et al. [28] obtained highly resistant membranes by incorporating up to 50 mol% ZrO_2 in microporous silica. Such membranes are often less selective than pure silica, and it is not clear if the dopant is completely mixed with silica or is confined in nanodomains after calcination. Similar results have been obtained with other dopants, like Ni [29] and Al [21].
The hydrothermal stability of microporous silica can be also increased by reducing its affinity to water molecules. This can be done by decreasing the density of hydroxyl groups on the silica surface by calcination at high temperatures. De Vos [30] compared the permeability and selectivity of silica membranes after calcination at 400 °C and 600 °C. Membranes calcined at 600 °C had hydrogen permeances of about four times smaller than the ones calcined at 400 °C; but they were also more selective and stable.
If the main objective is to supply a costumer with a stable product, membranes can be fired in humid environment. This approach was followed by Yoshida et al. [32], who fired zirconia-silica membranes in controlled conditions (50% steam/air for 15 min. at 570 °C). After this treatment the samples showed a larger resistance to reaction with steam, but also the typical characteristics of hydrothermaly aged membranes: low permeability and low selectivity.
Both thermal treatment and steam firing lead to a more stable product that does not vary its performance in hydrothermal environments. Nevertheless, membranes prepared in this way are always characterized by no very large permeate fluxes.
The affinity to water in microporous membranes can be reduced by introducing hydrophobic moieties into the silica matrix. De Vos et al. [33] were the first to prepare microporous silica membranes containing methyl groups that were covalently bonded to the inorganic matrix. This material was obtained by the simultaneous reaction of MTES (metyltriethyl orthosilicate) with TEOS (tetraethyl orthosilicate). Compared to standard silica membranes, the organic-inorganic membranes showed a lower selectivity towards hydrogen,

but a similar permeance and higher hydrothermal resistance than pure silica. So far the highest degree of incorporation of organic groups in a microporous silica matrix has been achieved by Sah [34], who prepared microporous membranes for pervaporation only from organosilane precursors: 1,2-bis(triethoxysilyl)ethane (BTESE) and MTES. These membranes showed a higher stability than normal silica under the conditions at which water/n-butanol pervaporation is performed. Unfortunately these membranes were not thermally stable at temperatures higher than 250 °C, while those prepared by De Vos are potentially applicable up to 500 °C.

Organic moieties can be introduced in the silica membranes also by treating standard inorganic membranes with organosilanes that react with the silanol groups present on the silica surface. This grafting reaction can occur in gas phase [35] or in solution [36]. Hydrophobic γ-alumina mesoporous membranes were prepared by immersing them in a solution of alkylclorosilanes (R_XSiCl_{4-X}) in toluene [37]. These post-treated membranes are more affine to organic permeants, like drugs and polymers Thus they can potentially be applied in a large number of industrial processes. The organosilane molecules are too bulky to penetrate inside micropores of gas selective membranes. Thus it is not possible to hydrophobise the internal pore surface of a microporous material by post-treatment. Despite that, organosilanes can be applied on top of a silica layer in order to decrease the water permeability of the membrane and, consequently, the concentration of water inside the gas selective layer. Nevertheless it is questionable if they can act as an affective barrier against water penetration into the microporous structure [38].

In conclusion, despite the variety of paths that have been proposed in literature to stabilize microporous silica, the hydrothermal instability of porous silica is still a limiting factor in the development of microporous membrane reactors for processes involving steam at high temperature. Among the solution described above, doping with transition metal ions appears to be the most promising path to stabilize a microporous silica membrane. This route will be pursued in the chapters of this thesis.

1.6. Outline of the thesis

To develop a novel ceramic sieve for carbon dioxide sequestration, stable and highly permeable to hydrogen it was necessary to focus the research work on the different layers which compose an asymmetric membrane. For this reason after a brief introduction in Chapter 1 and Chapter 2, this thesis is structured in three sections concerning each of the three layers, which were shown in Figure 1.2. Form Chapter 3 to Chapter 6 the development of niobia-silica microposorous membranes is exposed. In Chapter 3 the strategy beyond the preparation of this new material is explained. Chapter 4 and Chapter 5 illustrate respectively the development of niobia-silica sols and membranes; while Chapter 6 deals with the hydrothermal stability of this new material. A new way of coating mesoporous templated silica layer is illustrated in Chapter 7, and Chapter 8 will be dedicated to the stability of the mesoporous materials. Chapter 9 is dedicated to a novel technique for the preparation of self-standing thin layers.

1.7. References

[1] UNFCCC (United Nations Framework on Climate Change), 1997 UNFCCC (United Nations Framework on Climate Change), 1997. The Kyoto Protocol to the Convention on Climate change, available at http://unfccc.int/resource/docs/convkp/kpeng.pdf.

[2] O. Bolland, P. Mathieu, Energy Conversion Manage, 1998, 39, 1653.

[3] B.D. Bhide, S.A. Stern, J. Membrane Sci., 1993, 81, 209.

[4] M. Röhr, R. Wimmerstedt, Desalination, 1990, 77, 331.

[5] D.R. Simbeck, Energy, 2004, 29, 1633.

[6] R. Bredesen, K. Jordal, O. Bolland, Chem. Eng. and Process, 2004, 43, 1129.

[7] W.J. Koros, Y.H. Ma, T. Shimidzu, Pure Appl. Chem., 68 (1996) 1479.

[8] Twigg MV, Catalyst Handbook (2nd ed), London: Wolfe Press, 1989 Chapter 6.

[9] A.F. Ghenciu, Curr. Opin. Solid State Mater. Sci. 6 (2002) 389.

[10] A. Nijmeijer, H. Kruidhof, R. Bredesen, H. Verweij, J. Am. Ceram. Soc. 84 (2001) 136.

[11] R.S.A. de Lange, J.H.A. Hekkink, K. Keizer, A.J. Burggraaf, J. Membr. Sci. 99 (1995) 57.

[12] K.S.W. Sing, D.H. Everett, R.A. W. Haul, L. Moscou, R.A. Pierotti, J. Rouquerol, T. Siemieniewska, Pure Appl. Chem., 57 (1985) 603.

[13] S. Giessler, L. Jordan, J. C. Diniz da Costa, G.Q. Lu, Sep. Purif. Technol. 32 (2003) 255.

[14] R.M. de Vos, High-selectivity, High-flux Silica Membranes for Gas Separation, PhD thesis, University of Twente, Enschede, 1998.

[15] A.J. Burggraaf, L. Cot, Fundamentals of Inorganic Membrane Science and Technology, Elsevier, Amsterdam, 1996.

[16] R.A. van Santen, P.W.N.M. van Leeuwen, J.A Moulijn, B.A. Averill, Catalysis: an Integrated Approach (2nd Ed.), Elsevier, Amsterdam, 1999, p 440-441.

[17] T. Van Gestel, C. Vandecasteele, A. Buekenhoudt, C. Dotremont, J. Luyten, R. Leysen, B. Van der Bruggen, G. Maes, J. Membr. Sci. 207 (2002) 73.

[18] J. Sekulic, A. Magraso, J.E. ten Elshof , D.H.A. Blank, Micropor. Mesopor. Mater. 72 (2004) 49.

[19] R. K. Iler, "The Chemistry of Silica", John Wiley and Sons, New York, 1979.

[20] H. Himai, H. Morimoto, A. Tominaga and H. Hiraschima, J. Sol-Gel Sci., 10 (1997) 45.

[21] G.P. Fotou, Y. S. Lin and S. E. Pratsinis, J. Mater. Sci. 30 (1995) 2803.

[22] S.W. Nam, and G.R. Gavalas, AIChE Symp. Ser., 85 (1989) 68.

[23] R.S.A. de Lange, K. Keizer, A.J. Burggraaf, Ind. Eng. Chem. Res. 34 (1995) 3838.

[24] S. Giessler, J.C. Diniz da Costa, G.Q. Lu, J. Nanosci. Nanotech. 1 (2001) 331.

[25] L. T. Zhuravlev, Colloids Surf. A, 173 (2000) 1.

[26] T. Bakos, S.N. Rashkeev, S. T. Pantelides, Phys. Rev. Lett. 88 (2002) 055508.

[27] R. Leboda, E. Mendyk, Mater. Chem. Phys. 27 (1991) 189.

[28] M. Asaeda, Y. Sakou, J.H. Yang, K. Shimasaki, J. Membr. Sci. 209 (2002) 163.

[29] M. Kanezashi, M. Asaeda, J. Membr. Sci. 271 (2006) 86.

[30] R.M. de Vos, H. Verweij, Science 279 (1998) 1710.

[31] H. Tada and H. Nagayama, Langmuir 11 (1995) 136.

[32] K. Yoshida, Y. Hirano, H. Fujii, T. Tsuru and M. Asaeda, J. Chem. Eng. Jpn., 34 (2001) 523.

[33] R.M. de Vos, W.F. Maier and H. Verweij J. Membr. Sci., 158 (1999) 277.

[34] A.Sah, Chemically Modified Ceramic Membranes – Study of Structural and Transport Properties, PhD thesis, University of Twente, Enschede, 2006.

[35] R.P. Singh, J.D. Way, K.C. McCarley, Ind. Eng. Chem. Res. 43 (2004) 3033.

[36] C. Picard, A. Larbot, F. Guida-Pietrasanta, B. Boutevin, A. Ratsimihety, Sep. Purif. Technol. 25 (2001) 65.

[37] A. Sah, H.L. Castricum, A. Bliek, D.H.A. Blank, J.E. ten Elshof, J. Membr. Sci. 243 (2004) 125.

[38] H. Tada, H. Nagayama, Langmuir 11 (1995) 136.

CHAPTER 2

Theoretical background

Abstract:

A general description of the preparation and the characterization of porous ceramic membrane is presented. Sol synthesis, membrane fabrication, characterization techniques and gas transport are the main topics of this chapter.

Nomenclature of Chapter 2

η	Dynamic viscosity [mPa·s]	γ_s	Gas-solid interfacial tension [J·m^{-2}]
τ	Torque [%]	M	Molecular mass [g·mol^{-1}]
u	Cylinder velocity [rad^{-1}]	$\bar{\upsilon}$	Average molecular velocity
E_k	Kinetic energy [eV]	P_m	Average pressure [Pa]
E_b	Binding energy [eV]	L	Membrane thickness [m]
h	Plank constant [eV·s]	μ_p	
ν	Angular frequency [s^{-1}]	E_a	Apparent activation energy of permeance [kJ·mol^{-1}]
R	Gas constant [J·mol^{-1}·K^{-1}]		
T	Temperature [K]	E_m	Mobility energy of the permeant [kJ·mol^{-1}]
r_K	Kelvin radius [nm]		
l_t	t-layer thickness [nm]	Q_{st}	Isosteric heat of adsorption [kJ·mol^{-1}]
V_{mol}	Molar volume [m^3·mol^{-1}]	D	Diffusion coefficient [m·s^2]
ε	Porosity	J	Transmembrane flux [mol·m^{-2}·s^{-1}]
τ_{memb}	Tortuosity	J_o	flux at T = ∞ [mol·m^{-2}·s^{-1}]
Φ	Flux [mol·s^{-1}·m^{-2}]	θ	Contact angle of the condensed phase on the pore wall [rad]
A_{tot}	Total area [m^2]		

2.1. Sol-gel chemistry

A sol is a stable suspension of particles within a fluid matrix [1]. The particles of a suspension can be dense bodies, with dimensions up to microns, or can be small clusters, containing only tens or hundreds of metal atoms. The first type of suspension is called colloidal sol; the second is named polymeric sol. The γ-alumina interlayer is obtained form a colloidal sol; on the contrary the microporous silica layer can be only prepared from a polymeric sol. Colloidal sols are usually prepared in aqueous media, while polymeric sols are synthesized in alcoholic solutions by hydrolysis and condensation of alkoxide precursors.

Some considerations about the stability of sols are required. Particles or clusters can aggregate or react with each other. This process is driven by the Van der Waals attractive forces or by bond formation between unreacted groups. As a result the particles grow in time, leading eventually to precipitation of larger aggregates, or to the formation of a tri-dimensional network. During the development of this network the viscosity of the sol

increases and at a certain point the system behaves like a solid. This point is called the "gel point" and the system after this moment is called a gel [1].

Sols can be stabilized by repulsive forces such as the mutual repulsion among particles of the same charge, which can provide the sol with a resistance to aggregation. Often sols are stabilized by adding an acid. This stabilization of a sol is called peptization.

For preparing ceramic membranes it is necessary to start form stable sols. When a thin film of the sol is deposited on top of a porous support, part of the solvent evaporates and part is drained by the pores. The removal of the solvent results in gel formation on top of the support. After complete removal of the solvent by heating, a porous structure is obtained. Such structure is an inorganic membrane.

Since this thesis concern the development of polymeric sols, a short description of the chemistry of such systems will be presented here. In particular way the chemistry of the alkoxysilanes will be treated, because of the fact that microprous silica is the most common material for the preparation of gas

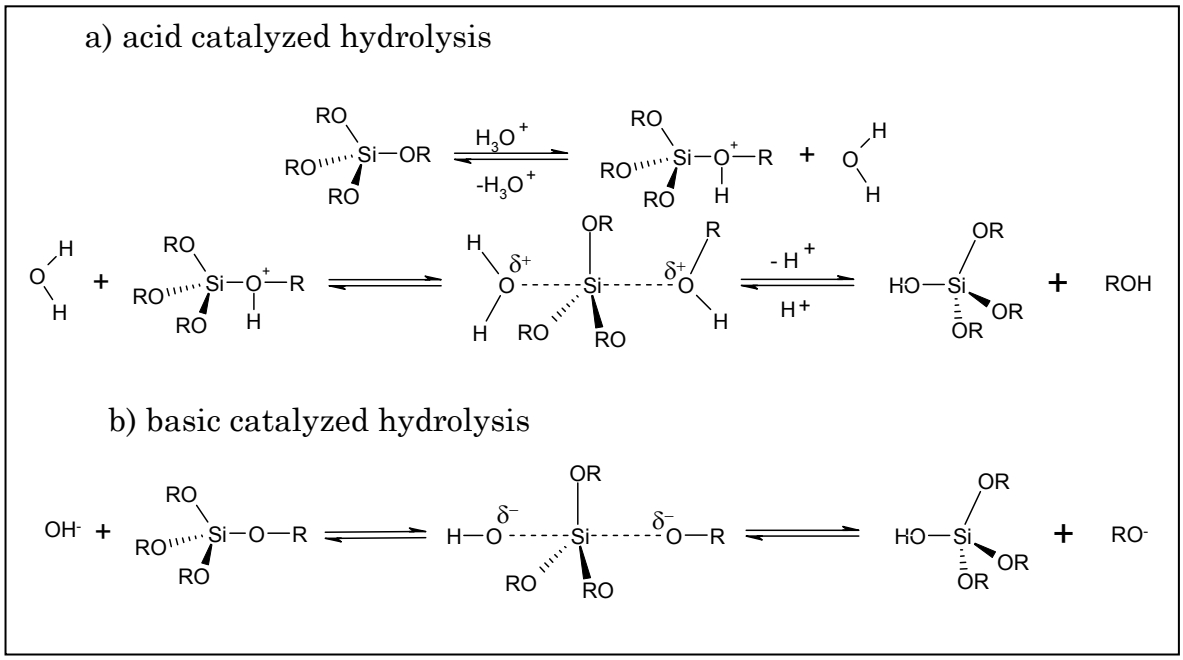

selective ceramic membranes.

Figure 2.1. Hydrolysis of a generic silicon alkoxide in basic and acid conditions.

In presence of water a metalorganic precursor, usually tetraethylorthosilicate (TEOS), reacts following the schemes shown in Figure 2.1 and Figure 2.3. At first it undergoes hydrolysis, which can be catalyzed by an acid or a base. Both mechanisms are shown in Figure 2.1. Under acidic conditions first a leaving group is formed by protonation, then the precursor is hydrolyzed by nucleophilic attack of water. The breakdown of the Si-O-R bound and the formation of a new Si-O-H bond are synchronized, as proved by the experiments of Baker [2] and Corriu [3] on chiral silanes. In chemistry this mechanism is catalogued as a bimolecular nucleophilic substitution: S_N2 [4]. Under basic conditions the hydrolysis occurs via an analogous mechanism; but in this case with the formation of a negatively charged transition state.

In a nucleophilic substitution (S_N) both steric and inductive effects play a role. The more the metal centre is accessible to the attack of a nucleophile, the faster is the reaction. Thus the hydrolysis is faster in presence of small and linear alkoxyl chains, as shown in Figure 2.2.

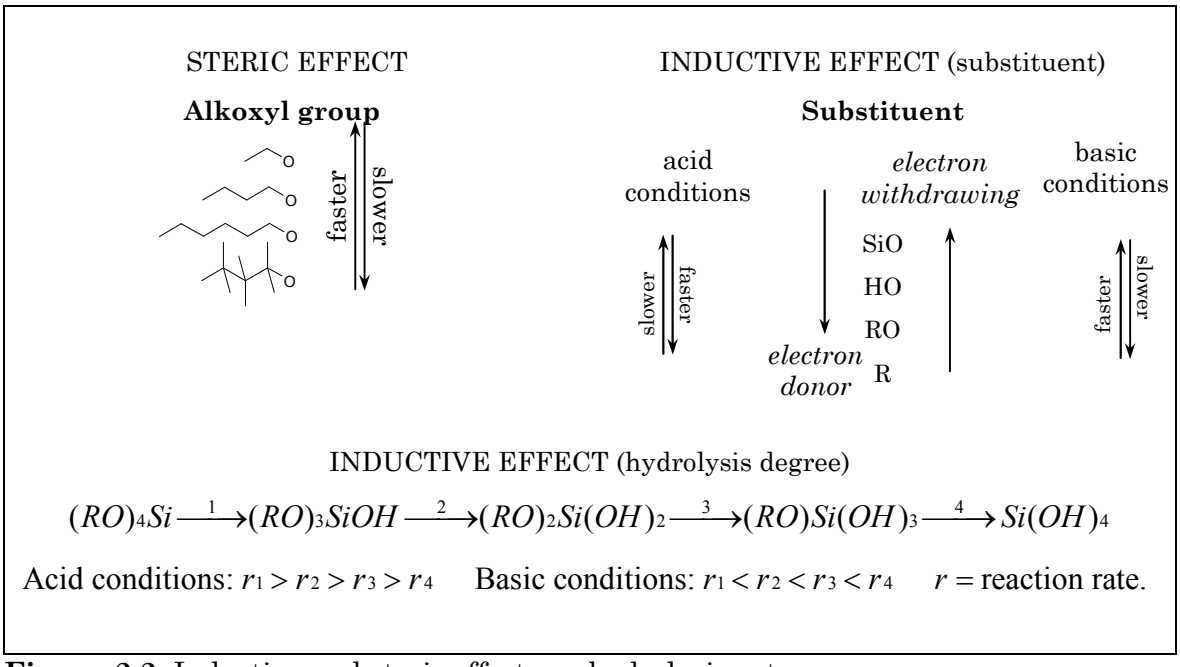

Figure 2.2. Inductive and steric effects on hydrolysis rate.

In organic chemistry manuals S_N2 reactions are reported to be only slightly affected by the inductive effect of the substituents [5], because there is no

formal charge on the centre undergoing substitution. Despite that, the inductive effects of the groups on the silicon were made evident by Schmidt [6]. This thesis will follow the description given by Brinker [7], who considered the hydrolysis of metal alkoxides as a S_N2 influenced by the inductive effect of the substituents.

In acid catalysed hydrolysis the positive transition state is stabilized by the presence of an alkoxy group (electron donor) on the silicon. Therefore the reaction is faster for those species that still have more alkoxy groups on the metallic centre (Figure 2.2). Under basic conditions the transition state is negatively charged. In this case the hydroxyl groups (electron withdrawing) stabilize it, hence the opposite behaviour is observed. Schmidt [6] studied also the reaction rate of $(CH_3)_X(C_2H_5O)_{4-X}Si$, where "x" can be 1, 2 or 3. Under acidic conditions the hydrolysis rate increases with "x" (more positive charge on the central metal). In basic solution the alkyl groups destabilize the intermediate state and the reaction speed decreases.

The reverse reaction of the hydrolysis is the esterification of the silanol. Usually the alcohol corresponding to the alkyl substituents is chosen as solvent, in order to avoid transesterification reaction and consequently a change in the composition of the precursor. In the case of TEOS, which is the most commonly utilized silica precursor, ethanol is used as solvent.

Condensation occurs with water or alcohol elimination, as described in Figure 2.3. The charge intermediate state is formed by protonation (acidic conditions) or deprotonation (basic catalysed reaction). The isoelectric point of the silicic acid, is about pH=2-2.2 [8], hence the term "base catalysed" mechanism is referred to any pH above 2. That implies also that the smallest condensation rate occurs around pH 2-3 [6], when the silicic acid is uncharged. The following formation of Si-O-Si bond is the slow step. Also in this case the inductive effect of the substituents plays a role. Under basic conditions the fully hydrolyzed species undergo the fastest condensation reactions. As a consequence highly cross-linked large particles are obtained and, in the end, materials with large pore sizes. On the contrary at low pH linear or slightly branched polymeric chains are obtained; the packing of these chains leads to

the formation of pores with widths smaller than 1 nm in the consolidate material. Hence these conditions are indispensable for the preparation of microporous silica.

Condensation reaction

Water Condensation:

$$Si(OEt)_3OH + HOSi(OEt)_3 \rightleftharpoons (OEt)_3SiOSi(OEt)_3 + H_2O$$

Alcohol Condensation:

$$Si(OEt)_3OR + HOSi(OEt)_3 \rightleftharpoons (OEt)_3SiOSi(OEt)_3 + ROH$$

Condensation mechanism

Acid conditions:

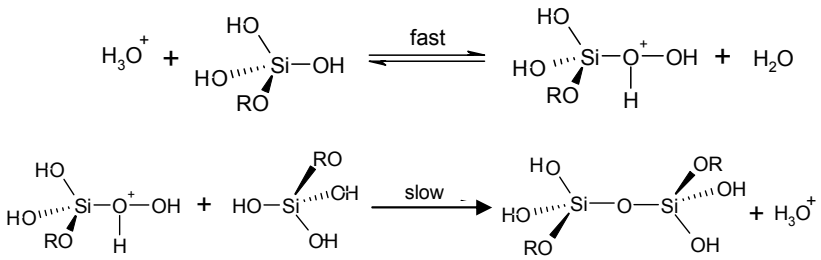

Basic conditions:

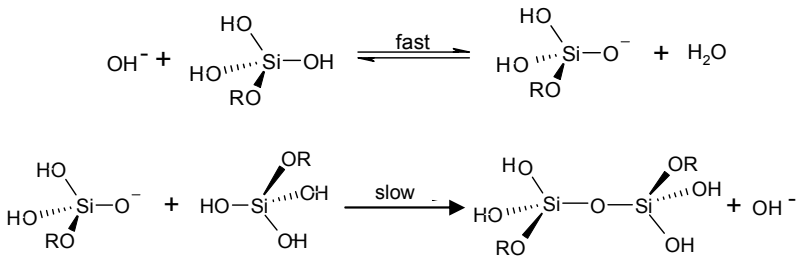

Figure 2.3. Condensation reaction and mechanism for pH below 2 (acid catalyzed hydrolysis) and above 2 (basic catalyzed hydrolysis).

In spite of its lack of chemical stability at high pH and in hydrothermal conditions, silica is still far the most used material in the preparation of gas-selective ceramic membranes. A first reason for that is the high stability of the amorphous phase of silica, which hardly undergoes crystallization below 1100 °C. Indeed amorphism is a desired property for preparing materials with

pores smaller than one nanometer. A second reason is the high reactivity of transition metal precursors, which requires extremely controlled reaction conditions. Although alkoxides of transition metals have a chemistry similar to the TEOS, their hydrolysis and condensation reactions are much faster than for silicon alkoxides. Indeed, while the rate constant for acid hydrolysis of TEOS was calculated to be $5.1 \cdot 10^2$ $mol^{-1} \cdot s^{-1} \cdot [H^+]^{-1}$ [9], the hydrolysis reactions of transition metal alkoxides are so violent that it is difficult to measure their rate constant in a precise way. This can be explained on the base of the data reported in Table 2.1. The partial charge on silicon is about half than those present on the other metals. Consequently silicon is less disposed to undergo nucleophilic attack than the other metal centers. The unsaturation, which is a tendency of the complexed metal to coordinate with other ligands, is zero in the case of silicon, and has a positive value for the other tetraalkoxides metals. This is explained by the fact that silicon has an empty d-shell [10]. Alkoxides of metal with higher unsaturation number are more inclined to interact with water molecules and thus to undergo hydrolysis. For this reason Ti, Zr and other transition metal precursors are more prone to hydrolysis than TEOS.

The tendency to crystallize at relatively low calcination temperatures and the difficulty to synthesize stable polymeric sols in the nanometer region, make the preparation of transition metals membrane a big challenge. Microporous membranes of titania [11] and zirconia [13] have been fabricated; but up to now they have shown permeabilities and selectivities for gases that are much lower than those of pure silica membranes. Enhanced stability, without paying a too high price in terms of selectivity and permeabiltity, was rather achieved with doped silica membranes [12].

Table 2.1. Partial charge and unsaturation on tetraethoxyde metals.

Complex	Partial charge (δ)	Cation	Coordination number (N)	Unsaturation number (N-4)
$Si(OR)_4$	0.32	Si^{4+}	4	0
$Ti(OR)_4$	0.63	Ti^{4+}	6	2
$Zr(OR)_4$	0.65	Zr^{4+}	7	3

2.2. Membrane preparation

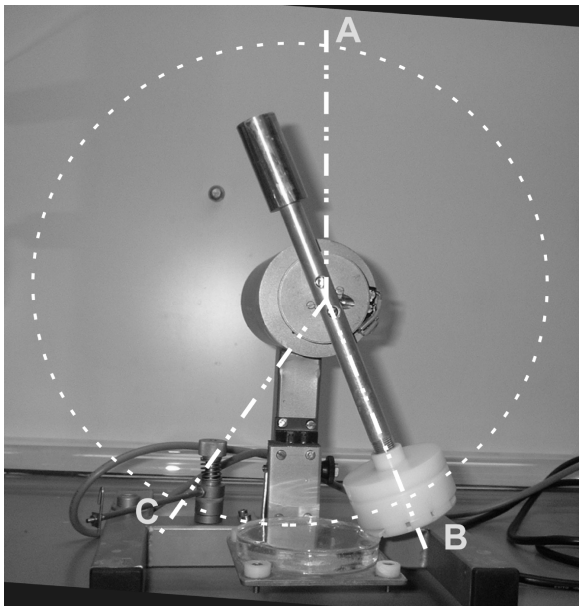

Figure 2.4. Dip-coating machine: the membrane is fixed on top of a mechanic arm, which is rotated by a small engine. During the rotation the membrane is dipped in the sol lying in the petry dish on the base of the machine.

The data reported in this thesis concern membranes obtained by coating of a sol onto a flat support. These supports were prepared by colloidal filtration of a commercial α-alumina powder (AKP30, Sumitomo, Tokyo, Japan) [14]. 140 g of AKP-30 was added to 140 ml of 0.02 M aqueous nitric acid. After being sonicated for 15 minutes, this dispersion was filtered on a metallic grid with about 0.2 mm large meshes in order to remove eventual aggregates. Then this colloidal suspension was poured in cylindrical plastic moulds (∅ 42 mm), about 20 ml suspension in each mould. The water was removed from the suspension trough a polyester filter (pore size 0.8 μm, Schleicher & Shuell, Dassel, Germany) placed on the bottom of the mould and using a vacuum pomp. After drying at room temperature overnight, the green supports were calcined at 1100 °C (heating/cooling rates of 2 °C/min). Flat disks of 39 mm diameter and 2.0 mm thickness were obtained after cutting and polishing. The final porosity of these supports was about 30% and the average pore size was in the range of 80-120 nm [15]. So prepared supports were checked by optical analysis. If scratches or other defects were visible, the polishing procedure was repeated; otherwise they were used as substrate for the deposition of a γ-alumina layer.

Mesoporous γ-alumina membranes were prepared via dip-coating of the α-alumina supports in a boehmite sol, using the setup sown in Figure 2.4. The sol was synthesized by adding, under vigorous stirring, aluminium-tri-sec-

butoxide (Merck, Darmstadt, Germany) to double-distilled water at 96 °C. The molar ratio aluminum oxide precursor/water was 1/140. The ethanol formed by the hydrolysis of the metal alkoxide was removed by evaporation; then the mixture was cooled down to 60 °C. The volume of evaporated solvent was partially replaced by adding water to obtain a 0.5 M suspension. The sol was peptized by adding concentrated nitric acid till a pH equal to 2.8 was reached, followed by refluxing for 20 h. The final product was a homogeneous boehmite sol. In general, an organic binder needs to be added to colloidal sols to enhance the viscoelastic properties of the dried film and thus inhibit cracks formation. For this reason a 30g/l solution of polyvinyl alcohol (Merck, M_W = 72000 g/mol) in 0.5 M nitric acid was added to the sol before coating.

The coating procedure followed the steps shown in Figure 2.4. First the membrane was clamped on top of the mechanic arm, which at this stage is in position A. Then the arm was rotated by a small motor with an angular speed of 0.2 rad·s^{-1} till the membrane reached the boehmite sol at position B. At this point the rotating speed of the arm was decelerated to 0.06 rad·s^{-1} and the support was dipped in the boehmite sol. At point C the angular speed was increased again to 0.2 rad·s^{-1} and the arm was rotated until the original vertical position A had been reached. After 1 minute the membrane was removed from the dipping machine and dried for 3 h in a climate chamber (Heraeus Votsch, Hanau, Germany) at 40 °C and 60% relative humidity. The thus prepared membranes were calcined in a muffle furnace for 3 h at 600 °C (heating/ cooling rate of 1 °C/min). The coating procedure was repeated once more to cover pin holes and/or small defects formed during the first coating. A similar coating procedure was used to obtain gas selective top-layers.

2.3. Characterization of porous membranes

The quantitative description of porous materials is not a trivial issue. Indeed any obtained parameters are closely connected to the technique that was used to acquire them. For instance nitrogen sorption detects all accessible pores of a

material, both the interconnected pores and those with a dead-end. On the contrary, in permporometry analysis only the pores that are actively used for transport are measured.

If a technique involves the use of probe molecules, there will be always some pores with a width smaller than the molecular size of the probe. Those pores cannot be detected and are called inaccessible or latent pores. This problem is relevant in the assessment of microporosity. Indeed the smallest molecules, which are helium and hydrogen have extremely low critical pressures and temperatures and cannot be used as vapour. This precludes their use to a limited amount of techniques. In addition the interaction solid-gas in microporous systems is so complex that cannot be described with simple models. Indeed those models, which consider matter as a continuum, cannot be applied at all, because all sorption sites must be taken in account explicitly. Complex equations, which are applicable only in a small range of experimental conditions and under a large number of assumptions, are required.

Furthermore, because membranes are extremely thin films with a certain roughness, it is extremely difficult to characterize them. For this reason a part of the characterization is done on powders, under the assumption that bulk material and thin film, prepared from the some sol, have the same properties. In most of the cases this assumption is inaccurate. Indeed solvent evaporation in a drying thin film is fast and the perturbing effect of the support is not negligible. On the contrary, when powders are prepared via sol-gel by evaporation of few milliliters of solvent in a beaker, the drying time is several hours and inhomogeneities can be formed during this time. In addition the draining effect of the pores can cause a difference between the chemical composition of the thin film and the starting sol.

Despite these shortcomings, bulk methods are commonly used next to surface methods and permeation methods to accomplish a full characterization of inorganic membranes. In this section only standard techniques largely used in materials science will be discussed.

Rheology

A sol with good rheological properties is a prerequisite for obtaining a defect-free layer after coating. The rheology of a sol can be investigated by using machines named rheometers. The simplest rheometer is the Ostwald glass viscometer, which consists of a glass bulb connected with a capillary. By measuring the time required for a polymeric solution to empty the bulb trough the capillary under its own hydrostatic pressure, it is possible to calculate the viscosity of the solution [20].

Other instruments consist of a sample holder and a spindle. Holder and spindle can have different shapes and dimensions depending on the sample that is to be measured. In a typical measurement the spindle is rotated within a fluid. The friction exerted by the fluid against the spindle is measured as function of the angular speed. Viscosity can by calculated according the equation:

(2.1) $\eta = K_1 \cdot \frac{\tau}{u}$ [21].

For Newtonian fluids K_1 is a constant depending on the geometry, weight and dimensions of the spindle. For non-Newtonian fluids, K_1 can be a function of shear rate and time.

Scanning Electron Microscopy (SEM)

Electron microscopy is an extremely important tool in materials science. It gives us the possibility to observe the morphology of particles or composite structures, like a stacked membrane, with a resolution of few nanometers [16].

In SEM a narrow electron beam scans the sample surface, while secondary and back scattered electrons are detected. The contrast in a SEM image is derived from the variation of detected intensity depending on the position of the beam. For instance two layers with different atomic composition can be distinguished, because the heavier elements are more efficient scatters and appear brighter in the image. Also grains in a homogeneous medium can be

observed. This is possible because surface patches orthogonal to the electron beam yield higher brightness than the oblique ones.

Gas sorption

Nitrogen sorption is probably the most widely used technique for characterizing porous materials. In a typical measurement the weight or the volume of nitrogen vapour sorbed on a solid at different relative pressures is monitored. The result of a sorption measurement is a sorption isotherm. A sorption isotherm is the plot, at constant temperature, of the equilibrium amount of nitrogen vapour sorbed by a porous system as a function of relative pressure. In general both adsorption and desorption isotherms are measured. Also other vapours can be used such as argon, carbon dioxide and acetylene. Recently also water has been used for the characterization of microporous carbons [17] and silica [18].
From the study of a sorption isotherm it is possible to determine pore size distribution, surface area and porosity of a material.

X-ray photoelectron spectroscopy (XPS)

This is a surface technique that allows quantitative determination of the chemical composition of a surface. Briefly, in XPS an X-ray source generates photons, which ionize the atoms of the sample, producing ejected free electrons. The kinetic energy of the ejected electrons is:
(2.2) $E_k = h\upsilon - E_b$ [19],
where $h\nu$ is the energy of the incoming photon and E_b is the binding energy of the electron. Since the binding energy is different for electrons in different orbitals or in different atoms, the kinetic energy of the ejected electrons can reveal the elemental composition of a sample. A typical XPS scan is conducted in high vacuum and the number of emitted photoelectrons is plotted as a function of their kinetic energy. From the relative intensity of the different peaks it is possible to quantitatively measure the elemental composition of a surface.

The binding energy of an electron is also function of the state of the atom, thus XPS can also be used to asses the different oxidation states of an atom in a material. A plasma etcher can be used during XPS analysis and the atomic composition as a function of the dept can be measured.

Permporometry

Permporometry is an effective technique for determining the pore size distribution of a mesoporous layer on a macroporous support, and to check if defects in the layer are absent. In short, two incondensable gases (nitrogen and oxygen) are injected at the two sides of the membrane. During the measurement some of the pores are selectively blocked by condensed vapour (typically cyclohexane, but also other probes can be used). The pore size in which capillary condensation can still occur is expressed as function of the relative cyclohexane pressure by the Kelvin equation [22]:

(2.3) $\ln P_r = -\frac{\gamma_s V_{mol}}{RT}\frac{1}{r_k}\cos\theta$,

where θ is normally considered to be equal to zero. For each relative pressure all pores with radii smaller than the threshold value r_k are blocked by the condensed vapour. At a relative pressure of 1 all pores of the membrane are filled and gas transport trough the membrane is not possible when no macroscopically large defects and cracks are present. When the vapour pressure is reduced, pores with a size larger than r_k are emptied and become available for gas transport. During the experiment the pressure at both sides of the membrane is kept equal to 1 bar, so that no pressure gradients are present in the system. Assuming that all pores are cylindrical and parallel, and the Knudsen equation, which is reported on page 32 is valid, the density function is expressed as:

(2.4) $n(r_k) = -\frac{3}{4}\frac{\tau_{memb} L A_{tot}}{r_k^3}\sqrt{\frac{RTM}{2\pi}}\left(\frac{\Delta F_{acc}}{\Delta r}\right)$.

This equation was applied for calculating the pore size distributions of the membranes presented in this thesis. r_k is the Kelvin radius of the pore, which

does not correspond to the actual pore radius. To obtain the real pore radius it must to be corrected by adding the thickness of the cyclohexane monolayer, which forms on the surface of the pores before capillary condensation occurs [23]. This layer is generally called t-layer and in this thesis it is indicated as l_t. The l_t thickness can be estimated from the oxygen permeation rate at low cyclohexane pressure and generally has a value of about 0.4 nm [23]. The actual pore diameter d_p can be calculated by summing l_t to r_k:

(2.5) $d_p = 2(r_K + l_t)$.

Examples of permporometry analyses of mesoporous materials are presented in Chapters 7 and 8.

Single gas permeation

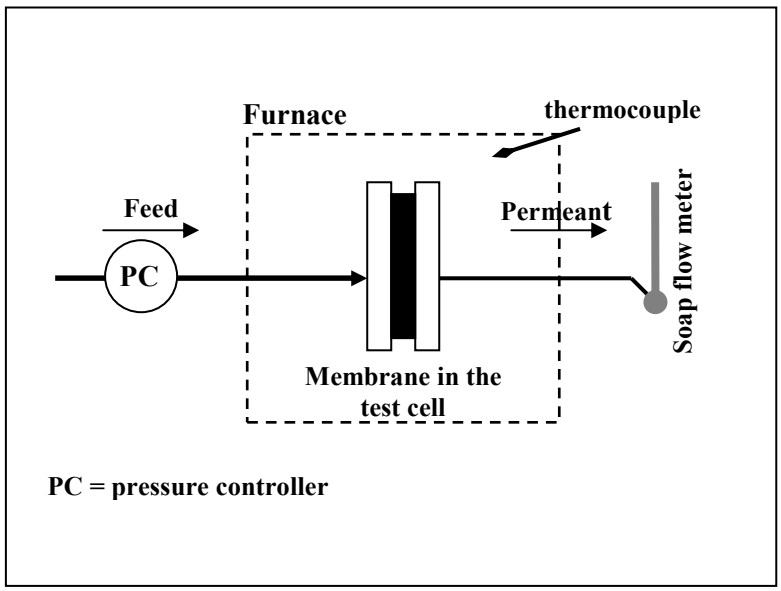

Figure 2.5. Scheme of the gas permeation set-up used for single gas permeation experiments.

The gas permeance of prepared membranes was measured by using the set-up schematically shown in Figure 2.5. The gas flow was measured with a soap film flow meter which allowed monitoring a large range of flows with high accuracy. Since atmospheric water can condense in the pores of the silica matrix, all membranes were dried at 200 °C in a hydrogen flow for at least 16 h before measurements were done. In a typical series of measurements, the permeation rate of different gases was determined starting from the one with the smaller kinetic diameter and equilibrating for a few hours after a new gas had been introduced into the set-up. With this simple

set-up it is possible to study the dependency of the permeance by the temperature and to estimate the main pore size of a membrane by measuring the permeability of a sequence of probe molecules with increasing kinetic diameter, as will be shown in Chapter 3, on page 44 and 46.

2.4. Transport phenomena in porous materials

Gas transport in porous materials occurs according to different mechanisms, depending on the size and shape of the pores. In macropores the mean free path of a molecule is far smaller than the pore diameter. Thus a gas molecule has a higher chance to collide with another gas molecule than with the pore wall. This regime, which is called viscous flow regime, is described by the Poiseuille law:

(2.6) $J_{viscous} = \frac{\varepsilon \mu_p \bar{r}^2}{8\eta} \frac{P_m}{RT} \frac{\Delta P}{L}$ [24].

The Poiseuille law is a general rule that is verified for macroscopic phenomena, such as the flux of a liquid in a pipe. In the viscous regime no gas separation is possible.

On the contrary in mesopores the mean free path of a gas molecule is larger than the size of the pore. The interaction gas molecule-pore wall is therefore more important than the interaction molecule-molecule. In this case the transport occurs following the Knudsen law:

(2.7) $J_{Knudsen,a} = \frac{2}{3} \bar{\upsilon}_a \frac{\varepsilon r}{\tau RT} \frac{\Delta p_a}{L}$ [24],

where υ_a is the mean molecular velocity of a species "a" in a pore of radius r. According to the kinetic theory of ideal gases:

(2.8) $\bar{\upsilon}_a = \sqrt{\frac{8RT}{\pi M_a}}$ [25].

Therefore, assuming that the pressure gradient is constant across the membrane, the gas flux of species "a" in a mesoporous medium is expressed by Equation 2.9.

(2.9) $J_{Knudsen,a} = K_{Knud}\sqrt{\frac{1}{M_a RT}}\frac{\Delta p_a}{L}$.

While in the viscous regime the flux is a function of the total gas pressure, in the Knudsen regime it is proportional to the gradient of partial pressure across the membrane. According to Equation 2.9 the flux across a mesoporous material is inversely proportional to the square root of the molecular mass of the permeating species. Thus molecules with different molecular mass can be separated by Knudsen diffusion. From Equation 1.3 and Equation 2.9 we obtain:

(2.10) $F_{Knudsen,a/b} = \sqrt{\frac{M_b}{M_a}}, \quad M_b > M_a$

The first application of ceramic membranes in an industrial process was the separation of uranium isotopes by Knudsen diffusion [26]. In this process $^{235}UF_6$ was separated from $^{238}UF_6$. The ideal separation factor for this process is extremely small, equal to 1.0064; therefore a cascade of steps is required for obtaining the desired degree of enrichment. From Equation 2.10 it is possible to calculate the ideal selectivity of microporous membranes for many other pairs of gases. An industrially relevant separation, for instance, is the removal of CO_2 from hydrogen, toward which mesoporous membranes offer an ideal selectivity equal to 4.69 only.

Microporous membranes have been developed in order to achieve more efficient gas separations than are obtained in the Knudsen regime. Separation of gas molecules with microporous membranes occurs mainly thanks to the sieving effect of the pores. Molecules with a kinetic diameter larger than the pores of the membrane cannot permeate trough. An ideal separation factor H_2/CO_2 higher than 10^2 was obtained by De Vos with pure silica membranes [27]. In separations according to Knudsen transport and molecular sieving, molecules are considered as spheres with defined dimensions and weight. The chemical properties are not considered, despite the fact that in micropores the interaction of gas molecules and ceramic walls is even stronger than in the Knudsen regime.

The transport in a microporous medium can be described as a surface diffusion mechanism; consequently the general Fick law can be applied:

(2.11) $J = -D\frac{dC}{dz}$ [28]

Equation 2.11 for a microporous membrane can be written as:

(2.12) $J_a = -J_{0,a}\exp\left\{-\frac{E_a}{RT}\right\}\frac{\Delta P}{L}$ [29].

E_a is the apparent activation energy. The E_a value is empirically estimated for each species measuring the temperature dependence of permeance. E_a can be positive or negative and it is considered as sum of two contributions: the isosteric heat of absorption (Q_{st}) and the positive mobility energy (E_m).

(2.13) $E_a = E_m - Q_{st}$ [29].

The permeance of microporous membranes is an exponential function of the temperature; while in mesoporous membranes it decreases with the square root of temperature. For this reason the study of the permeance of a gas as function of the temperature can be a way to asses either the presence or absence of defect-free microporous [30] and mesoporous layers [31].

2.5. References

[1] A.C. Pierre, "Introduction to Sol-gel Processing", Kluwer Academic Publisher, Dordrecht, 1998.

[2] R. Baker, R.W. Bott, C. Eaborn, P.W. Jones, J. Organomet. Chem. 1 (1963) 37.

[3] R.P.J. Corriu, M. Henner, J. Organomet. Chem. 74 (1974) 1.

[4] P.Y. Bruice, Organic Chemistry (2nd Edition), Prentice-Hall, New Jersey, 1998, p. 362.

[5] R.T. Morrison, R.N. Boyd, Organic Chemistry, (6th edition), Benjamin Cummings, San Francisco, 1992.

[6] H. Schmidt, H. Sholze, A. Kaiser, J, Non-Crystalline Solids, 63 (1984) 1.

[7] C.J. Brinker, G.W. Scherer, Sol-Gel Science, Academic Press, San Diego, 1990, p. 119

[8] R.K. Iler, "The chemistry of silica", Jhon Wiley and Sons, New York, 1979.

[9] R. Aelion, A. Loebel, F. Eirich, J. Amer. Chem. Soc. 72 (1950) 5705.

[10] P.W. Atkins, "General chemistry", Scientific American books, New York, 1989.

[11] J. Sekulić, J.E. ten Elshof, and D.H.A. Blank, 16 (2004).1546.

[12] T. Tsuru, T. Tsuge, S. Kubota, K. Yoshida, T. Yoshioka, M. Asaeda, Sep. Purif. Technol. 36 (2001) 3721.

[13] J. Etienne, A. Larbot, A. Julbe, C. Guizard L. Cot, J. Membrane Sci., 86 (1994) 95.

[14] A. Nijmeijer, H. Kruidhof, R. Bredesen, H. Verweij, J. Am. Ceram Soc. 84 (2001) 136.

[15] P.M. Biesheuvel and H. Verweij, J. Membr. Sci., 156 (1996) 250.

[16] H.P. Hsieh, "Inorganic membranes for separation and reaction", Membrane science and technology series, 3, (1996) 3.

[17] F. Rodriguez-Reinoso, M. Molina-Sabio, M.A. Muiiecas, J. Phys. Chem. 96 (1992) 2707.

[18] D.A. Mooney, J.M. Don MacElroy, Chem. Engin. Sci. 59 (2004) 2159.

[19] D. Briggs, Surface Analysis of Polymers by XPS and Static SIMS, Cambridge University Press, Cambrige, 1998, p. 7.

[20] P.J. Carreau, D.C.R. De Kee, R.P. Chhabra, "Rheology of Polymeric Systems: Principles and Applications", Hanser/Gardner Publications, Cincinnati, 2004.

[21] A.G. Fredrickson, Principles and Applications of Rheology, Prentice-Hall, Englewood Cliffs, N.J, 1964, p. 20.

[22] D.D. Do, Adsorption Analysis: Equilibria and Kinetics, vol 1, Imperial College Press, London, 1998, p.115.

[23] F.P. Cuperus, D. Bargeman, C.A. Smolders, J. Memb. Sci., 71(1992) 57.

[24] R.R. Bhave, "Inorganic Membranes: Synthesis, Characteristics and Applications", Van Nostrand Reinhold, New York, 1991, p. 338.

[25] P.W. Atkins, Physical Chemistry, (6^{th} edition), Oxford Press, Oxford, 1998, p. 28.

[26] M. Mulder, "Basic Principle of Membrane Technology", (2nd edition), Kluwer Academic Publisher, Dordrecht, 2000, p. 306.

[27] R.M. de Vos, "High-selectivity, high-flux silica membranes for gas separation", PhD Thesis, University of Twente, 1998, p. 113.

[28] R.B. Bird, W.E. Stewart, E.N. Lightfoot, Wiley, Transport Phenomena, (2nd edition), New York, 2002, p. 516.

[29] ref. 26, p. 42.

[30] V. Boffa, J.E. ten Elshof, A.V Petukhov, D.H.A. Blank, Adv. Funct. Mater. Submitted.

[31] V. Boffa, J.E. ten Elshof, D.H.A. Blank, Microprous Mesoporous Mater. 100 (2007) 173.

CHAPTER 3

A microporous niobia silica membrane for gas separation

Abstract

A novel microporous ceramic membrane for the recovery of CO_2 from gaseous streams was developed and characterized. Very high retention of CO_2 was achieved by introducing Nb^{5+} ions in a microporous silica framework by sol-gel synthesis. The membrane was made by coating an asymmetric γ-alumina disk with a 3:1 Si/Nb polymeric sol prepared from metal alkoxide precursors. Coated films were calcined at 500 °C. SEM and XPS analyses showed that the membrane consisted of a 150 nm thick layer with a Si/Nb atomic ratio of about 1.5. The single gas permeances of this membrane for small molecules decreased steadily with molecular size. The permeance of carbon dioxide deviated strongly from the generally observed trend. The interaction of CO_2 with the pores was studied by ATR-FTIR on a thin film, and is probably due to a relatively strong interaction between Nb-bound hydroxyl groups and CO_2. It was shown that hydrogen, helium and carbon dioxide followed an activated transport mechanism through the membrane. Deviation of linearity in the Arrhenius plots at low temperatures indicated the presence of large micropores or small mesopores in the thin layer.

3.1. Introduction

As stated in the previous chapter, both mesoporous and microporous ceramic membranes can be used for gas separation. Mesoporous membranes, with a pore diameter between 2 nm and 50 nm [1] are generally more permeable than microporous sieves, which have pores smaller than 2 nm by definition [1]. But mesoporous membranes have a relatively poor selectivity towards gases, since the transport across them is governed by the Knudsen law (this thesis, page 31), here written as:

$$(3.1)\ F = K \cdot \sqrt{\frac{1}{MRT}}$$

Where F is the membrane permeance, K is a constant depending only on the membrane properties, M is the molecular mass of the permeant, R is the gas constant and T is the absolute temperature.

The Knudsen law is generally applicable under all conditions in which the free path length of gas molecules is larger than the nearest pore wall, and is valid for the majority of incondensable gases. However, the permeation behaviour of carbon dioxide deviates from the behavior predicted by Equation 3.1 [2]. This has been explained in terms of the contribution of adsorption and surface diffusion of CO_2 to the total flux. In γ-alumina membranes with pore radii of 2.5-4 nm, the CO_2 permeance was found to be higher than that of lighter molecules like nitrogen [3,4]. The contribution of surface diffusion to the total transport rate of CO_2 was estimated to be about 30% at 20 °C [3], and became negligible above 300 °C [2].

Thus, it is possible to vary the CO_2 permeance by modification of the pore surface. Uhlhorn et al. [4] compared the CO_2 permeance of a mesoporous γ-alumina membrane and a magnesium oxide impregnated γ-alumina membrane and found that the CO_2/N_2 separation factor of the Mg-impregnated membrane was lower than that of the unmodified membrane. The authors proposed that the introduction of magnesia in the γ-alumina mesopores led to the formation of basic centers, in which CO_2 was strongly adsorbed. The mobility of CO_2 on the pore surface was therefore strongly restricted, resulting

in a low CO_2 permeance. McCool and De Sisto enhanced the CO_2 permeance of mesoporous silica membranes by covering the pore surface with covalently bonded amino groups [5]. They used a post-modification method in which amino-functional silanes were coupled to the hydroxyl groups of the preformed pore surface. The CO_2 permeance of the resulting membrane was higher because of the presence of these amino groups. In this case, the presence of sorption centers enhances CO_2 transport by increasing the concentration of CO_2 on the pore walls. However, if this interaction would be too strong, surface diffusion would be controlled by the low mobility of CO_2.

The selectivity of mesoporous membranes for separation of CO_2 is intrinsically limited by the fact that selective surface diffusion always occurs in parallel to the much less selective Knudsen diffusion separation through the gas phase, while selectivities higher than the theoretical Knudsen value can only be obtained at moderate temperatures when the population of adsorbed molecules is comparable to the number of molecules in the gas phase of the pore [2] Very high selectivities are only possible in the microporous regime, where gas-phase transport is impossible because the pores are so small that their width is comparable to the molecular size of the permeating species. Microporous silica membranes act as extremely effective molecular sieves by retaining the largest molecules of mixtures [6]. However, in the case of CO_2, with a kinetic diameter of 0.33 nm [7], separation from other small gases, like H_2 (0.28 nm), CH_4 (0.38 nm), CO (0.38 nm), N_2 (0.36 nm) and O_2 (0.35 nm), is only possible when differences in chemical properties between these gases are exploited for the separation [7].

This Chapter describes the preparation and the characterization of a microporous membrane with a large retention towards CO_2. Gas separation is based on a combination of size-based sieving and differences in molecule-wall interactions. The strategy behind this work was to introduce active surface sites to which carbon dioxide binds [4]. This was accomplished by introducing pentavalent niobium ions in a microporous silicon oxide matrix. The membrane was made by sol-gel synthesis from a silicon and niobium alkoxide-containing sol.

3.2. Experimental part

Synthesis of the NS membrane

11 ml of tetraethyl orthosilicate (Aldrich, 99.999% pure) was added to 10.5 ml of ethanol. An aqueous solution of nitric acid was dropped in the mixture until the final molar ratio (Si)-O-C_2H_5 : H_2O : HNO_3 was 1 : 0.5 : 0.01. We have chosen to express the chemical composition of the sol in this way because alkoxy groups, water and acid are the moieties that participate directly in the reaction. This mixture was heated under reflux at 60 °C for 2 h. Then a 1 M solution of niobium(V) penta(n-butoxide) (Gelest) in n-butanol (Aldrich, anhydrous) was added slowly to the mixture. Aqueous nitric acid was dropped into the mixture to restore the initial composition (M)-O-R : H_2O : HNO_3 to 1 : 0.5 : 0.01, with M = Si, Nb and R = C_2H_5 or C_4H_9. The sol was refluxed at 60 °C for 5 h. Then it was cooled down to -20 °C and kept at this temperature for few days until it was used for characterization or membrane preparation.

Membrane preparation

The NS membrane was prepared by dipping a porous support into the 4% diluted NS sol. The porous support consisted of a 2 mm thick α-alumina disk, coated on one side with a 6% La-doped γ-alumina film of about 2 μm thickness. The NS coating was deposited on the γ-alumina layer, which had an average pore diameter of about 4 nm.

This was done in a class 1000 clean room using an automatic dip-coating machine, with an angular dipping rate of 0.06 rad·s^{-1}. The membrane was calcined in air at 500 °C, using heating and cooling rates of 0.5 °C/min.

Characterization of membrane morphology

Thickness and morphology of the NS membranes were analyzed by Scanning Electron Microscopy (SEM) on a LEO 1550 FEG.

X-ray Photoelectron Spectroscopy (XPS) measurements were performed on a PHI Quantera Scanning ESCA Microprobe equipped with a monochromatic

AlKα X-ray source (1486.6 eV) at a pressure < $8 \cdot 10^{-6}$ bar. Film thickness was determined by monitoring the atomic composition of the film at different depths after sputtering the material with Ar^+ ions. The sputter rate was calibrated on a 100 nm SiO_2 film on silicon.
The chemical composition of a powdered sample of the NS sol was measured by X-ray Fluorescence (XRF) using a Philips PW1480 apparatus.

Permeation experiments

Single-gas permeation measurements were done in a dead-end mode set-up. Permeabilities of gases with different kinetic diameter were measured at 5 bar at the feed side and atmospheric pressure at the retentate side. The gas flow was measured with a soap film flow meter. Since atmospheric water can condense in the pores of the silica matrix, all membranes were dried at 200 °C in a hydrogen flow for at least 16 h before any measurements were done. The permeation rates of different gases were determined in a sequence starting with the one with the smallest kinetic diameter, and equilibrating for a few hours each time a new gas was introduced into the set-up. The Arrhenius plots were obtained by varying the membrane temperature from 200 °C to 50 °C. The resistance of the support for H_2, He, CO_2 and CH_4 was measured at 200, 160, 110 and 50 °C. The resistance at other temperatures was obtained by fitting these data to Equation 3.1.

ATR measurements

A thin film of niobium-doped silica was prepared by spin-coating the NS sol on a ZnSe crystal. The ZnSe crystal was completely covered by the NS sol and spinned for 20 s at a speed of 2000 rpm. This procedure was repeated 5 times and then the thin film was dried at 250 °C for 3 h (heating/cooling rates of 0.5 °C min^{-1}). As a reference, a thin film of silica was prepared following the same protocol, using a standard polymeric silica sol [8]. The ATR measurements were performed at room temperature on a Bruker Tensor 27 equipped with a MCT detector. The samples were first exposed to nitrogen for

about 1 hour and then to a continuous flow of CO_2 (10 ml/min) at 1 bar of pressure.

3.3. Results and discussion

The sol was prepared from tetraethylortosilicate (TEOS) and niobium(V) penta(n-butoxide) in an acidic alcoholic solution. Since metal alkoxides derived from silicon are less reactive than those derived from niobium, TEOS was pre-hydrolyzed before reacting with Nb(V) penta(n-butoxide), as described in more detail in the experimental section. The prepared sol will further be referred to as NS sol, and the corresponding membrane will be referred to as NS membrane.

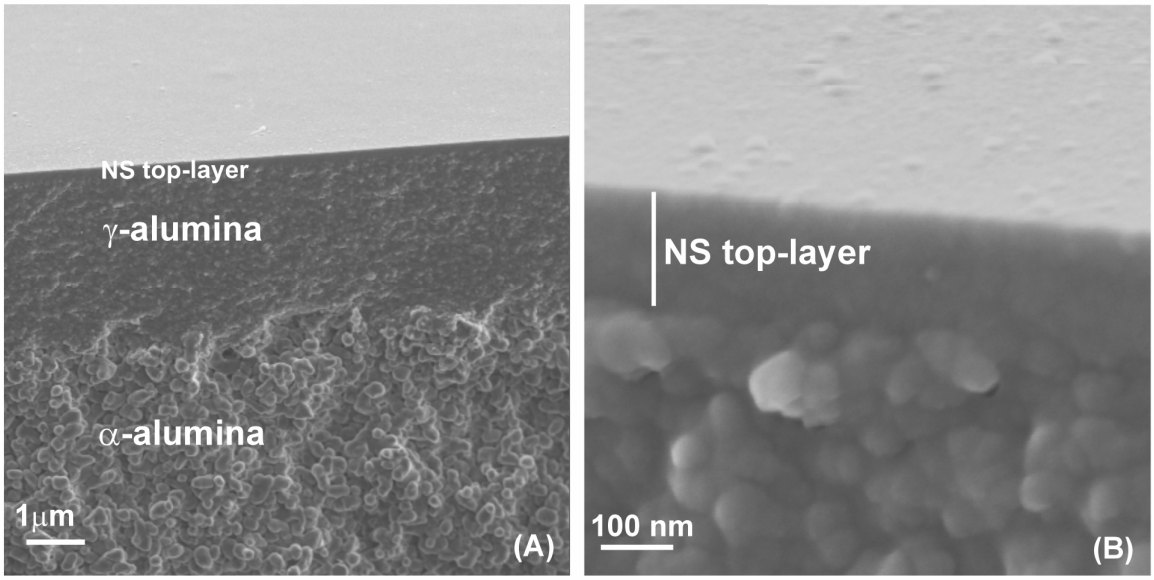

Figure 3.1. SEM images of the NS membrane cross-section. (a) Asymmetric three layer structure. (b) Magnification of the 150 nm thick gas selective NS top-layer.

A membrane was prepared by direct coating of the NS sol onto a mesoporous asymmetric support following a above described procedure. A SEM picture of the cross-section of the membrane after calcination at 500 °C is shown in Figure 3.1. The asymmetric architecture of the membrane is clearly visible in Figure 3.1a. From bottom to top the α-alumina macroporous support,

γ-alumina intermediate layer, and NS gas-selective top layer can be seen. The thickness of the NS top layer was 150 nm, as shown in Figure 3.1b.

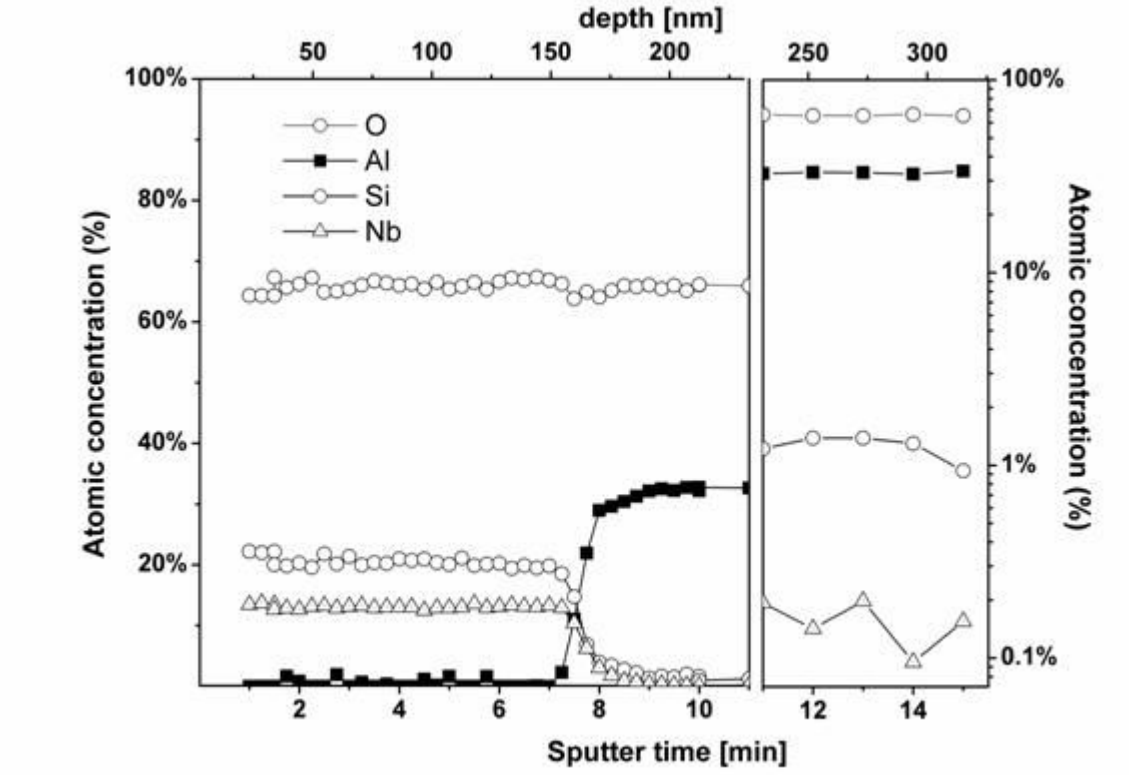

Figure 3.2. XPS depth profile of the NS membrane. Ar^+ sputtering rate is 21 nm/min.

The compositions of the NS sols and the supported thin films were determined by X-ray fluorescence (XFR) and X-ray photoelectron spectroscopy (XPS), respectively. The atomic Si/Nb ratio of a dried NS sol was found to be equal to 2.9, not far from the atomic ratio of 3.0 in which the two metal precursors had been added. No other metals were detected by XRF. Figure 3.2 shows the atomic concentrations of Si, Nb, Al and O as determined by XPS as a function of depth below the membrane surface. A 25-30 nm thick transition region between top and intermediate layer can be observed at a depth of 150 nm. The Si/Nb ratio in the top layer deviated strongly from the composition of the coating sol. The Si/Nb molar ratio in the top layer was about 1.5. Thus, the microporous top layer was richer in niobium than the starting sol. This can possibly be attributed to the higher reactivity of niobium alkoxides compared

to TEOS, which makes them form large polymeric structures faster. At an estimated depth of about 250-300 nm the silicon atomic concentration was still about 1 at%, while niobium traces up to about 0.1 at% were also detected. This seems to indicate that part of the TEOS in the sol did not react or reacted only to form small clusters. These clusters may have been drained into the support together with the solvent as the coating was applied. The extent to which the niobium precursor had already undergone hydrolysis and condensation was probably higher than for TEOS, making it form sol particles that were large enough not to be drained into the support.

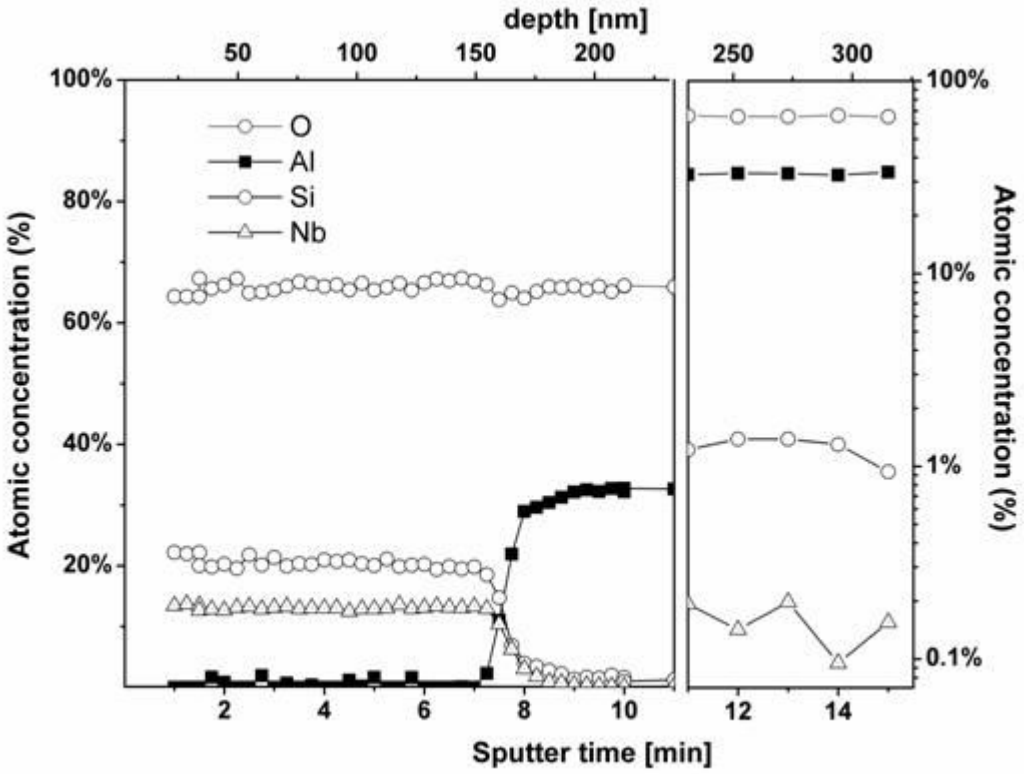

Figure 3.3. Single gas permeation experiments. (a) Knudsen plot of support and NS membrane. The Knudsen behavior of the support is indicated by the drawn line, which was obtained by fitting experimental values to Equation 1. The prediction of Knudsen diffusion of the NS membrane is indicated by the dashed line, which was obtained by fitting to the experimental SF_6 permeance. (b) Permeance as function of kinetic diameter; the dashed line serves as a guide to the eye to indicate the approximate effect of size sieving of the membrane.

The sieving capacity of the membrane was assessed by measuring the

permeance of a series of probe molecules with different masses and kinetic diameters. The measurements were performed at 200 °C and a pressure difference of 4 bar across the membrane. The results are shown in Figure 3.3a and 4b. The permeance of the membrane for different gases before and after deposition of the NS layer are compared in Figure 3.3a.

The Knudsen behavior of the mesoporous support is shown by the drawn line in Figure 3.3a. It was obtained by fitting Equation 3.1 to the experimental data of the permeance of the probes. The curve indicates a regime that is fully governed by transport through mesopores. After coating of the NS layer on the support, the permeance was no longer related to the molecular mass of the permeant molecules. This is illustrated in Figure 3.3a by the dashed line that was calculated from the experimental SF_6 permeance using Equation 3.1. It can be seen that hydrogen and helium have a comparatively higher permeance than the larger molecules, while the permeance of CO_2 is about six times smaller. A good correlation was found between permeance and kinetic diameter, as shown by the dashed line in Figure 3.3b. Except for CO_2, all probe molecules interact weakly with the surface of the pores of the mixed metal oxide film. Information on the permeance of such weakly interacting species can be thus used to estimate the pore size distribution in the NS layer by comparing the permeance with the kinetic diameter of the permeating molecule. The data shown in Figure 3.3b suggest that a large part of the membrane pores have a diameter that is smaller than nitrogen (kinetic diameter 0.36 nm), since the membrane permeance decreased by 92% when the probe was changed from helium to nitrogen. The permeance of the membrane to the largest gas molecule SF_6 (kinetic diameter 0.55 nm) was not negligible. This reveals the presence of pores or defects larger than 0.55 nm.

The permeance of CO_2 was exceptionally low considering its moderate molecular size. A roughly 6 times higher permeance would be expected based on the behavior of the other probes. At 200 °C the ideal separation factor for CO_2/SF_6 mixture was 0.29 and not 1.8 as predicted by the Knudsen mechanism. This is an indication that the transport of SF_6 occurs in large

micropores, rather than in mesopores or in defects, because in such a pore structure the permeance of CO_2 should be equal to or larger than the permeance of SF_6.

To understand the transport mechanism that governs the permeance in more detail, we studied the temperature dependency of the permeance of various gases.

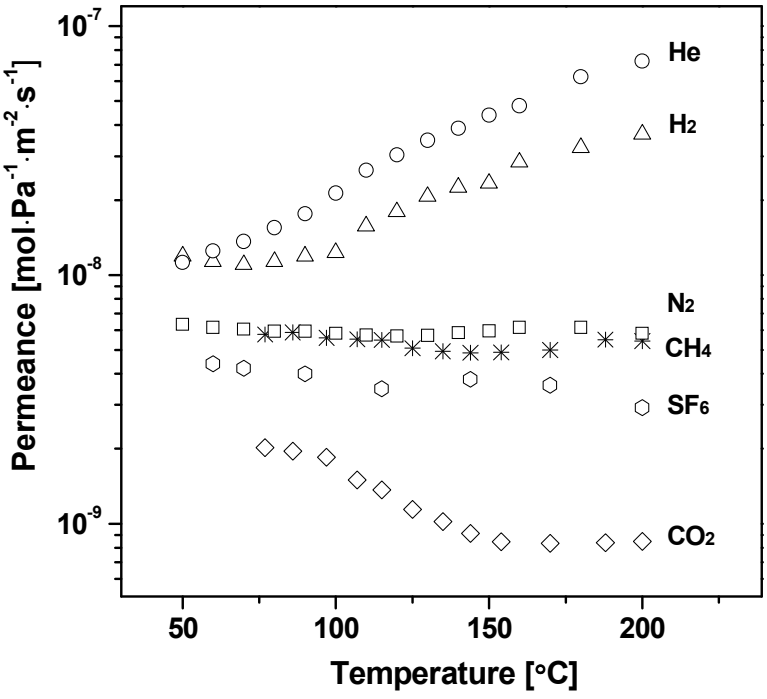

Figure 3.4. Temperature dependency of the He, H_2, CO_2, N_2, CH_4 and SF_6 permeances of the NS membrane.

Figure 3.4 shows the permeance of the NS membrane for different probes. The flux of helium and hydrogen across the membrane increased exponentially with increasing temperature; while a decrease of CO_2 flux was observed. The temperature dependency of N_2, CH_4 and SF_6 was more complex, as shown in Figure 3.4.

Since the membrane is a stack of layers, the total resistance of the membrane is the sum of the resistances of each layer. By definition the resistance of a membrane to a flux is proportional to the inverse of the permeance. The

permeance of the NS-layer can thus be determined from the total permeance and the permeance of the support via[8]

$$3.2)\ \frac{1}{F_{tot}} = \frac{1}{F_{NS}} + \frac{1}{F_{Sup}},$$

where $1/F_{tot}$ is the total resistance and $1/F_{NS}$ and $1/F_{Sup}$ are the resistances of the top layer and support, respectively. The helium permeance in the support was found to be $7.5 \cdot 10^{-7}$ mol·Pa^{-1}·m^{-2}·s^{-1} at 200 °C. This means that the contribution of the support to the total resistance of the membrane was about 9.6 % at this temperature. For all other gases the contribution of the support to the total resistance is smaller than this value. Hence, the overall resistance of the membrane was mainly localized in the top layer.

The permeance of the support to 6 probe molecules at different temperatures is depicted in Figure 3.5. This graph shows that gas transport in the support occurs according to a Knudsen-type mechanism for all reported molecules. So the constant K in Equation 3.1 was determined to have a numeric value of $8.9 \cdot 10^{-5} \pm 1 \cdot 10^{-6}$ by linear fitting of the data points in Figure 3.5. However, contrary to what was predicted by Equation 3.1, the extrapolated fit line does

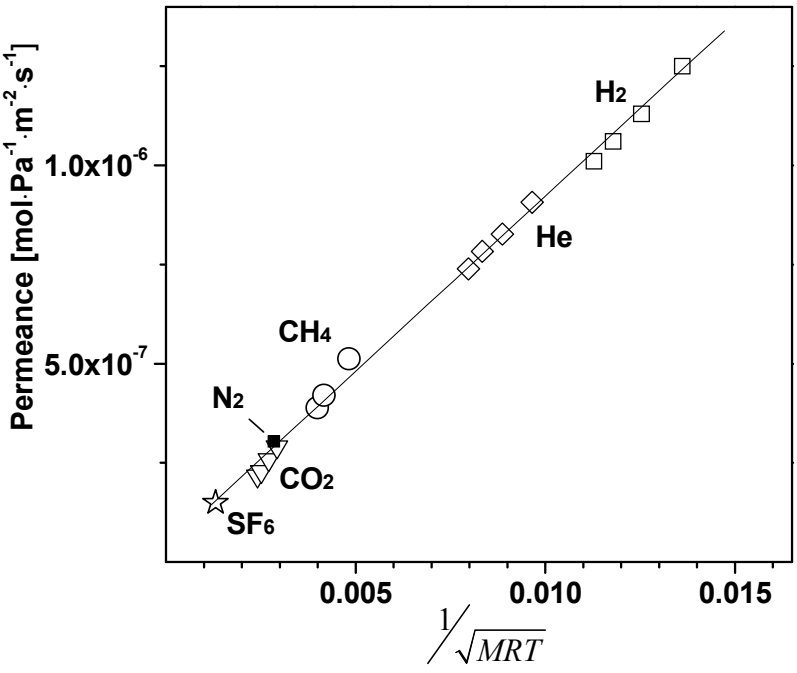

Figure 3.5. Permeances of 6 probe molecules trough a γ-alumina disk of the type used as a support for the microporous membranes presented here. The straight line represents the best fit of the data to Equation 3.1.

not cross the origin, but intersects the y-axis at a permeance of $3.3 \cdot 10^{-8}$ $mol \cdot Pa^{-1} \cdot m^{-2} \cdot s^{-1}$. This is due to a small contribution of viscous flow to the total permeance. The latter contribution is almost irrelevant to the total transport and Equation 3.1 can fit the data in Figure 3.5 with a standard deviation of $2.1 \cdot 10^{-8}$ $mol \cdot Pa^{-1} \cdot m^{-2} \cdot s^{-1}$.

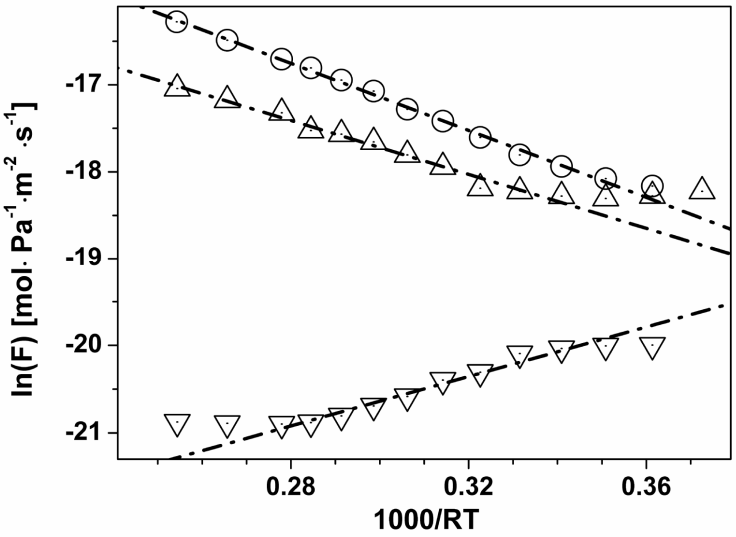

Figure 3.6. Arrhenius plots of the permeance F of He, H_2 and CO_2 in the NS top layer.

The permeances of He, H_2 and CO_2 in the NS top layer versus temperature are shown in Figure 3.6, as calculated by using Equation 3.2 and the straight line in Figure 3.5. Gas transport in micropores occurs essentially according to a surface diffusion mechanism. The transport rate associated with this mechanism can be expressed in terms of a modified Fick law [8]:

$$(3.3)\quad J = J_0 \exp\left\{-\frac{E_a}{RT}\right\}\frac{\Delta P}{L}.$$

J_0 is a temperature independent coefficient and E_a is the apparent activation energy. E_a is the sum of two contributions: the heat of sorption of the molecule (here considered as a negative number, since adsorption is an exothermic process in which heat is released) and the positive activation energy of mobility. Since these two terms have opposite signs the apparent activation energy can be positive or negative depending on their relative magnitudes. A negative value of E_a is generally interpreted as being caused by strong adsorption of the molecule on the pore surface. Table 3.1 lists the activation energies calculated from Figure 3.6, together with some data on pure and metal oxide doped silica membranes that have been reported elsewhere [8-13].

Above a certain temperature, here named $T_{Kn,}$ the permeances of He and H_2 show an Arrhenius-type temperature dependency in agreement with Equation 3.3. This suggests that hydrogen and helium transport across the membrane occurs essentially via surface diffusion through micropores. Apparent activation energies of 19.1±0.3 kJ·mol^{-1} and 15.3±0.7 kJ·mol^{-1} were calculated for helium and hydrogen, respectively. The values measured in this work are close to those reported by Nair et al., who found activation energies of helium permeance of 23 kJ·mol^{-1} in pure silica [9]. Asaeda reported an increase in apparent activation energy of H_2 permeance from 3.4 to 44 kJ·mol^{-1} when the Zr dopant loading in silica was increased from 10 to 90 mol % [13].

Table 3.1. Apparent activation energies E_a of molecular transport of He, H_2 and CO_2 in NS top layer, calculated by fitting the data reported in Figure 3.6, and their comparison with literature values for pure and doped silica membranes prepared by sol-gel coating. When more values were presented in a study the lowest one is reported on the left side of the semicolon and the highest one on the right side.

	Ea [KJ·mol^{-1}]			Calcination T [°C]	Ref.
	He	H_2	CO_2		
NS	19.1±0.3	15.3±0.7	-14.2±0.8	500	
SiO_2		7.6 ; 8	-4 ; -2	400 ; 600	[8]
SiO_2	7 ; 23			400	[9]
SiO_2		12.3; 21.7	3 ; 6.8	400	[10]
SiO_2	4 ; 9	10 ; 11	0 ; 10	400	11]
33%Ni-doped SiO_2	7.1			500	[12]
10%Zr-doped SiO_2	4.7	3.4		570	[13]
50%Zr-doped SiO_2	22	44			

The deviation from Equation 3.3 below the threshold temperature T_{Kn}, which is 90 °C for hydrogen and 70 °C for helium, can be explained by assuming two parallel transport paths in the microporous top layer. We can consider a

mesoporous path with an associated permeance F_{Kn} where a Knudsen-type diffusion mechanism is operating, and a microporous path with an associated permeance F_{mic}, where a surface diffusion mechanism dominates. The overall permeance of the top layer F_{NS} is the sum of these two contributions $F_{mic}+F_{Kn}$. While Knudsen diffusion becomes negligible at high temperatures due to its $T^{-0.5}$ temperature dependency, it can be dominant at low temperatures where it may contribute significantly to the overall transport rate. The sum of these two parallel contributions yields a curve with profiles as shown in Figure 3.6 for He and H_2. Since hydrogen has a larger kinetic diameter than helium and is lighter, the contribution of Knudsen transport to the total flux across the membrane is higher for hydrogen than for helium. This expectation agrees with the experimental observation that the hydrogen permeance deviates from the behavior predicted by Equation 3.3 at a higher temperature than helium.

As shown in Figure 3.4, the temperature dependencies of the permeances of N_2, CH_4 and SF_6 molecules are less pronounced and more scattered. After correction for the support resistance, the following E_a were measured: -0.3 ± 0.3 kJ·mol^{-1} for N_2, -1.3 ± 0.6 kJ·mol^{-1} for CH_4 and -3.0 ± 0.7 kJ·mol^{-1} for SF_6. These slight negative activation energies are probably not related to a real activated transport, but most likely depend on the fact that between 90 °C and 200 °C the dominant transport mechanism of N_2, CH_4 and SF_6 is via the gas phase. If a temperature T_{Kn} would also exist for these molecules, it would probably be close to or higher than 200 °C.

The apparent activation energy of CO_2 was calculated by a linear fit of all data points below 150°C. This yielded a value of -14.2 ± 0.8 kJ·mol^{-1}. Such a highly negative value suggests a high enthalpy of sorption. The data in Figure 3.6 show either positive activation energies for CO_2 permeance [10,11], or slightly negative values [8]. But none of these values is close to -14.2 ± 0.6 kJ·mol^{-1} as measured on the NS membrane. The large exothermic enthalpy of sorption of CO_2 on the NS pore walls may also explain why CO_2 has a lower permeance than N_2, CH_4 and SF_6, without significant contribution of gas-phase transport. Indeed a high coverage of the pore walls by CO_2 molecules may result in

narrowing of the actual pore diameter and thus in a significant reduction of the number of channels that are large enough to allow transport in the gas phase.

We investigated the absorption of CO_2 onto the surface of NS pores by infrared spectroscopy. We first studied CO_2 adsorption on a powder that was obtained by calcining dried NS sol using the same heating program as for the NS membrane. However, after calcination, we obtained a black powder with extremely low surface area (as revealed by nitrogen sorption analysis) and good quality IR sorption measurements were not possible.

Adsorption of CO_2 was therefore measured by Attenuated Total Reflectance Fourier Transform Infrared Spectroscopy (ATR/FTIR) on a 94 nm thick NS film spin-coated on a ZnSe crystal and calcined at 250 °C. A 126 nm thick film of pure silica was used as reference. The thickness of these films was determined by X-ray fluorescence (XPS) analysis. Figure 3.7 shows the IR spectra of the two samples. The vibrations of the SiO_4^{4-} tetrahedron [14] are visible at 804 and 1050 cm^{-1} in the case of the NS membrane, and at 806 and 1070 cm^{-1} in the case of pure silica. The high intensity peak in the NS sample at a wave number of ~960 cm^{-1} has been attributed to the presence of niobium atoms in the oxide network [14]. At 1445 cm^{-1} a sorption band is visible in the spectrum of niobium-doped silica. This band is commonly assigned to carbonate-like species on the

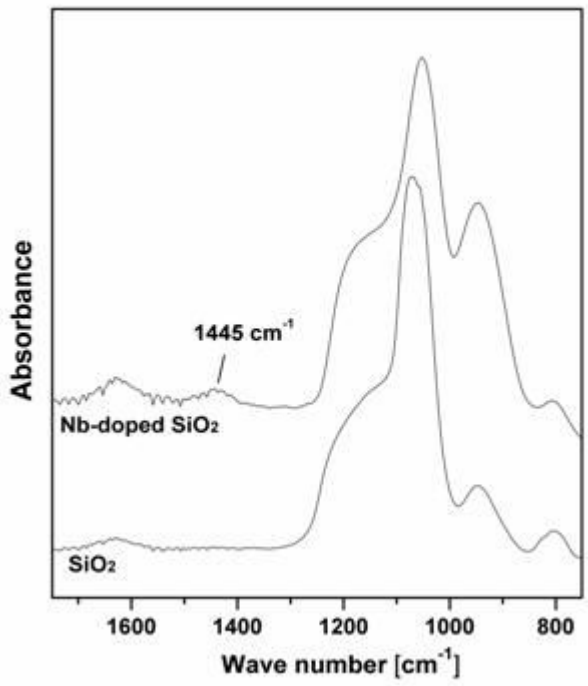

Figure 3.7. Room temperature ATR/FTIR spectra of pure silica and NS films in nitrogen atmosphere.

metal oxide surface [15,16]. As expected, this peak was absent in the spectrum of silica. Since the band at 1445 cm^{-1} is broad it is not possible to determine a specific type of carbonate present on the NS surface. However, surface carbonates are strongly bound species and presumably do not play a determining role in the transport rate of CO_2 at 200 °C [17-18]. Therefore, in a second series of experiments the measuring cell was flushed with CO_2 at a rate of 10 ml/min and the infrared absorption spectrum was recorded as function of time. It was observed that only the part of the spectrum between 2280 and 2400 cm^{-1} changed. This was due to changes in stretching mode vibrations of both CO_2 in the gas phase of the cell, and CO_2 adsorbed on the oxide surface. Figure 3.8shows the temporal evolution of this band. A comparison is made with the spectrum of pure CO_2 gas as measured on a bare ZnSe crystal. The intensity of the band increased in the course of the sorption process. Even after 50 minutes a steady value had not been reached. This can probably be explained by considering that the pores of the material are so narrow that the crossover of CO_2 molecules diffusing into, and N_2 molecules diffusing out of the micropores is rate determining. The band at 2345 cm^{-1} is not present in the spectrum of gaseous CO_2 and is comparable to a value reported for CO_2 adsorbed in silicalite [17-20]. This band had been ascribed to the ν_3 stretching vibration of CO_2 sorbed on surface cations [16-19]. A

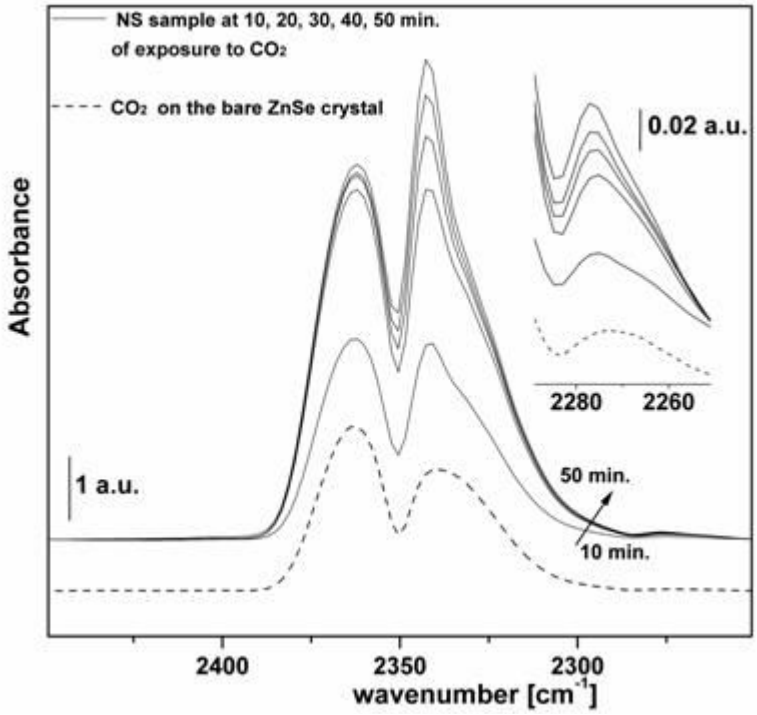

Figure 3.8. Asymmetric stretch (ν_3) region of the room temperature ATR/FTIR spectra of CO_2 adsorbed on NS and measuerd on a bare ZnSe crystal. Inset shows a magnified view of the $^{13}CO_2$ ν_3 asymmetric stretch region.

further indication for this interaction is provided by the band related to the $^{13}CO_2$ ν_3 stretching mode shown in the inset of Figure 8. This band has an intensity that is about 100 times lower than that of the corresponding $^{12}CO_2$ signal depicted in the main body of the figure. The position of the $^{13}CO_2$ ν_3 stretching band is 2277 cm^{-1} for NS and 2271 cm^{-1} for pure CO_2. The spectrum of CO_2 sorbed on the silica film showed a qualitatively similar evolution as on NS and is not shown here. This suggests that CO_2 interacts with hydroxyl groups on the pore wall in both silica and niobia-doped silica, and not with niobium cations exposed on the surface. The fact that the main band of the CO_2 stretching band is at 2345 cm^{-1} in both silica and NS is not in conflict with the data reported in Table 1. Indeed, Pires [19] observed similar CO_2 ν_3 stretching frequencies in zeolites which had heats of sorption for CO_2 that differed by more than 10 $kJ \cdot mol^{-1}$. We therefore propose that the low permeance of CO_2 in NS is primarily due to strong adsorption of CO_2 on surface hydroxyl groups, presumably those which are directly bound to Nb. The more polar character of the NbOH bonds in NS will have a stronger interaction with CO_2 than surface OH groups that are connected to Si.

In Figure 3.9 the H_2/CO_2 and CH_4/CO_2 ideal permselectivities of the NS membrane at different temperatures are compared with that of the support. The ideal permselectivity of the support for both mixtures was approximately temperature independent and close to the theoretical limits predicted by the Knudsen law. On the other hand, the permselectivity of the NS membrane towards H_2/CO_2 increased rapidly as a function of temperature. This is probably due to the high activation energy of mobility of hydrogen, and the large heat of sorption of carbon dioxide. The ideal H_2/CO_2 selectivity was 5.8 at 60 °C, and increased to 43.2 at 200 °C. A similar but less prominent trend was observed for CH_4/CO_2. The ideal selectivity increased from 3.3 at 80 °C to 7.0 at 200 °C. These measurements indicate that NS may be a suitable membrane material for CO_2 sequestration from streams containing hydrogen and/or methane.

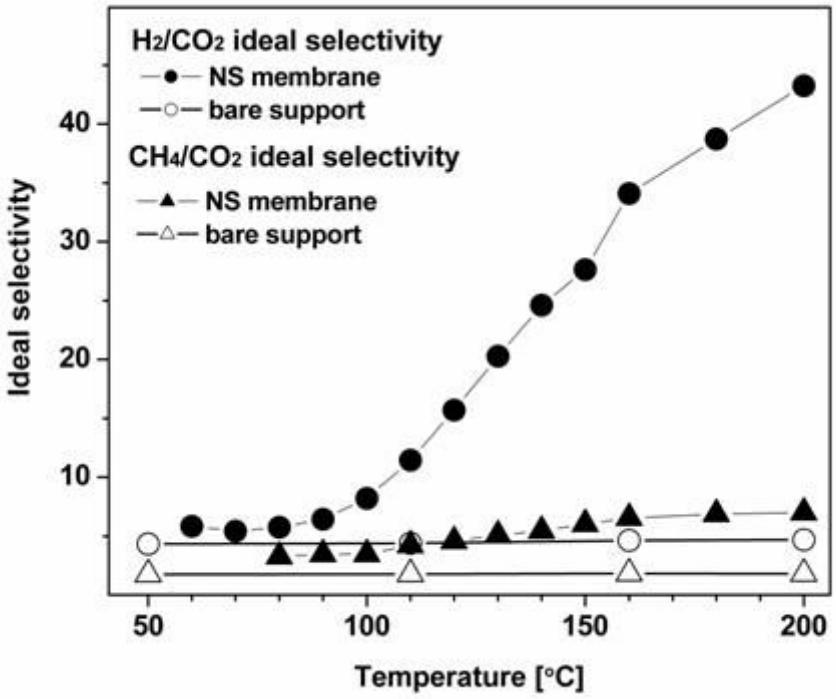

Figure 3.9. H_2/CO_2 and CH_4/CO_2 ideal permselectivities as calculated from single gas permeation experiments in the temperature range between 50 and 200 °C.

3.4. Conclusions

The microporous NS layer is a new type of selective membrane for CO_2 separation from gas mixtures. The results shown here are promising. Since the membrane was not completely impermeable to SF_6, it should be possible to optimize the membrane microstructure further by eliminating pores larger than ~0.55 nm in order to achieve even higher separation factors. The exceptionally low permeance of CO_2 was explained as a consequence of strong chemical interaction between CO_2 and the pore surface of the microporous material, presumably Nb-bound hydroxyl groups.

The presence of acidic and basic sites on niobium-doped silica has been reported before [20,21]. Acidic centers have been observed by Raman spectroscopy after pretreatment in dry oxygen at 500 °C, as well as ionic couples $Nb\text{-}O^-$ and Nb^+ when activated at temperatures above 400-500 °C 20].

This material has therefore been suggested as potential catalyst for redox reactions 20,21] and it seems intriguing to try to exploit the catalytic activity of Nb-doped silica membranes in a catalytic membrane reactor.

The results shown for the NS membrane are an indication that other silica doped membranes may also be used for molecular separations based on sorption rather than on molecular size differences between molecules. Hence, we suggest to introduce aliovalent ions other than Nb into the silica matrix to promote specific molecular separations.

3.5. References

[1] K.S.W. Sing, D.H. Everett, R.A. W. Haul, L. Moscou, R.A. Pierotti, J. Rouquerol, T. Siemieniewska, Pure Appl. Chem. 57 (1985) 603.

[2] R.R. Bhave, "Inorganic Membranes: Synthesis, Characteristics and Applications", Van Nostrand Reinhold, New York, 1991, p. 338.

[3] R. J. R. Uhlhorn, K. Keizer and, R.J. Van Vuren, A. J. Burggraaf, J. Membrane Sci. 39 (1989) 285.

[4] R. J. R. Uhlhorn, K. Keizer and, A. J. Burggraaf, J. Membrane Sci. (1989) 46, 225.

[5] B.A. McCool, W.J. DeSisto, Adv. Funct. Mater. 15 (2005) 1635.

[6] R.M. de Vos, H. Verweij, Science 279 (1998) 1710.

[7] D.W. Breck, Zeolite Molecular Sieves-Structure, Chemistry, and Use, John Wiley & Sons, New York, 1974, p. 636.

[8] R.M. de Vos, H. Verweij, J. Membrane Sci. 143 (1998) 37.

[9] B.N. Nair, K. Keizer, H. Suematsu, Y. Suma, N. Kaneko, S. Ono, T. Okubo, S.-I. Nakao, Langmuir 16 (2000) 4558.

[10] R.S.A. de Lange, K. Keizer, A.J. Burggraaf, J. Membrane Sci. 104 (1995) 81.

[11] R.J.R. Uhlhom, K. Keizer, A.J. Burggraaf, J. Membrane Sci. 66 (1992) 271.

[12] M. Kanezashi, T. Fujita, M. Asaeda, Separation Sci. Techn. 40 (2005) 225.

[13] K. Yoshida, Y. Hirano, H. Fujii, T. Tsuru, M. Asaeda, J, Chem. Eng. Jap., 34 (2001) 523.

[14] Y. Liu, K. Murata, M. Inaba, Chem. Lett. 32 (2003) 992.

[15] A.A. Davydov, "Infrared Spectroscopy of Adsorbed Species on the Surface of Transition Metal Oxides", John Wiley & Sons, West Sussex ,1984.

[16] M. Cerruti, C. Morterra, Langmuir 20 (2004) 6382.

[17] B. Bonelli, B. Onida, B. Fubini, C. Otero Areán, E. Garrone, J. Phys. Chem. B 104 (2000) 10978.

[18] B. Bonelli, B. Onida, B. Fubini, C. Otero Areán, E. Garrone, Langmuir 16 (2000) 4976.

[19] J. Pires, M. Brotas de Carvalho, J. Molecular Cat. 83 (1993) 295.

[20] J.-M. Jehng, I.E. Wachs, Catalysis Today, 8 (1990) 37.

[21] M. Ziolek, I. Sobcsak, I. Novak, P. Decyk, A. Lewanowska, J. Kujawa, Microporous Mesoporous Mater. 35 (2000) 195.

CHAPTER 4

Niobia-silica sols: a SAXS study

Abstract:

About 40 niobia-silica (NSs) sols were analyzed by small angle X-ray scattering (SAXS) to gain a better understanding of the formation and aggregation mechanism of niobia-silica nanoparticles, and to asses which sols can be used successfully for membrane engineering. In all samples a niobium alkoxide was added to a pre-hydrolyzed silica sol. Independent of the synthetis procedure the fractal dimension (D_f) of the niobia-silica particles was always larger than 1.5. When tetraethyl orthosilicate (TEOS) was used as silica source, D_f increased as a function of time, to remain constant at an upper value equal to 1.9. The gyration radius (R_g) of all the sols grew proportionally to $t^{½}$. For this reason a diffusion limited growth mechanism is proposed. Dilution and moderate reaction temperatures can be employed to slow down the reaction rate in order to control the size of the particles precisely. The sols presented here had a Nb:Si molar ratio between 0.33 and 0.8. Generally, sols with higher Nb:Si molar ratios were more developed, due to the higher reactivity of the niobia precursors compared to TEOS. Higher growth rates were measured for sols with higher water contents. The concentration of acid can also increase the growth rate of polymeric particles, especially in the early stages of the synthesis when a reaction limited mechanism cannot be excluded. When 1,2-bis(triethoxysilyl)ethane (BTESE) was used as silica source, particles with $R_g > 6$ nm and $D_f > 2.3$ were obtained. To ensure homogeneous mixing of Si and Nb, it is necessary to maximize the concentration of silanol groups at the moment of incorporation of niobia. This can be accomplished by maximizing the degree of hydrolysis of silica precursors, and minimizing the degree of condensation. The data reported here suggest that the condensation of highly reactive Nb-OH groups with less reactive Si-OH groups may also help to control the condensation rate.

4.1. Introduction

In the preparation of microporous membranes the size of precursor sol particles must be controlled carefully in order to be able to deposit layers of sufficient quality and suitable thickness. A diameter of the sol nanoparticles of 4-5 nm is sufficient to prevent penetration of the sol into the 5-8 nm wide pores of the underlying γ-alumina support. To fabricate a microporous silica-based material via the sol-gel route, a polymeric sol needs to be employed. Polymeric sols differ from colloidal sols because their particles are not dense bodies but macromolecular chains formed by an alternation of metallic atoms and oxygen atoms. These macromolecules can be linear or branched. Most often they are fractalic in nature and their shape can be characterized in terms of a fractal dimension (D_f). The mass of such objects M scales with their size R as [1]:

(4.1) $M \propto R^{D_f}$.

The fractal dimension D_f is also a very important parameter and should be precisely controlled in order to obtain a material with micropores only. A microporous network can be formed when the sol particles are able to interpenetrate each other while their concentration increases during the drying process. Brinker suggested that microporous silica can be formed from sols with D_f smaller than or close to a threshold value of 1.5 [2].

The Nb/Si oxide sols (NS*s*) were characterized by small angle X-ray scattering (SAXS) using synchrotron radiation at the BM-26B station of the Dutch-Belgian beam line (DUBBLE) of the European Synchrotron Radiation Facility in Grenoble, France. SAXS allows estimation of the effective particle size in solution, expressed as the gyration radius R_g, and permits measurement of the fractal dimension D_f.

SAXS allows rapid assessment of the suitability of sols for membrane engineering. Thus, on the basis of this analysis appropriate sols for preparation of membranes can be selected. This chapter also aims to provide a better understanding of the formation and aggregation mechanism of niobia-silica nanoparticles.

Principles of SAXS measurements

In a SAXS measurement the scattered intensity is determined as function of the scattering vector q [nm^{-1}], which is related to the scattering angle θ as follows:

$$q = \frac{2\pi}{\lambda}\sin(2\theta). \quad (4.2)$$

Here θ is the scattering angle and λ is the wavelength of the beam.

Figure 1a shows the raw data as acquired by the gas-filled 2D-detector of DUBBLE. These data concern the NS sol and they are used here as illustration for the general explanation of theory. The position of the incident beam is indicated by an arrow. The beam was focused on a corner of the 2D detector, in such way that the detection window was opened in the largest range of q values possible. A beam stopper was required to shield the detector from the direct beam and thus to avoid saturation of the outgoing signal. The position of the beam stopper is marked in Figure 1a by the triangular shadow.

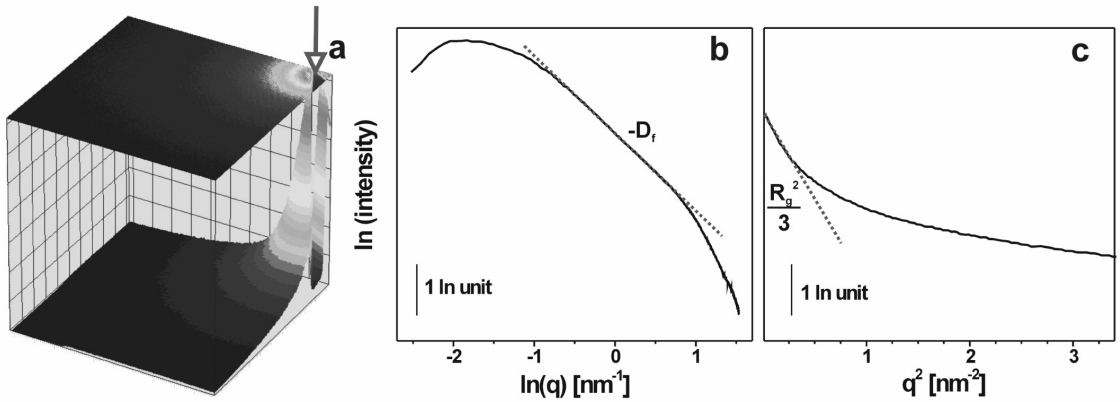

Figure 4.1. SAXS analysis of the NS sol. (a) Raw data acquired from the 2D gas-filled detector of DUBBLE. After background and mask subtraction the 1-dimensional data were plotted in a Porod plot (b) and in a Guinier plot (c). In both graphs the intensity $I(q)$ is expressed in arbitrary units.

After background subtraction, the scattered intensity $I(q)$ was plotted as a function of the scattering vector q in a Porod plot (Figure 1b) and in a Guinier plot (Figure 1c).

The Porod plot shown in Figure 4.1b represents a typical scattering curve of polymeric metal oxide based sols [3]. The part of the curve between the two limiting values $q = 1/r_0 = 2.09$ nm^{-1} and $q = 1/\xi = 0.55$ nm^{-1} is linear. This implies that the scattered intensity $I(q)$ in this interval is a power function of q [4]:

(4.3) $I(q) \propto q^{-D_f}$.

Here D_f corresponds to the fractal dimension of the nanoparticles of which the sol is composed. r_0 represent the size of the primary scatterers forming the fractals, while ξ is a parameter related to the gyration radius (R_g) of the whole fractal structure.

At small q the scattered intensity of a sol containing particles with a gyration radius (R_g) can be expressed by the Guinier law [4]:

(4.4) $$I(q) \propto \exp\left(-q^2 \frac{R_g^2}{3}\right).$$

As shown in Figure 1c, the logarithm of the scattering intensity had an approximately linear relationship with q^2 at small q. Fitting data in the range of q values where this relationship is valid allows calculation of the the gyration radius R_g by using Equation 4.4.

Principle of DLS

Dynamic light scattering (DLS) is a well established technique for measuring particle sizes in the 10^{-9}-10^{-6} m range. DLS measurements determine the velocity at which particles within a solvent diffuse due to Brownian motion. This is done by monitoring the fluctuations of intensity of the scattered light beam over time. The scattered intensity varies constantly depending on particle size due to phase addition of the moving particles. The Brownian diffusion velocity is inversely proportional to particle size, and is expressed as hydrodynamic radius R_H according to the Einstein equation:

(4.5) $$R_H = \frac{2kT}{3\pi\eta D}.$$

Where D is the translational diffusion coefficient, k is the Boltzmann constant; T is the absolute temperature and η corresponds to the solvent viscosity.

4.2. Experimental

SAXS characterization

The samples were placed in a capillary glass tube (∅ 1.5 mm, glass n° 14, Hildenberg, Malsfeld, Germany). At room temperature the tube was exposed to a 12 keV x-ray beam, which corresponds to a wavelength of 0.13 nm. The beam was focused on a corner of the 2D detector to maximize the range of accessible q values. By placing the 2D detector of DUBBLE at a distance of 1.5 m from the sample, it was possible to measure the scattered intensity in a range of q (scattering vector) values between 0.13 and 5.56 nm^{-1} with successive steps of 0.0109 nm^{-1}. A beam stop was required to shield the detector from the direct beam and to avoid saturation of the outgoing signal. The position of the beam stop is marked by a triangular shadow in Figure 4.1a. The raw data were corrected for the pixel-dependent detector sensitivity and averaged along circles with the same q values. To correct for the contribution of the background a SAXS curve of a capillary containing pure solvent was recorded under the same experimental conditions as the Nb/Si oxide sols (NS*s*).
To reach q values smaller than 0.13 nm the detector was placed at 8 m from the sample and a second set of measurements was acquired at this distance.

Reagents

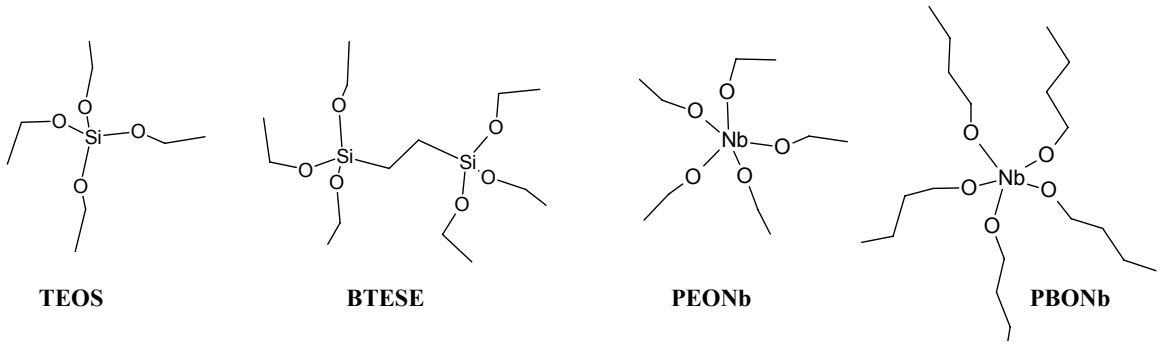

Figure 4.2. Chemical formulae of the metal oxide precursors used in the syntheses.

The metal oxide precursors used in this study are depicted in Figure 4.2. Tetraethyl orthosilicate (TEOS) and 1,2-bis(triethoxysilyl)ethane (BTESE)

were purchased from Aldrich with purities of 99.999% and 96%, respectively. Niobium(V) penta(n-butoxide), hereafter designated as PBONb, and niobium(V) pentaethoxide, hereafter referred to as EBONb, were purchased from Gelest. The purity was not specified. Nitric acid 65%, ethanol (99.8%) and 1-butanol (99.8%) were purchased from Aldrich.

Table 4.1. List of sols including a description of their synthesis.

Sol	Description of synthesis procedure
A-type sols	
A0	Aqueous nitric acid (0.833 ml HNO_3 conc. in 3.9ml of water) was dropped in a mixture consisting of 13 ml of TEOS and 136 ml of ethanol. The mixture was refluxed for 2 h at 60 °C and then used as stock solution for the synthesis of the A-type sols.
A1	5 ml of 1M solution of PEONb in ethanol was added drop by drop to 16.5 ml of sol A0. The mixture was heated at 60 °C for varying periods of time.
A2	5 ml of 1M solution of PEONb in ethanol was added drop by drop to 16.5 ml of sol A0. The mixture was heat at 80 °C for varying periods of time.
A3	5 ml of 1M solution of PBONb in butanol was added drop by drop to 16.5 ml of sol A0. The mixture was heat at 60 °C for varying periods of time.
A4	1 ml of 1M solution of PEONb in ethanol was slowly added to 3.3 ml of sol A0. The so-prepared mixture was diluted in 17.2 ml of ethanol. It was then heated to 60 °C for varying periods of time.
B-type sols	
B0	Aqueous nitric acid (0.181 ml HNO_3 conc. in 0.851 ml of water) was added drop by drop to 3.13 ml of BTESE and 29.7 ml of ethanol. The mixture was refluxed for 2 hours at 60 °C.
B1	5 ml of 1M solution of PEONb in ethanol was added drop by drop to 16.5 ml of sol B0. The mixture was heated at 60 °C for varying periods of time.
$B_\beta 0$	Aqueous nitric acid (0.181 ml HNO_3 conc. in 0.851 ml of water) was added drop by drop to 3.13 ml of BTESE and 17.6 ml of ethanol. The mixture was refluxed for 2 hours at 60 °C.
$B_\beta 1$	12.1 ml of ethanol was added to the $B_\beta 0$ sol to reach a molar composition equal to B0. An aliquot of 16.5 ml of the sol was mixed to 5 ml of 1M solution of PEONb in ethanol. The mixture was heated at 60 °C, but gelled after few minutes.
$B_\gamma 0$	Aqueous nitric acid (0.181 ml HNO_3 conc. in 0.851 ml of water) was added drop by drop to 3.13 ml of BTESE and 8.80 ml of ethanol. The mixture was refluxed for 2 hours at 60 °C.
$B_\gamma 1$	20.9 ml of ethanol was added to the $B_\beta 0$ sol to reach a molar composition equal to B0. An aliquot of 16.5 ml of this sol was mixed with 5 ml of a 1M solution of PEONb in ethanol. The mixture gelled after few minutes.

Sol	Description of synthesis procedure
C-type sols.	
C0	Aqueous nitric acid (0.18 ml of HNO_3 conc. in 2.3 ml of water) was dropped in a mixture consisting of 14.3 ml of TEOS and 15 ml of ethanol. The mixture was refluxed for 2 hours at 60 °C and then used as base for synthesis of the C-type sols.
C1	2.15 ml of PEONb dissolved in 3.20 ml of ethanol was added to 12.7 ml of sol C0. The original rW and rH ratios of sol C0 were re-established by addition of 0.030 ml of nitric acid conc. in 0.385 ml of water. The prepared mixture was heated at 60 °C, for varying periods of time.
C2	8.6 ml of 1 M solution of PBONb in butanol was added to 12.7 ml of sol C0. The original rW and rH ratios of sol C0 were re-established by addition of 0.030 ml of nitric acid conc. in 0.385 ml of water. The prepared mixture was heated at 60 °C for varying periods of time.
D-type sols	
D0	Aqueous nitric acid (0.36 ml HNO_3 conc. in 1.7 ml of water) was dropped into a mixture consisting of 8 ml of TEOS and 84 ml of ethanol. The mixture was refluxed for 2 hours at 60 °C and then used as base for the synthesis of the D-type sols.
D1	2.79 ml of 1M solution of PEONb in ethanol were added drop by drop to 22 ml of sol D0. The mixture was heated at 60 °C for a varying period of time.
D2	0.17 ml of water was added to 22 ml of sol D0. Then 2.79 ml of 1M solution of PEONb in ethanol was dropped to this sol. The mixture was heated at 60 °C for varying periods of time.
D3	Aqueous nitric acid (0.254 ml HNO_3 conc. In 0.082 ml of water) was added to 22 ml of sol D0. Then 2.79 ml of 1M solution of EONb in ethanol was dropped into this sol. The mixture was heated at 60 °C for varying periods of time.

The solvents used were anhydrous to strictly control the water concentration in the system. De-ionized water (ρ=18.2 MΩ cm) was prepared using a TKA water purification unit.

Preparation of samples

To screen the effect of synthetic conditions on sol particle evolution a large number of samples was made. All sols prepared are listed in Table 4.1. Four series of sols were generated following four different synthetic methods. All sols were prepared in a two-step method in which the silica precursor was first prehydrolized for 2 h at 60 °C. The Nb precursor was added to the mixture and

reacted at 60 °C under reflux. Samples for SAXS analysis were collected at 0, 30, 90, 150 and 300 min of reaction time. The A-type sols were prepared by adding all water and acid at once at the beginning of the TEOS pre-hydrolysis step. The B1 sol was prepared following a similar synthetic procedure but by using BTESE instead of TEOS.

The D-type sols were prepared under more diluted conditions than sols A, but with a similar procedure. In the C-type sols water and acid were added in two steps, namely at the prehydrolysis stage and after addition of the Nb precursor. For the sake of simplicity the samples in this chapter will be referred to by the letter that is listed in, followed by the time of reaction in minutes. For example, the NS membrane was prepared from a sol corresponding to a sample synthesized according to procedure C2 after 300 min. of reaction at 60 °C. This sol is thus referred to as C2_300.

4.3. Molar composition of NS*x* sols

The morphology of the sol particles depends on many synthetic parameters, i.e., reaction time and temperature, and concentration of the metal oxide precursors, water and acid.

The concentration of water and acid is often expressed in terms of hydrolysis ratio and acid ratio. In this chapter these parameters are defined by Equations 4.6 and 4.7.

$$rW = \frac{[H_2O]}{\sum_i \upsilon_i [M_i]} \quad (4.6) \qquad rH = \frac{[H^+]}{\sum_i \upsilon_i [M_i]} \quad (4.7)$$

$[H_2O]$ = mols of water/liters of solution
$[H^+]$ = mols of water/liters of solution
$[M_i]$ = mols of water/liters of solution
υ_i = oxidation state of the metal

The concentration of metal oxide precursors was found to be a crucial parameter in the kinetics of hydrolysis and condensation. Thus, we also report for each sample the rS ratio, defined in Equation 4.8. It corresponds to the reciprocal of the concentration of metal atoms.

(4.8) $$rH = \frac{[S]}{\sum_i \upsilon_i [M_i]}$$ [S] = mol of organic solvents/liters of solution

The parameters rW, rH and rS provide a complete description of the molar composition of a sample. These parameters are listed in Table 4.2 for all sols, to allow an easy comparison among samples.

Table 4.2. Molar composition of the sols. The ratios rW, rH and rS are defined in Equations 4.6-4.8.

Sol	Nb:Si molar ratio	rW	rH	rS	Notes*
A0	0	1	0.05	10	
A1	0.80	0.5	0.025	6.3	
A2	0.80	0.5	0.025	6.3	heated at 80 °C
A3	0.80	0.5	0.025	5.6	PBONb was used as precursor
A4	0.80	0.5	0.025	36	high dilution ratio (rS)
B0	0	1	0.05	10	Sols B: BTESE was used as Si source
B1	0.60	0.5	0.025	6.3	
$B_\beta 0$	0	1	0.05	6	
B_β	0.60	0.5	0.025	6.3	Instable sol
$B_\gamma 0$	0	1	0.05	1.5	
B_γ	0.60	0.5	0.025	6.3	Instable sol
C	0	0.5	0.01	1	Sols C: water and acid were added in 2 steps; Nb:Si molar ratio = 0.33
C1	0.33	0.5	0.01	1	
C2	0.33	0.5	0.01	1	PBONb was used as precursor
D	0	0.7	0.35	10	Sols D: Nb:Si molar ratio = 0.33
D1	0.33	0.5	0.025	7.8	
D2	0.33	0.7	0.025	7.8	Higher rW than D1
D3	0.33	0.7	0.1	7.8	Higher rH than D2

*By taking sols A and A1 as references the notes describe the main difference between the actual recipe and those of sols A and A1.

4.4. Results and discussion

Growth of A1 particles

The evolution of sol A1 as investigated by SAXS is reported in Figure 4.3 and Table 4.3. Figure 4.3a was used to follow the evolution of D_f with reaction time. The part of the graph indicated as 'fractal region' was fitted to Equation 4.3. The fractal dimension changed only slightly between 30 and 300 min of reaction time, increasing from 1.64 ± 0.01 to 1.85 ± 0.01.

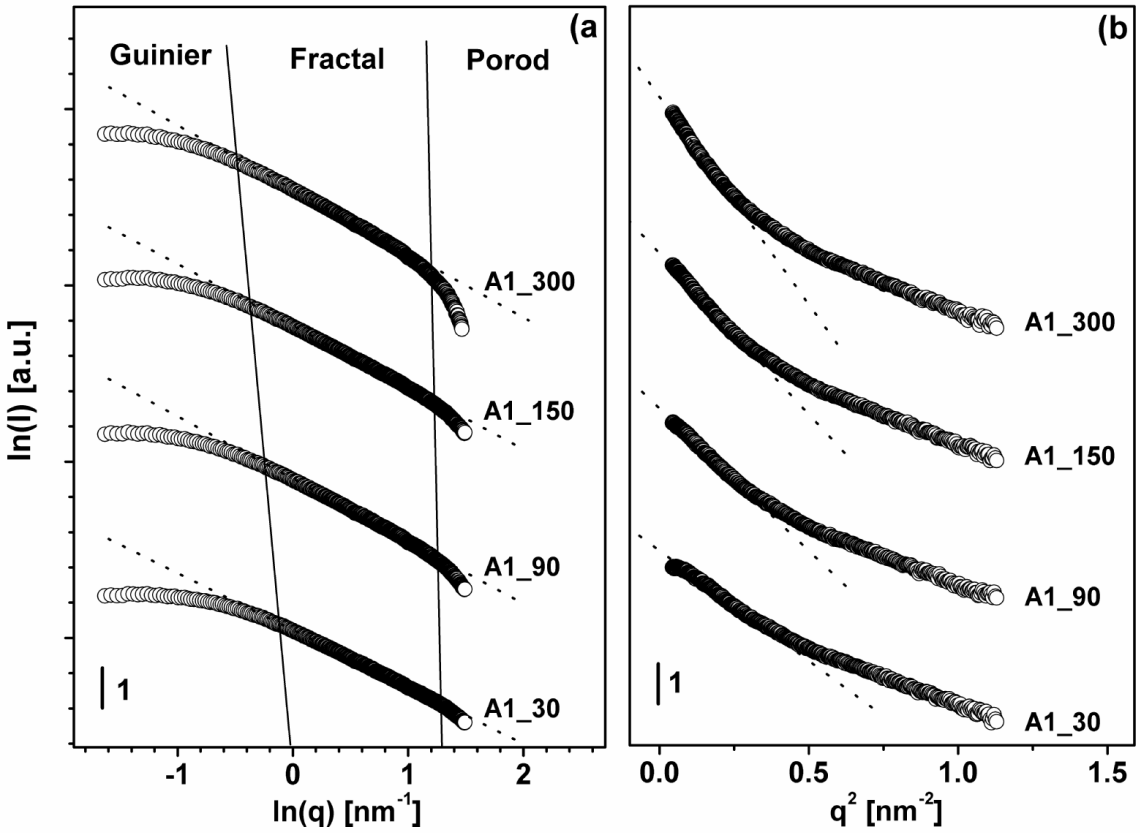

Figure 4.3. Fractal evolution of sol A1, as monitored by SAXS. The four samples were collected at reaction time of 30, 90, 150 and 300 min. In the Porod plot (a) the experimental points (detector-sample distance ~ 1,5 m) were fitted to Equation 4.3 (dotted lines). The vertical black lines were added to guide the eye of the reader in distinguishing the boundaries of the Guinier, fractal and Porod regions in the graph, respectively. In the Guinier plot (b) the experimental data (detector-sample distance ~ 8 m) were fitted to Equation 4.4.

The two threshold values $1/r_0$ and $1/\xi$ that are the boundaries of the fractal

region were chosen for each curve by determining the q values where the following criterion was no longer met:

$$(4.9)\quad \left(\frac{\ln(I)_{\exp} - \ln(I)_{fit}}{\ln(I)_{\exp}} \right)^2 < 0.001 .$$

Here $\ln(I)_{exp.}$ is the natural logarithm of the scattered intensity as experimentally measured (white circles in Figure 4.3a) and $ln(I)_{exp}$ is the corresponding value as calculated by linear fitting (dotted lines in Figure 4.3a). The position of $1/r_0$ and $1/\xi$ in the four A1 curves are indicated in Figure 4.3a by the black vertical lines. These lines have no physical meaning, but only serve as a guide to the eye of the reader. The radius of the primary scatterers of the fractals, with size r_0, of A1_30, A1_90 and A1_150 change only slightly with time and typical values are 0.21-0.23 nm. These values are similar to those reported de Lange [6]. Only for A1_300 a r_0 of 0.27 nm was calculated from the data. It is not clear if the deviation from the general trend exhibited by A1 is due to a physical property of the A1_300 sol, or an artifact that is due to the rather low intensity of the signal at high q values of the SAXS spectrum.

Table 4.3. Evolution of the A1 sol with time, as monitored by SAXS. The fractal dimension (D_f), the primary particle radius (r_0) and the parameter ξ were calculated from the Porod plot in Figure 4.3a, as described in the text in more detail. The gyration radius was calculated by fitting Equation 4.4 to the Guinier plots of Figure 4.3b.

Time [min.]	D_f [-]	r_0 [nm]	ξ [nm]	R_g [nm]
30	1.60 ± 0.01	0.21	2.04	2.56 ± 0.05
90	1.73 ± 0.01	0.23	2.24	2.97 ± 0.03
150	1.72 ± 0.01	0.23	2.29	3.37 ± 0.04
300	1.81 ± 0.01	0.27	2.35	3.86 ± 0.08

The position of $1/\xi$, instead, shifted towards lower q values by increasing reaction time. This is a direct consequence of particle growth, since ξ is directly related to R_g. The gyration radii of the four A1 sols were measured in a Guinier plot by fitting the data acquired at the longest detector-sample distance to Equation 4.4. The R_g of sol A1 was determined to be 2.56 ± 0.05

nm after 30 minutes of reaction time, 2.97 ± 0.03 nm after 90 min, 3.37 ± 0.04 nm after 150 min and 3.86 ± 0.08 nm after 300 min.

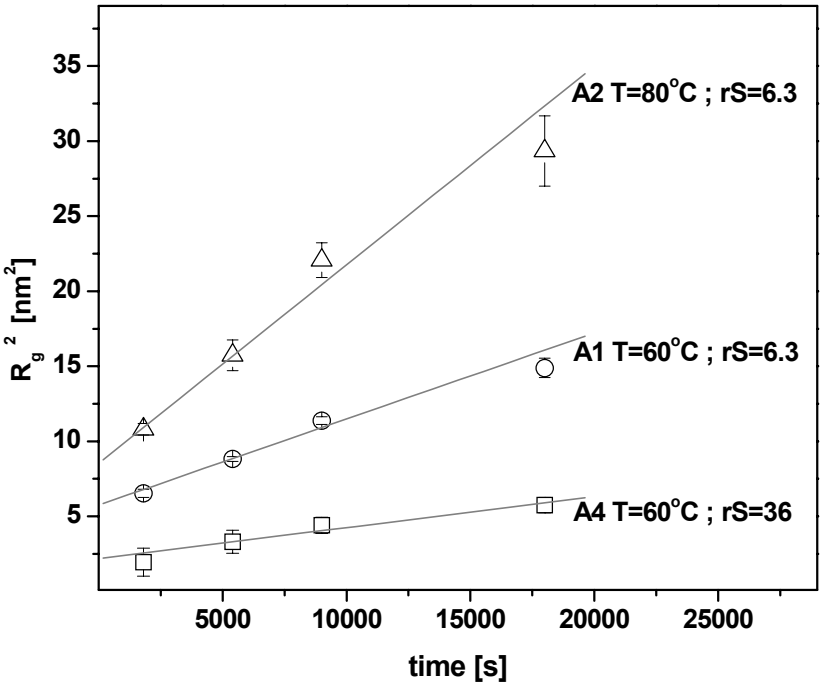

Figure 4.4. Evolution of the particle size of sols A1, A2 and A4 with time. The growth curve of each sol was fitted to Equation 4.10.

These values are shown in Figure 4.4 together with the corresponding R_g values as calculated for the A2 and A4 samples. The figure shows that the growth of these particles can be fitted within experimental error on a law of the type [7]:

(4.10) $$R_g^2 = R_0^2 + k_D \cdot t \,.$$

Here k_D is constant depending on the molar volume of the metal oxide clusters in solution, and the diffusion coefficient of the momoners. In reality, the hydrolysis and condensation of a silicon precursor and a niobium precursor is a complex process in which hydrolysis and condensation of numerous species occur at the same time, generating new condensed reactive species. For this reason, k_D is an empirical parameter that is used in this chapter only to compare the growth rate of particles of different sols quantitatively. The

parameter R_0 indicates the gyration radius at t=0. The parameters k_D and R_0 are listed in Table 4.4 for the A, C, and D-type sols.

R_0 was experimentally determined by extrapolation. Table 4.4 allows comparison of the R_0 values of the A-type sols. These values vary between 3.2 and 1.5 nm. These values are larger than 1.1 nm, which is the R_g of the A0 sol as extrapolated from the Guinier plot of its SAXS pattern. It is well possible that R_0 of the other A-type sols is somewhat larger, because the reaction in the early stages of synthesis may be governed by mechanisms that are not in accordance with Equation 4.10 [3].

The fact that R_g^2 is a linear function of reaction time indicates that the growth of niobia-silica particles is probably dominated by a homogeneous diffusion-controlled process, i.e., the supply of monomers to the growing particles is probably rate-determining. Diffusion-controlled growth has also been reported by Nair et al. [3] for pure silica polymers, and by De Lange et al. [6] for Ti- and Zr-doped silica polymers.

Growth of NS*s* particles: general considerations

Figure 4.5 shows the fractal dimension of the NS*s* sols as a function of gyration radius R_g. The pure silica sols, namely A0, B0, C0 and D0, are not shown in this graph since the signal/noise ratio in their SAXS patterns was too low to allow proper analysis of the data.

Table 4.4. Parameters from Equation 4.10, as calculated for sols A, C, and D-type sols.

Sol	k_D [$m^2 \cdot s^{-1}$]	R_0 [nm]
A1	$(5.7 \pm 0.4) \cdot 10^{-22}$	2.4 ± 0.1
A2	$(1.3 \pm 0.1) \cdot 10^{-21}$	2.9 ± 0.2
A3	$(4.1 \pm 0.3) \cdot 10^{-22}$	3.2 ± 0.1
A4	$(2.1 \pm 0.5) \cdot 10^{-22}$	1.5 ± 0.5
C1	$8.5 \cdot 10^{-22}$	0.5
C2	$(7.6. \pm 0.3) \cdot 10^{-22}$	1.3 ± 0.2
D1	$(6.6 \pm 0.7) \cdot 10^{-23}$	1.00 ± 0.04
D2	$(5.3 \pm 0.3) \cdot 10^{-22}$	0.3 ± 0.3
D3	$(5.9 \pm 0.1) \cdot 10^{-22}$	1.19 ± 0.01

Niobia-silica sols, prepared by using TEOS as silicon source, have D_f values between 1.5 and 1.9. In the early stages of sol development the fractal dimension increases with gyration radius. However, when the sol particles exceed the threshold $R_g \sim 4$ nm the fractal dimension appears to remain constant at a threshold value equal to 1.9. The

existence of an upper limit for the D_f of growing silica polymers has also observed in previous works, for instance by Meane et al. [8] for silica polymeric sols, and by Peterlik et al. [9] for silica-alumina sols. According to theoretical calculations [10] a final fractal dimension of about 1.8 agrees well with a diffusion limited growth mechanism. Only objects with fractal dimensions below 1.5 can freely interpenetrate each other. For this reason Brinker [11] proposed the requirement $D_f \leq 1.5$ for a metal oxide sol to be able form a microporous network. In reality, the calculated D_f is the mean of a broader distribution. Particles with a fractal dimension higher or smaller than this average are also present in the sol. Hence it should also be possible to obtain microporous materials from sols with D_f slightly above 1.5. This may explain why the microporous NS membrane reported in the previous chapter was prepared by C2_300 sol, for which a D_f of 1.8 was calculated.

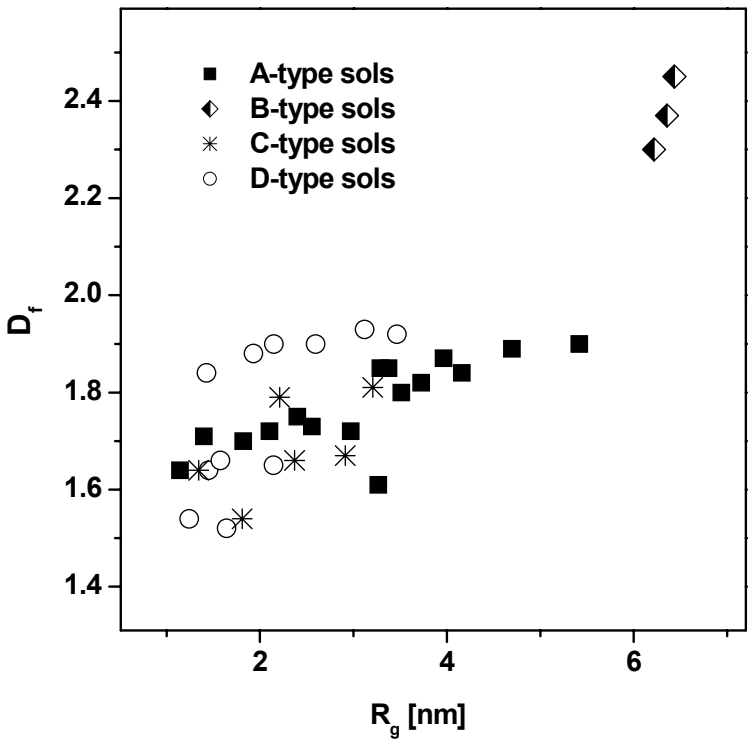

Figure 4.5. Fractal dimension (D_f) of the NS*s* sols described in this work as function the gyration radius R_g.

The fractal dimension of the sols with rW = 0.7, i.e., D2 and D3, increased to 1.8-1.9 in the early stages of syntesis, when the gyration radius of the particles was still below 2 nm. The reaction of D2 and D3 was not followed after 300 min, thus it is not possible to determine if their fractal dimensions increased further at longer reaction times.

It is noted that none of the niobia-silica sols analyzed in this study have a D_f value smaller than 1.5. Even those sols with a low degree of condensation and

an R_g value smaller than 2 nm have a D_f value larger than 1.5. This cannot be attributed to the reactivity of TEOS, because this precursor typically yields silica sols with D_f between 1 and 1.5 [3,6-8] under acid-catalyzed conditions. When pure TEOS was reacted at the same hydrolysis and acid ratios and for similar reaction times, sols were obtained that consisted only of small clusters, too small to be analyzed by scattering techniques. Hence, the presence of a lower limit to the fractal dimension of the sol particles is most likely due to the use of Nb-alkoxides in the preparation of the sols under study here. Probably, Nb precursors already form clusters with a definite non-linear shape in the earliest stages of synthesis. At high Nb loading, this leads to the formation of particles with a fractal dimension higher than 1.5. Attempts to synthesize NS *s*ols with rW ≤ 0.025 and a Nb:Si molar ratio of 0.33 yielded sols which too low scattering power it was not possible to calculate a reliable fractal dimension value: $D_f < 1$ was measured.

When TEOS was substituted by BTESE as silicon source (B1 sols), fractal dimensions between 2.30 and 2.45 were measured at rW = 0.5 and rW = 0.025. The gyration radii measured for the B1 sols were larger than 6 nm. It should be noted that the Nb : Si molar ratio in the B-type sample was equal to 0.6. Thus, statistically one Nb-O bond was available for each Si-O bond, as for the A sols. But the B-type sols were larger than any of the A-type sols prepared under similar conditions. The larger dimensions of the B1 sols are probably due to the higher reactivity of the silicon atoms in BTESE compared to TEOS. The silicon atoms in BTESE have a higher reactivity because of the inductive electron-donating effect of the ethylene bridge. An additional explanation for the high fractal dimension of the B1 sols can be given by taking the nature of the precursors into consideration. The number of alkoxide groups present in TEOS is 4, it is 5 in PEONb and PBONb, and 6 in BTESE. Hence, on the basis of statistics alone it is expected that BTESE-containing polymers have a higher degree of intrachain branching than TEOS-based sols. Since D_f is a measure of the degree of branching, the D_f of BTESE-based sols is expectedly higher.

Effect of the temperature on the particle growth

To study the effect of temperature on the kinetics of particle growth, sols A1 and A2 were prepared with the same molar composition. However, they were heated under reflux at 60 and 80 °C, respectively. By applying Equation 4.10 to the data reported in Figure 4.4, a growth rate constant k_D equal to $(5.7 \pm 0.4)\cdot10^{-22}$ m^2·s^{-1} was obtained for A1, and $k_D = (1.3 \pm 0.1)\cdot10^{-21}$ m^2·s^{-1} for A2. Although these two values do not permit calculation of the temperature dependency of the diffusion coefficient D, they illustrate how strongly the reaction temperature affects the kinetics of sol particle growth. After a reaction time of 300 min, an R_g value of 3.56 ± 0.08 nm was calculated for A1. The radius of A1 under otherwise similar conditions was 70% smaller than that of A2.

Effect of dilution on particle growth

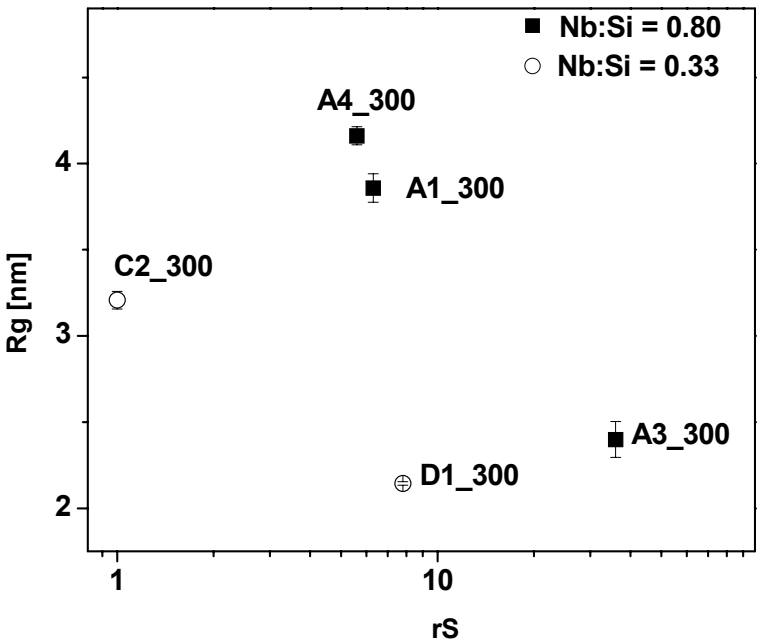

Figure 4.6. Gyration radius (R_g) of sol particles as function of the dilution ratio (rS). Reflux time of all samples was 300 min. at 60 °C..

Figure 4.4 shows the temporal evolution of A4 sol particles. As depicted in Table 4.2, sol A4 has the same molar composition as A1, except for the dilution ratio rS. The degree of dilution affects the growth rate of sol particles strongly. For A4 a k_D value of $(2.1 \pm 0.5)\cdot10^{-22}$ m^2·s^{-1} was calculated from the experimental data. By diluting the A1 sol 6 times before reaction started, the value of R_g was equal to 2.4 ± 0.1 nm after 300 at 60 °C. In this case the diffusion rate of the monomeric species within the solvent remained constant since the reactions leading to A1

and A4 were performed in the same solvent and at the same temperature. However, because the reaction took place in a more dilute medium the number of collisions per second was lower for A4 than for A1. Thus, the value of k_D is also expected to be lower for A4 than for A1.

The strong influence of the degree of dilution is stressed in Figure 4.6, where sols are compared on the basis of their dilution ratios. Figure 4.6 compares sols with similar rW and rH ratios, all prepared at 60 °C and a reaction time of 300 min. Dilution affects the particle growth rates of NS*s* sols with Nb : Si molar ratios of both 0.8 and 0.33. Clearly, for both Nb : Si ratios, R_g decreases with increasing rS.

Effect of composition on particle growth

The results depicted in Figure 4.6 suggest that the evolution of R_g with time depends to a large extent on the Nb : Si molar ratio. In agreement with expectation, sols with lower Nb : Si molar ratios have lower R_g values. This can be explained by the higher reactivity of the niobia precursors compared to TEOS.

Effect of rW on particle growth

Sol D2 was prepared at a higher hydrolysis ratio than D1. In the synthesis of D3 more nitric acid was used than in preparation of D2. The evolution of these three sols with time is presented in Figure 4.7. The D-type sols were prepared at lower Nb:Si molar ratio and in a more diluted mixture than the A-type sols. Generally, the scattered intensity of the D-type samples was lower than that of the A-type. Thus there was more uncertainty about the actual R_g for this set of measurements than on the A-type sample, although the standard deviations of the linear regression are comparable to those reported in Figure 4.4.

The particle growth of D-type sols well fit to the diffusion-limited aggregation model of Equation 4.10. A k_D of $(6.6 \pm 0.7)\cdot10^{-23}$ $m^2\cdot s^{-1}$ was measured for D1 sols and of $(5.3 \pm 0.3)\cdot10^{-22}$ $m^2\cdot s^{-1}$ for the D2 sol. The D1 sols were prepared at rW = 0.5, while for D2 a hydrolysis ratio of 0.7 was used. According to the

schemes in Figure 2.1 and 2.3 one molecule of water is consumed for each two Si-O bonds that are added to a linear polymer. Thus, the presence of water in the system is of great importance to obtain a sol with R_g of few nanometers. For instance, attempts to prepare a niobia-silica sol at rW = 0.25 yielded poorly developed sols also after reacting for a few hours at 60 °C. As already mentioned it was not possible to analyze these sols prepared at rW = 0.25, due to the low signal/noise ratio. The rate of growth of the D2 particles was higher than the rate of growth of in D1, probably because of the higher concentration of Si-O-H and Nb-O-H groups in D2 than in D1. Remarkably, D2 and D3 that were synthesized at the same rW ratio showed similar k_D values, as reported in Table 4.4.

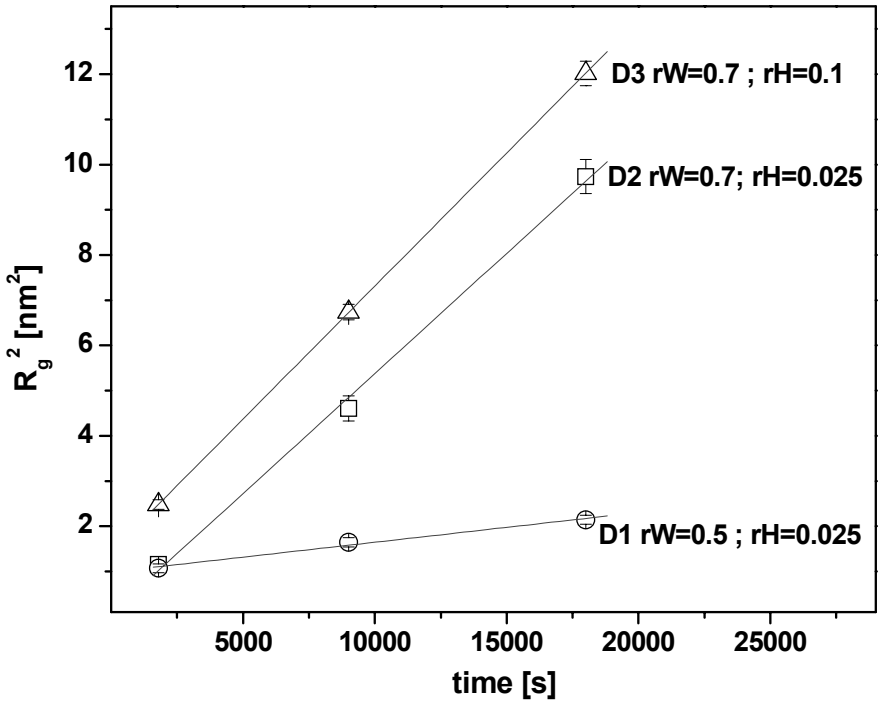

Figure 4.7 Evolution of the particle size of sols D-type sols with time. The growth curve of each sol was fitted to Equation 4.10.

Effect of rH on particle growth

All samples reported here were prepared at an rH large enough to ensure that hydrolysis and condensation occurred under acid catalyzed conditions. These

conditions are of extreme importance to obtain slightly branched and stable polymeric sols, as elucidated in Section 2.1, on pages 18-23. The acidity ratio was equal to 0.025 in D2 and to 0.1 in D3. As already stated, after 30 min of reaction time the growth rate of D2 and D3 was similar, with a k_D of about 5-6·10^{-22} m·s^{-2}. However after a reaction time of 30 min D3 had an R_g of 1.54 ± 0.03 nm, while D2 had an R_g of about 1.1 nm. Thus, in the first stages of reaction, the particle growth was increased by increasing the concentration of acid.

The overall polymerization reaction does not consume or create protons. The acid acts as a catalyst in both hydrolysis and condensation reactions. Hence, *rH* affects the kinetics of reaction, while it is unlikely that it would affect the diffusion rate under the reaction conditions employed here. This suggests that particle formation and growth in the early stages of reaction occurs under reaction-limited conditions [7]. The scattered intensity of the D00 sol was extremely low, close to that of pure ethanol. Hence, after 2 hours of pre-hydrolysis, D00 probably consisted of small silica clusters only. After introduction of 1M PEONb, at reaction time t = 0, the sol was formed by solvated silica-niobia clusters and monomers in parallel. Indeed, the solvent ratio *rS*=7.8 correspond to about 33 molecules of ethanol per metal atom. Under these conditions diffusion is probably not the rate-determining step, however the reaction rate between molecules could be. However, after a relatively short time, nucleation centers are formed from relatively large numbers of monomers, after which the diffusion of monomers to these centers becomes rate determining. Nair [3] already proposed a shift from a reaction limited process to a diffusion limited process in synthesis and aging of pure silica polymeric sols.

The importance of *rH* in the early stages of reaction was confirmed by the fact that D1 and D2, which were synthesized at the same *rH* ratio, both had a gyration radius about 1.1±0.1 nm after the first 30 minutes of reaction.

Effect of the niobia precursor

Figure 4.8 shows the evolution of two sols (A1 and C1) that were prepared by using PEONb as niobia precursor, and two sols synthesized by using PBONb, i.e., A3 and C2. For A3, the parameter k_D was calculated to be $(4.1 \pm 0.3)\cdot10^{-22}$ $m^2 \cdot s^{-1}$. Hence, k_D is smaller for A3, prepared by using PBONb than for A1, which was prepared under the same synthetic conditions but using PEONb. The same trend was observed for the couple C1 and C2, as reported in Table 4.4.

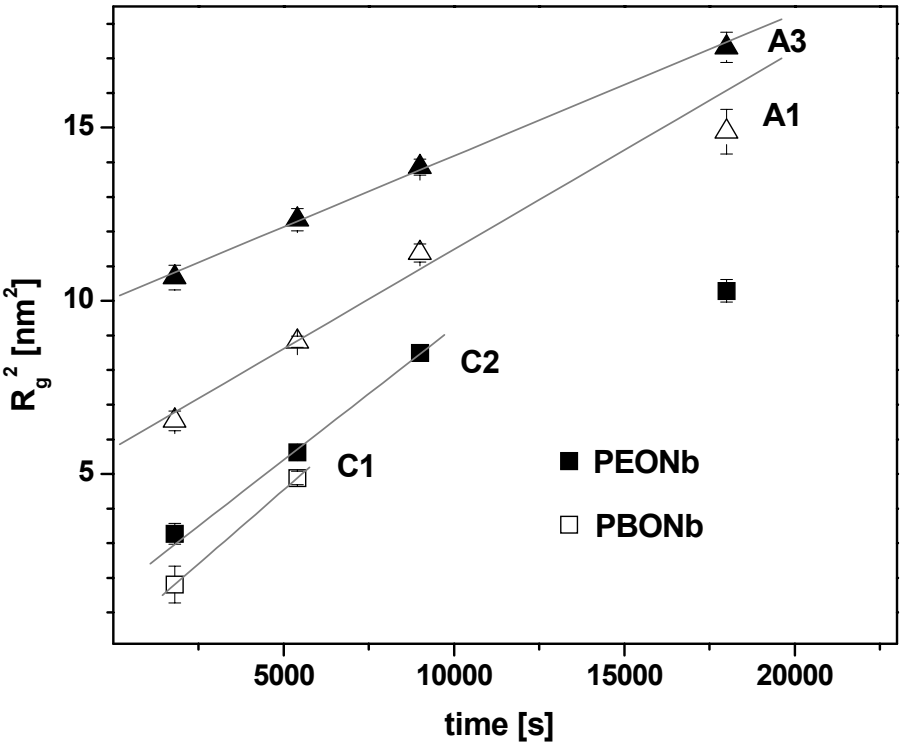

Figure 4.8 . Evolution of the particle size of sols A1, A3, C1 and C2 with time. The growth curve of each sol was fitted to Equation 4.10

This can be explained by the fact that an appreciable amount of 1-butanol was present in A3 and C2, which was introduced together with PBONb, and was also formed during the hydrolysis of PBONb. 1-Butanol has a viscosity equal to 3.0 cP at 25°C, which is almost three times higher than that of ethanol (1.074 cP). Hence the diffusion of the niobia-silica clusters is reasonably slower in A3 than in A1, and slower in C2 than in C1. The parameter R_0 is also

smaller in the PBONb containing sols than in their homologues generated from PEONb. The hydrolysis rate of PEONb is expected to be lower than that of PEONb, because of the steric and electronically stabilizing effect of the butoxy substituents. However, dedicated studies on the reactivity of Nb alkoxides have not been reported, so we do not have experimental evidence to support any specific explanation.

Quenching effect of the silica precursor on Nb/Si oxide particles

The number distribution of hydrodynamic radii of three bridged silica sols that were prepared by heating a mixture of BTESE dissolved in acid ethanol for two hours at 60 °C are reported in Figure 4.9. At the beginning of the reactions rW was equal to 1.0 and rH was 0.05 in all samples, while rS was varied from 10 for sol B0 to 3 for the sample $B_\gamma 0$; sample $B_\beta 0$ was prepared with an rS equal to 6. The rate at which the particle formed and grew increased by increasing the concentration of BTESE in the sol. After reacting for 2 hours at 60 °C the number average hydrodynamic radius was equal to 0.5 nm for B0 (rS = 10), it was 0.7 nm in sample $B_\beta 0$ (rS = 6) and 1.3 nm for sample $B_\gamma 0$ (rS = 3), which was the most concentrated sol. A sample was also prepared at rS = 1.5; but it gelled after about 100 min of reaction at 60 °C. After a reaction time of 2 hours, ethanol was added to sols $B_\beta 0$ and $B_\gamma 0$ to bring the rS ratio to 10, so that the nominal composition was the same as B0 for all the samples. DLS measurements were performed after this addition.

Then a 1 M solution of PEONb in ethanol was added to all the samples to get a final molar composition Nb:Si equivalent to 0.6. Although all samples had the same molar composition, they reacted differently to the addition of the PEONb. Sample B_γ gelled as soon as PEONb was added; sample B_β gelled after the sol had been raised to a temperature of 60 °C. Sample B1 was heated for 5 hours at 60 °C and the evolution of size and fractal dimension are shown in Figure 4.5. The outcome of the reaction depends on the concentration of silanol groups in the system at the moment that the niobia precursor is added to the mixture.

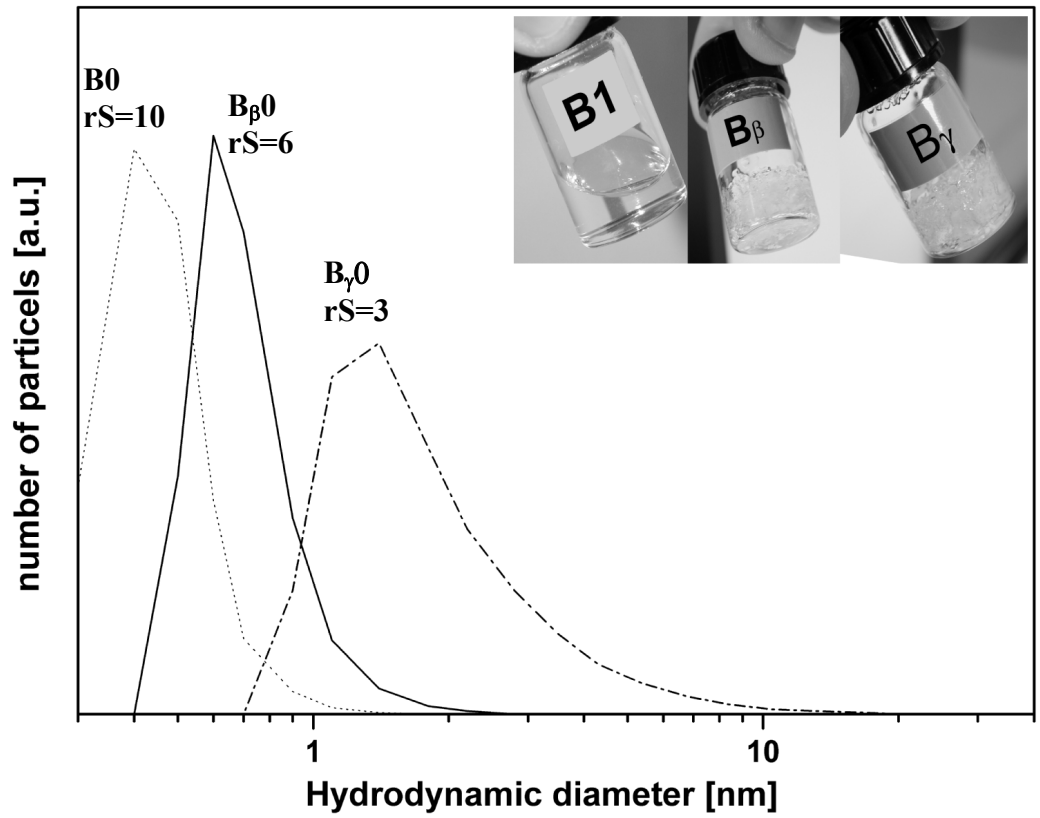

Figure 4.9 Hydrodynamic diameter distribution of B, $B_\beta0$ and $B_\gamma0$ as measured by DLS. The sols were refluxed for 2 h. After that time ethanol was added to $B_\beta0$ and $B_\gamma0$ to reach the molar composition of B0. The distributions were calculated from the DLS correlogram by using the CONTIN method. Inset shows B-type sols after addition of 1 M solution of PEONb in ethanol. B1 yielded a stable suspension; B_β and B_γ gelled after a few minutes after addition of the precursor

The highly reactive niobia precursor undergoes hydrolysis when it is brought into contact with the water containing mixture to yield Nb-OH groups. Then the hydroxyls on the niobium atoms can undergo condensation with other Nb-OH groups or with silanols. This latter reaction is preferred because it would result in a niobia-silica network that is mixed at the atomic level. The data reported here suggest that the condensation of highly reactive Nb-OH groups with less reactive Si-OH groups could also help to control the condensation rate. Despite the fact that the three sols had the same nominal composition when the niobium precursor was added, the concentration of silanol groups and of free water was different, depending on the extent to which the

hydrolysis and condensation reactions occurred during the previous two hours of reaction at 60 °C. To ensure homogeneous mixing of Si and Nb, it is necessary to maximize the concentration of silanols at the moment of incorporation of niobia. This can be accomplished by maximizing the degree of hydrolysis of BTESE, and minimizing the degree of condensation. As shown by the DLS measurements in Figure 4.9, the degree of condensation in the samples was in the order $B_\gamma 0 > B_\beta 0 > B0$. The fact that the silanol groups indeed suppress gelation is indicated by the fact that the sol stability of PEONb precursor follows the reverse order, i.e., $B_\gamma < B_\beta < B1$.

4.5. Conclusions

The data reported here suggest that the growth of niobia-silica fractalic sols follows a diffusion limited growth mechanism. When TEOS was used as silica precursor the fractal dimension converged to a value of 1.8-1.9. The data presented in this study showed that a hydrolysis ratio rW = 0.5 seems to be favorable to obtain nanosols with a fractal dimension in the range 1.5 – 1.9. Sols prepared at rW ≤ 0.25 were not well developed. In the present study sols prepared with rW = 0.7 did not show fractal dimensions larger than 1.9. However, it is possible that different results would be obtained when reaction times would be longer. Also the acid ratio, $0.01 \leq rH \leq 0.1$ helps to obtain niobia-silica sols with an R_g in the nanometer region. Dilution and moderate reaction temperature can be used to slow down the reaction rate in order to control the size of the particles precisely.

This study showed that SAXS is a powerful technique for screening a large number of synthetic conditions. However, it is stressed that R_g and D_f are mean values of a distributions of particles with different size and fractal dimension. No polydispersities of the samples can be obtained from the experimental data, nor any information on the chemical homogeneity of composition of the cluster. For this reason a further study on the consolidated state is required.

4.6. References

[1] B.B. Mandelbrot, The Fractal Geometry of Nature, W.H. Freeman. New York, 1982, p123.

[2] C.J. Brinker; G.W. Scherer, Sol-gel Science, Harcourt Brace Jovanovich, Boston, 1990, p. 779.

[3] B.N Nair, W.J. Elferink, K. Kaizer and H. Verweij, J. Coll. Interface Sci., 178 (1996) 565.

[4] R.J Roe, Methods of X-ray and Neutron Scattering in Polymer Science, Oxford University Press, New York, 2000.

[5] K.S. Schmitz, An introduction to dynamic light scattering by macromolecules, Academic Press, Boston, 1990.

[6] R.S.A de Lange, J.H.A. Hekkink, K. Keizer and A.J. Burggraaf, J. Non-Cryst. Solids, 191 (1995) 1.

[7] G. Cao, "Nanostructures & Nanomaterials – Synthesis, Properties and Applications", Imperial College Press, London, 2004.

[8] N. Meane, B.N. Nair P. D'Hooghe, S.-I. Nakao, K. Keizer, J. Sol-Gel Sci. and Tech. 12 (1998) 117.

[9] H. Peterlik, H. Rennhofer, V. Torma , U. Bauer, M. Puchberger, N. Hüsing, S. Bernstorff, U. Schubert, J. Non-Cryst. Solids 353 (2007) 1635.

[10] P Meakin, J. Sol-Gel Sci. Technol. 15 (1999) 97.

[11] C.J. Brinker; G.W. Scherer, Sol-gel Science, Harcourt Brace Jovanovich, Boston, 1990, p. 779.

[12] This thesis, section 2.1.

CHAPTER 5

Development of niobia-silica membranes: fabrication and characterization

Abstract:

Two disk membranes were prepared and their permeabilities compared to that of the NS membrane. One sample, here name NS2, was prepared by a sol with the same molar composition as the NS sol but with smaller particle size. The other sample, called NS3, was prepared by a sol which had particle size similar to NS, but higher Nb : Si molar ratio than NS and NS2. The hydrogen and helium permeabilities of the NS2 membrane was a factor of ten lower than that of NS. The low permeance of NS2 is probably related to the low degree of structural evolution of the NS2 coating sols. By comparing NS to NS3, it appears that the increase in the loading of Nb ions causes a densification of the material. Single gas permeation measurements showed a preferential permeability towards helium at 200 °C for membranes, especially for the NS3 sample. A tubular membrane was prepared by coating the NS sol on the outer part of an alumina support and named NSt. The pore size distribution measured by nanopermporomtry shows two distinct peaks. One peak was centered at a Kelvin diameter (D_K) value of about 3 nm, which corresponds to the pore diameters of the γ-alumina layer underneath. A second peak was present in the ultramicropore region between 0.3 nm and 1 nm. Despite a certain amount of defects on the membrane surface, the He/N_2, He/CH_4, H_2/N_2 and H_2/CH_4 ideal permselectivities of the NSt tubular membrane were higher than the selectivity of a membrane in which pure Knudsen transport occurs. Hence, although the coating process is not yet optimized, NSt indicates that Nb/Si oxide membrane may be applied to real separation modules.

5.1. Introduction

The development of niobia-silica-type (NSs) membranes is still in an early stage. The previous chapter showed that, in the synthesis stage, we were able to act on the size of the sol particles and on the composition of the sol. Unfortunately, I was not able to tune the fractal dimension of the sol at the high Nb loading used for my syntheses. This is probably due to the formation of clusters with a definite shape in the earliest stages of synthesis. We assume that these clusters influence the growth of the material during later stages of synthesis. At high Nb loading, this leads to the formation of particles with a fractal dimension (D_f) between 1.5 and 2. This indicates that obtaining control over the structure of NSs sols is more problematic than in the synthesis of silica sols, for which it is possible to set the fractal dimension to any value between 1 and 3 by adjusting the concentration of water and nitric acid in the system. This is in agreement with expectation since the porosity and pore structure of silica can be controlled easier than any other material, as discussed in Chapter 2.

The impossibility to vary the fractal dimension of the NS sol particle makes the fabrication procedure from coating to calcination more complicated. As was elucidated in the previous chapter, the synthesis of Nb-doped silica sols often yields particles with a fractal dimension of about 1.7-1.8. This value is higher than the threshold value of 1.5 that was indicated by Brinker as the upper limit for obtaining a microporous network from a sol [1,2]. However, the fractal dimension measured by SAXS is an average value. Particles with fractal dimension above and below the calculated one are most likely also dispersed in the sol, which was initially obtained by mixing two alkoxides precursors. Hence, the pores in the final calcined material may have different dimensions and only a fraction of the total pore volume may actually facilitate molecular sieving. A large number of parameters play a role in the fabrication of a membrane, i.e., sol concentration and viscosity, deposition rate, type of support, calcination temperature, calcination time and heating/cooling rates of the furnace. Furthermore, prior to calcination, a membrane can be aged under

certain conditions to control the evaporation rate of the solvent during consolidation [3]. This is the case with γ-alumina membranes, which are aged in a climate chamber (60% humidity at 40 °C) for 3 h [4]. Because of the complexity of the process, it is not yet possible to construct a general model that can predict the main membrane properties (porosity, pore size distribution, and layer thickness) from the fabrication procedure. The development of ceramic membranes is therefore still carried out by experimental approaches [5].

In this chapter the fabrication and characterization of two supported niobia-silica disk membranes are described and their properties are compared to that of the NS membrane reported in Chapter 3. The properties of the membranes such as permselectivity and permeability are correlated with the characteristics of the sol from which the films were generated. These experiments aim to establish an understanding of the relationship between sol structure and membrane properties.

A tubular membrane was prepared from the same sol that had been used for the preparation of NS and it was calcined under the same conditions. The tubular membrane is referred to as NSt in this chapter. NSt demonstrates the possibility to apply Nb-doped silica membranes in real separation modules.

5.2. Experimental part

2.1 Synthesis and characterization of sols

The NS, NS2 and NSt membranes were prepared by using the group of sols that were named C2 in the previous chapter. The C2 sol was heated to 60 °C under reflux for 90 min in case of NS2, and for 300 min in the case of NS and NSt. NS3 was prepared by using the A3 sol after reflux at 60 °C for 90 min.

Dynamic light scattering (DLS) measurements were performed on a Malvern Zetasizer HS3000. The small-angle x-ray scattering (SAXS) measurements were performed at DUBBLE in Grenoble, France, as described in the previous chapter.

Powders preparation and analysis

Aliquots of the sols dried in air and calcined at 500 °C for 3 h, with a heating/cooling rate of 0.5 °C/min The presence of crystalline phases in these powders was determined by XRD analysis using a Philips SR5056 with Cu Kα radiation.

Membrane coating

The disk membranes were fabricated as described on page 40. Also in this case an α-alumina disk (2 mm thick, ∅ 39 mm) was used as support. The support was polished on one side and coated with a 6% La-doped γ-alumina film of about 2 μm thickness. The dip coating procedures were performed in a class 1000 clean room. The coatings were performed after dilution of the NS*s* sols. The extent of dilution is reported in Table 5.1 for each sol. The membranes were calcined in air at 500 °C for 3 h, using heating and cooling rates of 0.5 °C/min.

The coating of the tubular membrane NSt was performed onto the outer part of an alumina tube provided by ECN (Energy research Centre of the Netherlands, Petten, The Netherlands) as reported elsewhere [6]. The tubular support consisted of an asymmetric α-alumina tube, polished on its external part and covered with a thin layer of mesoporous γ-alumina. This configuration resembles that of the flat membranes. The NSt sol was dip-coated on the tube with a withdrawal speed of 5 mm/s. Subsequently, the tubes were calcined at 500 °C for 3 h with 0.5 °C/min heating and cooling rates.

Measurement of gas permeance

The He, H_2, CO_2, N_2, CH_4 and SF_6 permeances of a disk-shaped γ-alumina support and of the microporous membranes coated on such supports were measured in a dead-end mode permeation set-up. The gas flow was measured with a soap film flow meter, while the overpressure across the membrane was kept at a pressure of 4 bar. The permeation rates of the different gases were determined in a sequence starting with the one with the smallest kinetic

diameter, from helium to SF_6. For each probe molecule the temperature of the furnace was varied step-wise from 200° C to 50 °C. Since atmospheric water can condense in micropores at these temperatures, all membranes were dried in a hydrogen flow for at least 16 h after the temperature had been raised to 200 °C.

The permeance of the tubular membrane was measured at the ECN laboratory, in Petten, in a set-up similar to that used for the characterization of the flat membranes.

5.3. Results and discussion

Table 5.1 provides information about the coating sols that were used for membrane preparation. Three coating sols were prepared according to two-step synthetic procedures, which consisted of the prehydrolysis of tetraethyl-orthosilicate (TEOS, 99.999% purity, Aldrich) in ethanol for two hours at 60 °C, and the subsequent reaction of the formed silica sol with niobium(V)penta(n-butoxide) (Gelest). Sols NS and NS2 were prepared by adding the water necessary for the reaction in two doses, namely at the beginning of prehydrolysis, and after addition of the Nb-alkoxide precursor.

Table 5.1 Properties of the coating sols used for the fabrication of the membranes presented in this chapter.

Membrane	Nb : Si*	D_f #	R_g [nm]§	R_H [nm]†	Dilution (v/v)‡
NS	0.33	1.8	3.2±0.1	3.9±0.7	9%
NSt	0.33	1.8	3.2±0.1	3.9±0.7	25%
NS2	0.33	1.7	2.4±0.1	3.1±0.5	4%
NS3	0.80	1.8	3.5±0.1	3.7±0.5	4%

*Molar ratio of the alkoxides precursors; #Fractal dimension as measured by SAXS; §Gyration radius as measured by SAXS; †Hydrodynamic radius as measured by DLS (average in number); ‡dilution in ethanol before coating, expressed in terms of volume of sol/volume of final coating solution.

NS3 was prepared by adding all water at once, at the beginning of hydrolysis of TEOS. NS3 also differed from the other two sols with respect to the Nb : Si

molar ratio, since it is richer in Nb than the other materials. NS and NS2 sols were prepared following the same procedure and conditions, except for the reaction time after addition of niobium(V) penta(n-butoxide). In the case of NS2 the sol was refluxed at 60°C for 90 min, while the reflux time was 300 min in the case of NS.

The fractal dimension (D_f), gyration radius (R_g) and hydrodynamic radius (R_H) of the sols have already been presented in the previous chapter. They are also summarized in Table 5.1 to facilitate direct comparison of data. All sols have a similar fractal dimension, but they are considerably different with respect to the size of the particles. From the SAXS measurements it was concluded that the NS sol was composed of particles with a main gyration radius (R_g) of 3.2 ± 0.1 nm. The NS2 had an R_g of 2.4 ± 0.1 nm, and NS3 of 3.5 ± 0.1 nm. The hydrodynamic radii measured by DLS showed a similar trend: NS,NS3 > NS2. From these data it appears that the NS and NS3 sols had developed further than NS2.

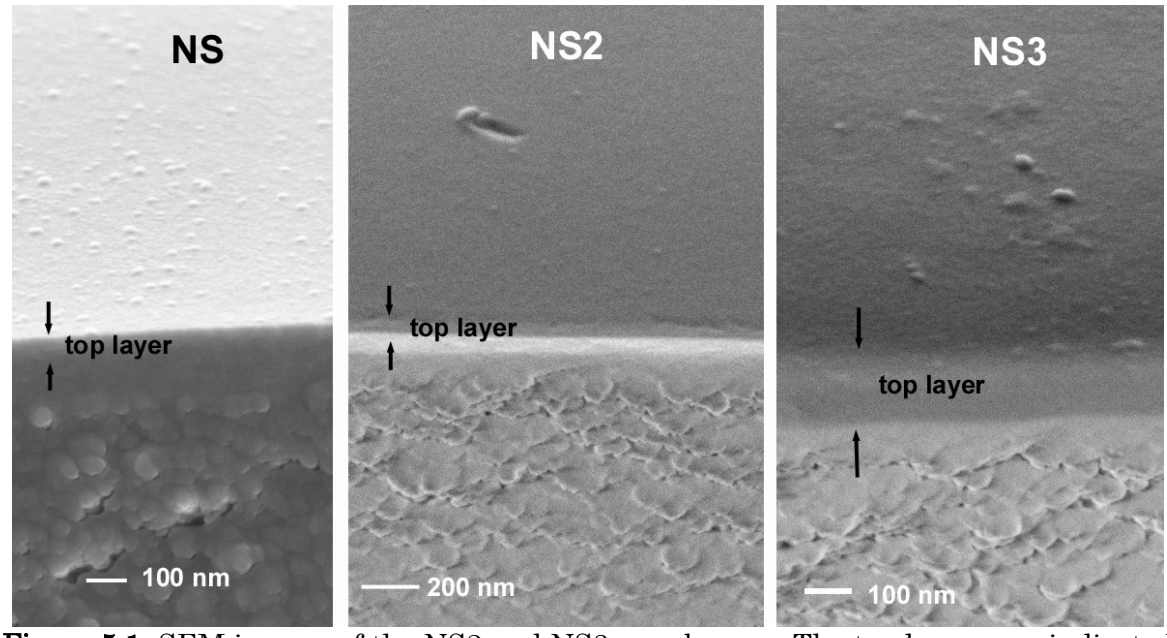

Figure 5.1. SEM images of the NS2 and NS3 membranes. The top layers are indicated by the arrows.

After coating of these sols and calcination at 500 °C, selective separation layers

with differing thicknesses were obtained, as illustrated in Figure 5.1. The Nb-doped silica top-layer of the NS membrane was 150 nm thick, as previously reported. The top layers of NS2 and NS3 had thicknesses of 60 and 100 nm, respectively.

Table 5.2. Permeance, permeability (permeance normalized per unit of membrane thickness) and ideal permselectivity of the NS*s* membrane. The data refer to measurements conducted at 200 °C, ΔP = 4 bar.

	Permeance* [mol·Pa^{-1}·m^{-2}·s^{-1}]		Ideal selectivity	Ideal selectivity	Top-layer thickness	Permeability§ [mol·Pa^{-1}·m^{-1}·s^{-1}]	
	He	H_2	He/H_2	He/CO_2	[nm]	He	H_2
NS	$7.2\cdot10^{-8}$	$3.8\cdot10^{-8}$	1.9	43	150	$1.2\cdot10^{-14}$	$5.7\cdot10^{-15}$
NS2	$1.2\cdot10^{-8}$	$4.5\cdot10^{-9}$	2.7	37	60	$7.3\cdot10^{-16}$	$2.7\cdot10^{-16}$
NS3	$2.8\cdot10^{-8}$	$3.7\cdot10^{-9}$	7.6	70	100	$2.9\cdot10^{-15}$	$3.7\cdot10^{-16}$

*These values were not corrected for support resistance
§ After correction for support resistance, layer permeance was multiplied by top layer thickness as measured by SEM analysis.

Table 5.2 reports the hydrogen and helium permeances of the three membranes. The permeance of the NS membranes to different gases has already been reported in detail in Chapter 3. In the case of NS2, the helium permeance was $1.2\cdot10^{-8}$ mol·Pa^{-1}·m^{-2}·s^{-1} and the hydrogen permeance was $4.5\cdot10^{-9}$ mol·Pa^{-1}·m^{-2}·s^{-1}. On the other hand, the NS3 membrane had a higher permeance of $2.8\cdot10^{-8}$ mol·Pa^{-1}·m^{-2}·s^{-1} for helium, but a lower permeance of $3.7\cdot10^{-9}$ mol·Pa^{-1}·m^{-2}·s^{-1} for hydrogen.

The capacity of the materials that constitute the gas-selective top layer can be compared directly by correcting the overall permeance of the membrane for the support resistance and the thickness of the top layer. This numerical correction allowed calculation of the permeability of the top layer, which is defined as the permeance per unit of membrane thickness. The method that was used to subtract the support resistance from the overall permeance is described on page 47. The calculated permeabilities of the Nb-doped silica layers for helium and hydrogen are listed in Table 5.2. The material forming the NS top layer is more permeable to these small gas molecules than the other two.

Comparison of NS with NS2 shows that the hydrogen permeability decreased from $5.7 \cdot 10^{-15}$ to $2.7 \cdot 10^{-16}$ mol·Pa^{-1}·m^{-1}·s^{-1}, while the helium permeability decreased from $1.2 \cdot 10^{-14}$ to $7.3 \cdot 10^{-15}$ mol·Pa^{-1}·m^{-1}·s^{-1}. NS2 and NS were prepared from sols with the same molar composition, but with different reaction times. The two membranes were coated on similar supports and calcined at the same temperature. Thus, the large difference in permeability is somehow related to the evolution of the structure of the coating sols during synthesis. XPS analysis of the NS membrane, as reported on page 43, suggested that unreacted TEOS molecules or silica oligomers were still present even in the NS sol. When these small particles or prepolymeric structures become trapped in the top layer during film formation, a relatively dense material results after consolidation and calcination. The NS2 sol was less developed than the NS sol, because its reaction time was lower. So, it is reasonable to assume that the concentration of these unreacted species was particularly high in the NS2 sol. Consequently, the resistivity of this layer after calcination was higher than that of the NS layer. The data reported in Table 5.1 support this explanation. An R_g equal to 2.4±0.1 nm was measured for NS2. This radius is smaller than that of the other two sols and it is also relatively small compared to the pore size of the underlying γ-alumina layer, which has pore radii of 2.5-4 nm. The SEM picture in Figure 5.1 shows that the niobia-silica sol penetrated in the support down to a depth of about 50 nm or more. Due to the penetration of Nb/Si mixed oxide into the support, the thickness of the NS2 top layer in Table 5.2 may be underestimated, and also its permeability. Such substantial penetration of the niobia-silica phase into the support also provides an explanation for the low helium permeance of the NS2 membrane.

The same explanation does not hold for the low He and H_2 permeances measured on the NS3 membrane. Indeed, the NS3 sol has a particle size that is similar to the NS sol, but its Nb : Si molar ratio is higher than that of NS and NS2. The NS3 sol was synthesized with a Nb : Si ratio equal to 0.8. Since to be neutral Si ions need to establish 4 bonds with oxygen atoms and Nb 5, the number of Nb-O bonds in the amorphous consolidated state is equal to the

number of Si-O bonds. The higher resistance of the NS3 layer to hydrogen and helium flow is most likely related to the higher concentration of Nb in NS3. The Nb^{5+} ions in the network have a coordination number equal to 6 [7], while Si^{4+} has a coordination number of 4 [8]. The presence of the more highly charged Nb ions, and the ability and tendency of Nb to coordinate more oxygen ions may lead to a more closely packed and denser network. The effect is most pronounced in NS3, since the concentration of Nb ions is higher than in the other samples.

All the samples were non-crystalline in XRD analysis. Even at a Nb : Si molar ratio of 0.8 the material appears to be non-crystalline. Hence, the densification of the network due to the introduction of Nb ions does not lead to an increase of crystallinity, at least to an extent that is detectable by XRD.

The higher concentration of Nb in NS3 also has other consequences. The ideal separation factor of a mixture containing He and H_2 is 7.6 for the NS3 membrane, as listed in Table 5.2. The ideal separation factor He/H_2 measured for NS and NS2 were 1.9 and 2.7, respectively. The separation factor He/CO_2 is also higher for the NS3 membrane than for the other samples. Generally speaking, microporous membranes are more permeable to helium than to other gases, because helium is very small and hardly interacts with the pore walls due to its noble character. However, this tendency seems to be more pronounced in the NS3 membrane than in the other two. This may possibly be attributed to a predominance of pores in the NS3 membrane that are accessible to helium only.

Table 5.3. Apparent activation energies of H_2, He and CO_2 permeance through Nb-doped silica membranes, as calculated by fitting the data in Figure 5.2 to Equation 3.3.

	He apparent E_a [kJ·mol^{-1}]	H_2 apparent E_a [kJ·mol^{-1}]	CO_2 apparent E_a [kJ·mol^{-1}]
NS	19.1±0.3	15.3±0.7	-14.2±0.8
NS2	18.1±1.2	16.3±1.0	-
NS3	22.0±0.9	15.0±1.2	-

In Figure 5.2 the temperature dependencies of the He, H_2 and CO_2 permeances of all three membranes are shown. The calculated apparent activation energies are listed in Table 5.3. The

apparent activation energy of hydrogen permeance is similar for all three samples, and is about 15-16 kJ·mol^{-1}. The activation energy of He permeance in the NS3 membrane is 22.0±0.9 kJ·mol^{-1}. It has a slightly higher value than measured on the other two samples with 18-19 kJ·mol^{-1}. These differences are in agreement with the single gas permeation data of Table 5.2, which showed a preferential permeability towards helium at 200 °C, especially for the NS3 sample.

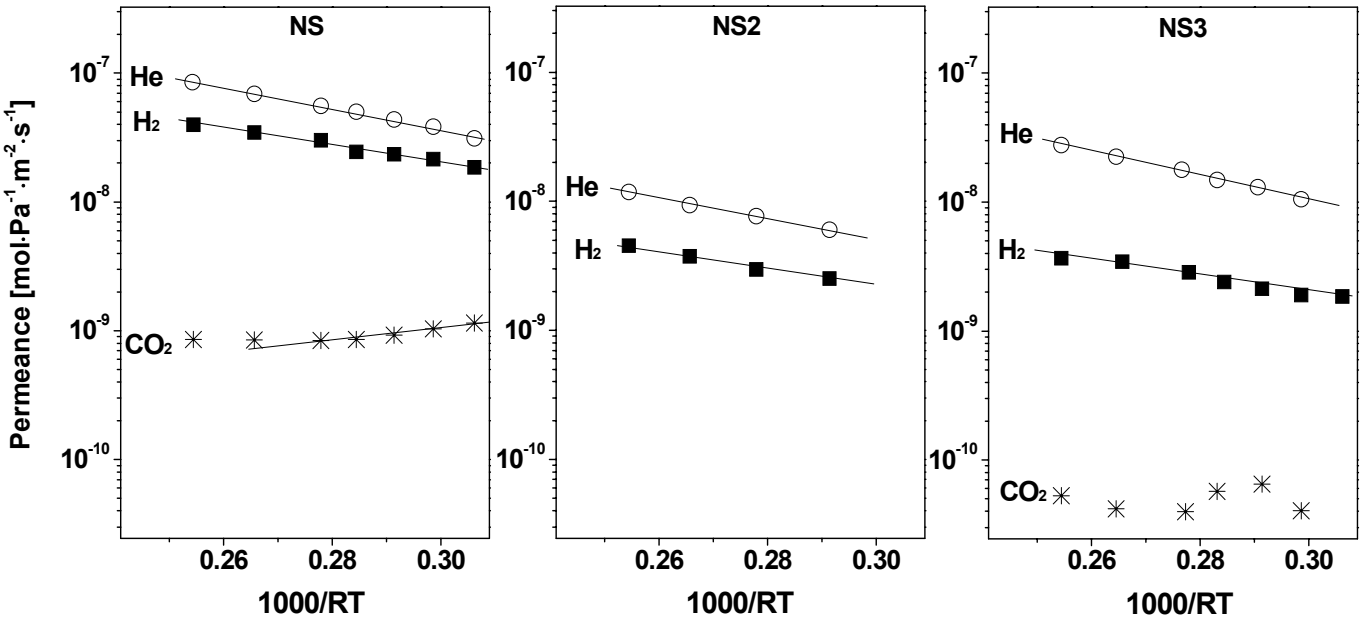

Figure 5.2. Temperature dependency of He, H_2 and CO_2 permeance in NS, NS2 and NS3. The data were corrected for support resistance and plotted in the form of Arrhenius plots.

A tubular membrane was prepared by coating the NS sol on the outer part of an alumina support as described in the experimental part. The hydrogen permeability of the tubular support that was used for deposition of the NSt membrane was about 10 times higher (10^{-5} mol·Pa^{-1}·m^{-2}·s^{-1}) than that of the disk membranes (10^{-6} mol·Pa^{-1}·m^{-2}·s^{-1}). The α-alumina disks have pores with diameters of 80-120 nm, while the tube used for the preparation of the NSt membrane had a more complex profile designed to minimize the resistance to the gas flow. Pictures of the membrane are shown in Figure 5.3.

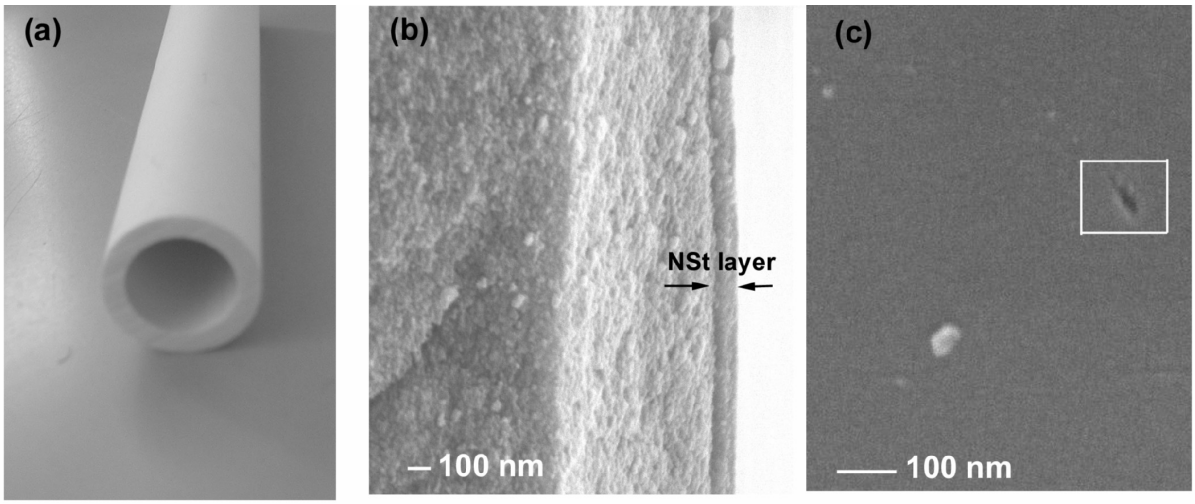

Figure 5.3. Picture and SEM magnifications of the NSt membrane. The tubular membrane (a). Membrane cross-section (b). Membrane surface (c), the white square emphasizes a defect.

From the SEM picture of the cross-section it is possible to estimate the thickness of the gas selective top layer. Although the sol used for the NS coating was about 6.25 times more concentrated than that used for the preparation of the NS disk membranes, the microporous top layers had similar thicknesses, i.e. about 150 nm. The tubular membrane showed fluxes that are at least one order of magnitude larger than those of the disk membranes. Values are reported in Table 5.4. For instance, the NSt membrane had a calculated hydrogen permeance of $1.0 \cdot 10^{-6}$ mol·Pa^{-1}·m^{-2}·s^{-1}, while the NS membrane had a hydrogen permeance of $3.9 \cdot 10^{-8}$ mol·Pa^{-1}·m^{-2}·s^{-1}. This huge difference may be partly due to the influence of the support. The two types of top layers probably also have different penetration depths in the support. However, the main reason for the high fluxes registered for the NSt membrane is the presence of defects in the gas selective top layer. One of these defects is shown in Figure 5.3c. Coating tubular membrane is more complicated than the coating of small flat disks. The presence of defects is reflected in the low values of H_2/x and He/x ideal selectivity listed in Table 5.4, where x represents the second component of a hypothetical binary mixture with helium. It can be either H_2, CO_2, N_2 or CH_4. The He/N_2 and He/CH_4 ideal permselectivities of the NSt membrane are higher than the selectivity of a membrane in which pure Knudsen transport occurs, as can be calculated by using Equation 2.10 on page

32. The same observation can be made for the ideal permselectivity of the NSt membrane for the binary mixtures H_2/N_2 and H_2/CH_4. Further development of the coating sol will be necessary to enable preparation of tubular membranes with a reduced number of defects.

	He	H_2	CO_2	N_2	CH_4
Permeances [$mol \cdot Pa^{-1} \cdot m^{-2} \cdot s^{-1}$]	$1.0 \cdot 10^{-6}$	$1.0 \cdot 10^{-6}$	$3.9 \cdot 10^{-7}$	$1.8 \cdot 10^{-7}$	$2.3 \cdot 10^{-7}$
Ideal selectivity H_2/x	1.0	-	2.6	5.4	4.3

Table 5.4. Permeances and ideal selectivities of He, H_2, CO_2, N_2 and CH_4 trough the NSt membrane measured at 200 °C with a overpressure across the membrane of 1 bar. The data are not corrected for support resistance.

A key property of a porous membrane is its pore size distribution. The pore size distribution of a membrane can be measured directly by permporometry or indirectly by BET analysis on unsupported material. As was noted in Chapter 3, the calcination of the NS sol at 500 °C yielded a black powder that was dense in BET analysis. Another disadvantage of BET analysis is that it is performed on powders that may have pore size distributions that are different from those of the corresponding thin films, as in this case. The pore size distribution of membranes is therefore often assessed by permporometry analysis. The principles of permporometry analysis have been discussed in Chapter 2, on page 29. The relatively high resistance of the NS layer and the fact that the membranes have an effective surface area of only $1.9 \cdot 10^{-4}$ m^2 implies very low gas fluxes. This is the reason that it was not possible to measure the permporometry profile of the NS membrane with sufficient precision.

Permporometry could however be used to investigate the pore size distribution of the NSt layer. In this case, the measured membrane area was $3.7 \cdot 10^{-3}$ m^2. The limitations and problems associated with application of this technique to microporous layers will be discussed in the next chapter. The pore size distribution of the NSt top-layer was calculated by using Equation 5.1 [9],

which is directly derived from the Knudsen [10] and Kelvin [11] equations:

$$n(r_k) = -\frac{K_{memb}}{r_k^3}\sqrt{\frac{RTM}{2\pi}}\left(\frac{\Delta F_{acc}}{\Delta r}\right). \quad (5.1)$$

In Equation 5.1 n represents the number of pores in the membrane, K_{memb} is a constant depending on the pore shape, membrane surface area and thickness of the top layer, R is the ideal gas constant, T is the absolute temperature, and M is the helium molecular mass. r_k is the radius corresponding to a certain relative pressure of water vapor as calculated from the Kelvin equation. The last term of the equation is the derivative of permeance over r_k.

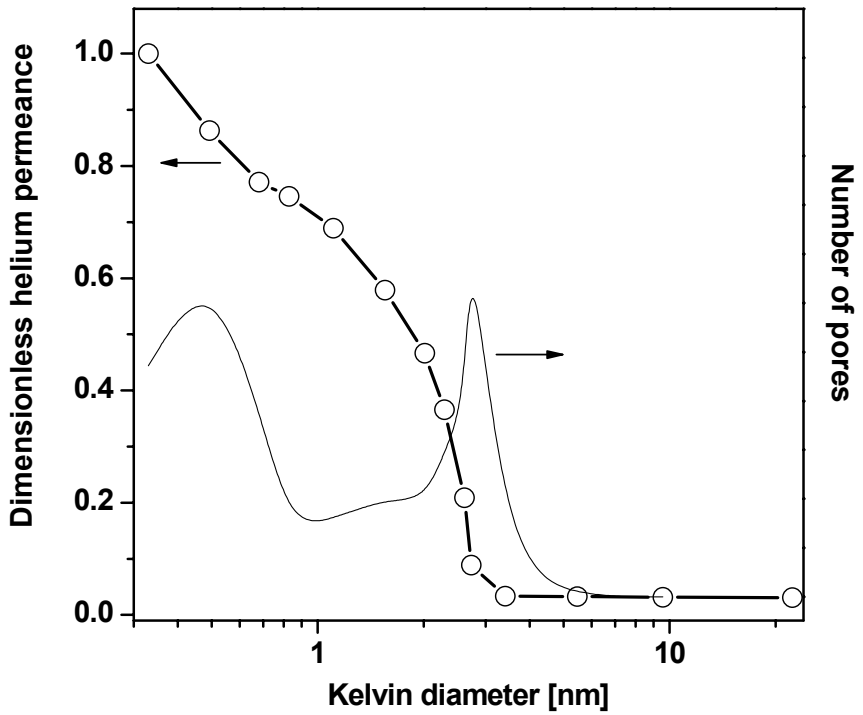

Figure 5.4. Permporometry analysis of the NSt membrane. Helium permeance (thick line) and pore size distribution (thin line) were plotted as function of the Kelvin diameter calculated by Equation 5.1.

The permporometry plot of NSt is depicted in Figure 5.4. The helium permeance and pore size distribution of NSt are reported as a function of Kelvin diameter ($D_k = 2r_k$). The pore size distribution shows two distinct peaks.

One peak is centered at a D_K value of about 3 nm. The presence of this signal is probably due to the presence of mesopores and/or small defects. It mainly corresponds to the pore diameters of the γ-alumina layer underneath. A second peak is present in the ultramicropore region between 0.3 nm and 1 nm. The presence of micropores larger than 0.55 nm in these layers had already been demonstrated by SF_6 single gas permeation experiments on the NS membrane. Since the NS layer was found to be permeable to SF_6, it has a fraction of pores larger than the kinetic diameter of SF_6, i.e., 0.55 nm.

5.4. Conclusions

In the fabrication of microporous ceramic membrane, it is necessary to limit the dimension of the sol particles to the nanometer size, in order to fabricate microporous layer with thickness of few tens of nanometers. This is commonly achieved by strictly controlling the quantity of water and acid in the system. However, the comparison between NS and NS2 showed that poorly developed sols are also not optimal to coat microporous membranes on porous supports. Indeed, the lower permeability of the NS2 layer compared to NS was probably to due to the fact that the NS2 sol was prepared in a shorter reaction time than the NS sol. Thus, its structure was less developed. This consideration can probably be generalized to all sols used for membrane coatings.

The helium and hydrogen permeabilities of the final NS-type layer also depend on the Nb loading in the material. Indeed, comparison between NS and NS3 suggested that the helium permeability of the material decreased with increasing Nb loading. Thus, the Nb : Si molar ratio should be an optimized, taking in account both the requirement of high selectivity and the highest possible permeability.

The permeability of the NS*s* layers may also be increased via the so-called templating method [12]. In principle, microporous NS*s* can be prepared by using small templating molecules [13], such as hexyl trimethyl ammonium bromide, or cetyl trimethyl ammonium bromide (CTAB). This has already been

demonstrated by Sah et al. for organic-inorganic hybrid membranes [14].

The reported data suggest an intriguing perspective, namely to fabricate mesoporous templated NS-type membranes by using CTAB micelles or similar assemblies as template. Such membranes should be highly permeable to gas molecules. The methods described in Chapters 7 and 9 could eventually be used in the fabrication of these membranes. Any deviation of the x/CO_2 ideal separation factor from the one predicted by Equation 2.10 (page 32) in NS*s* mesoporous membranes could provide further information about the interaction between CO_2 and the pore surface of the NS*s* materials.

5.5. References

[1] C.J. Brinker; G.W. Scherer, Sol-gel Science, Harcourt Brace Jovanovich, Boston, 1990, p. 779.

[2] C. J. Brinker, T.L. Ward, R. Sehgal, N.K. Raman, S.L. Hietala, D.M. Smith, D.-W. Hua, T.J. Headley, J. Membrane Sci., 77 (1993) 165.

[3] J. Sekulic, J.E. ten Elshof, D.H.A Blank, Adv. Mater., 16 (2004) 1546.

[4] A. Nijmeijer, H. Kruidhof, R. Bredesen, H. Verweij, J. Am. Ceram Soc. 2001, 84, 136.

[5] A.J. Burggraaf; "Fundamentals of inorganic membrane science and technology", Elsevier, Amsterdam, 1996.

[6] J. Campaniello C.W.R. Engelen, W.G. Haije, P.P.A.C. Pex, J.F. Vente Chem. Comm. 7 (2004) 834.

[7] J.H. Jehng, I.E. Wachs, Catalysis Today, 8 (1990) 37.

[8] R.K. Iler, The chemistry of silica: solubility, polymerization, colloid and surface properties, and biochemistry, New York, Wiley.

[9] V. Boffa, J.E. ten Elshof, D.H.A. Blank, Mesoporous Microporous Mat. 100 (2007) 173

[10] R.R. Bhave, "Inorganic Membranes: Synthesis, Characteristics and Applications", Van Nostrand Reinhold, New York, 1991, p. 338.

[11] D.D. Do, Adsorption Analysis: Equilibria and Kinetics, vol 1, Imperial

College Press, London, 1998, p.115.

[12] C.T. Kresge, M.E. Leonowicz, W.J. Roth, J.C. Vartulli, J.S. Beck, Nature 359 (1992) 710.

[13] C-Y Tsai, S-Y Tam, Y Lu, C. J. Brinker, J. Membr. Sci. 169 (2000) 255

[14] A. Sah, H.L. Castricum, J. Vente, D.H.A. Blank, and J.E. ten Elshof, Microporous molecular separation membrane with high hydrothermal stability European Patent application EP 06100388.5, 2006.

CHAPTER 6

Hydrothermal stability of microporous niobia-silica membranes

Abstract:

The hydrothermal stability of the NS membrane was investigated and compared with the stability of a pure silica membrane. The membranes were exposed at 150 and 200 °C for 70 h at a steam partial pressure of 0.56 bar Single-gas permeation measurements were used to probe the change of the pore structure of a membrane after exposure to steam. After subtracting the support resistance to the hydrogen and helium permeance values it was possible to observe the higher hydrothermal stability of the NS layer than in the pore silica film. Indeed after the second treatment in the silica membrane the helium permeance was reduced to 21% of its initial value, and hydrogen permeance to 27% after the first treatment. In the case of NS, the decrease of permeance was less pronounced. After the treatment at 200 °C, the hydrogen permeance was the 72% of that of the untreated sample, while the helium permeance the 47%. The apparent activation energy of the He permeance was 12.8±0.3 kJ·mol^{-1} for the pure silica membrane and 19.3±0.6 kJ·mol^{-1} for the NS sample. The H_2 permeance activation energy was found to be 12.2±0.2 kJ·mol^{-1}for silica and 15.3±0.7 kJ·mol^{-1} for NS. The hydrothermal treatment left the activation energies unchanged in both samples. The structural change of the microporous pure silica layer was observed also by nanopermporometry. The data acquired with this technique were comparable to those obtain with single gas permeation experiments, upon subtraction of about 0.2 nm to the calculated pore size distribution. The data here presented suggest that, during the small time of steam exposure densification occurred only in the point of higher convex curvature increasing the effective path of helium and hydrogen across the membranes, without changing the apparent activation energies of their permeances.

6.1. Introduction

Because of its high retention of CO_2, the NS membrane could be applied in membrane reactors to recover H_2 from hydrogen synthesis processes such as steam reforming [1] and water gas shift [2]. In these processes hydrocarbons or CO are oxidized by steam to yield CO_2 and hydrogen.

Ceramic membranes need to be stable under working conditions for at least a few years in order to be commercially feasible. The major factor that is limiting the long term durability of microporous ceramic membranes is their relatively low stability at high temperatures in the presence of steam. The porous structure collapses during hydrothermal exposure, yielding a denser material.

The microporous silica network can be stabilized by introducing transition metals into the silica network. Oxygen forms more polar and stable bonds with these metals than with silicon. Furthermore, most transition metals have coordination numbers larger than silicon, which has a coordination number equal to 4 [3]. Thus, they have a tendency to form a more closely packed and crystalline structure than pure silica. For this reason NS membranes are expected to be more stable than pure microporous silica ones.

In this chapter the stability of the NS membrane is investigated and compared with that of silica membranes. Nanopermporometry and single-gas permeation measurements were employed to probe the change of the pore structure of the membranes after exposure to steam. The hydrothermal treatment consisted of exposure of the membranes to 150 and 200 °C for 70 h at a steam partial pressure of 0.56 bar.

6.2. Experimental part

Preparation of the NS membrane

The NS membrane was prepared as described on page 40.

Synthesis of the silica sol

Silica sols were prepared by adding 11 ml of 0.73 N aqueous nitric acid to

21 ml of tetraethylorthosilicate (TEOS, 98 %, Aldrich) dissolved in 21 ml ethanol (≥ 99.5%, Aldrich). The addition was carried out drop by drop under vigorous stirring, while the reaction flask was cooled in an ice bath. The mixture was then refluxed at 60 °C for 3 h. The so prepared silica sol was diluted 18 times in ethanol and kept at -5 °C for few days until it was used for preparation of membranes.

Preparation of the silica membranes

The silica membrane was prepared by dipping a flat support in the diluted sols at an angular speed of 0.06 rad·s^{-1}. The support was of the same type as used for the preparation of NS membranes. The membrane was calcined in air at 500 °C for 3 h, with a heating/cooling rate of 0.5 °C/min. These conditions are the same as used for the NS membrane. The silica sol was highly diluted an extremely thin layer was formed. For this reason, the coating and calcination cycle was repeated to cover all remaining parts of the membrane surface where no material may have been deposited in the first coating step.

Single-gas permeation experiments

The permeances of different gases in silica and NS membranes were determined by using the setup shown in Figure 6.1. In single gas permeation experiments valves were closed with the exception of valve number 2, and the setup was used as a dead-end mode permeation setup [4]. In a typical single-gas permeation experiment, the membrane was first degassed at 200 °C for two days in a flowing helium atmosphere. Then the fluxes of He, H_2, CO_2, N_2, CH_4 and SF_6 were measured individually, employing a pressure of 5 bar on the side of the feed, and atmospheric pressure on the permeate side. The gas flow on the permeate side was controlled with a soap film flow meter, which allowed measurement of volumetric gas flows with high accuracy in a wide range of flows. The permeation rates of different gases were determined in a sequence with increasing kinetic diameter, and equilibrating for at least 3 h each time a new gas was introduced into the setup. In the case of hydrogen

and helium the gas permeation measurements were done in a range of temperatures between 90 and 200 °C, in order to determine the apparent activation energies of permeance of these gases in the microporous layers.

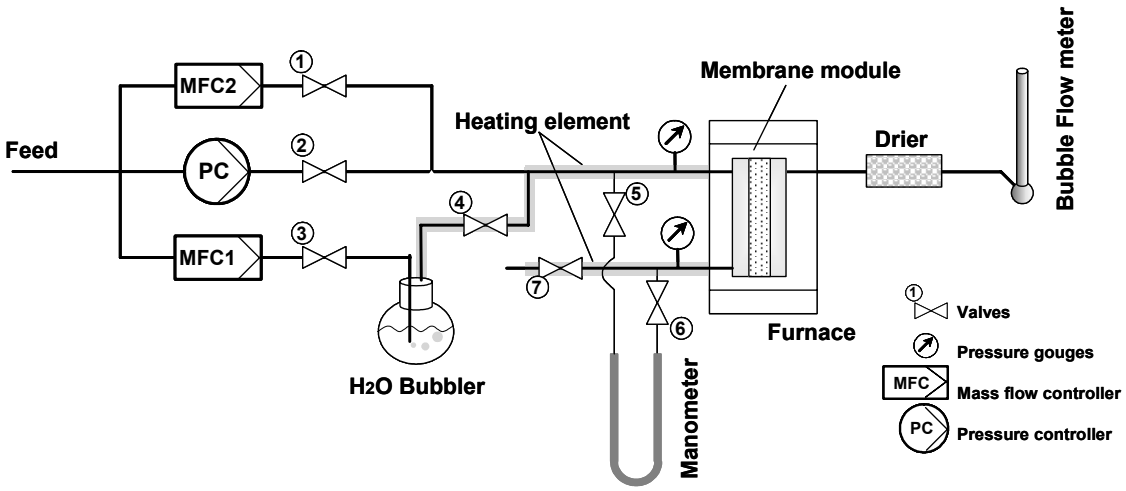

Figure 6.1. Schematic diagram of the experimental set-up. The operation of this set-up is described in the text.

Nanopermporometry measurements

In the second stage of characterization, the pressure controller was excluded from the active part of the setup by closing valve number 2, and opening the other valves. Valve 7 was regulated manually to produce an overpressure of 1.0 kPa on the feed side. While flushing the membrane with dry hydrogen the sample temperature was decreased from 200 °C to 90 °C. The temperature of the water bath was kept at 32 °C. The steam partial pressure in the feed was gradually raised by varying the gas flow trough the two mass flow controllers MFC1 and MFC2 (Figure 6.1). During this operation, the H_2 pressure gradient across the membrane was kept fixed at 1 kPa.

Hydrothermal treatment

The hydrothermal stability of the silica and the NS membranes was tested by exposure to steam at two different temperatures. Membranes were first exposed to a steam partial pressure of 0.56 bar at 150 °C for 70 h, with hydrogen being used as sweep gas. The total overpressure at the feed side was

4 bar. Then the sample was dried at 200 °C for 2 days. After that, single gas measurements were done at 200 °C, starting from helium to SF_6. The pore size distribution of the silica top layer was measured by nanopermporometry, under the same experimental conditions as used for the fresh sample. After exposure to 0.56 bar of steam at 200 °C for 70 h, the gas permeation and nanopermporometry experiments were repeated a third time.

Scanning Electron Microscopy

Scanning Electron Microscopy (SEM) images were taken on a LEO 1550 FEG.

6.3. Results and discussion

Morphology and stability

The SEM images in Figure 2 show the cross-section of the silica and the NS membrane. The gas-selective thin layers have a thickness of about 30 nm and 150 nm in the silica and NS membrane, respectively. Silica and NS-derived powders were x-ray amorphous after calcination at 500 °C.

The results of single gas permeation experiments on these two membranes are listed in Table 6.1 and Table 6.2.

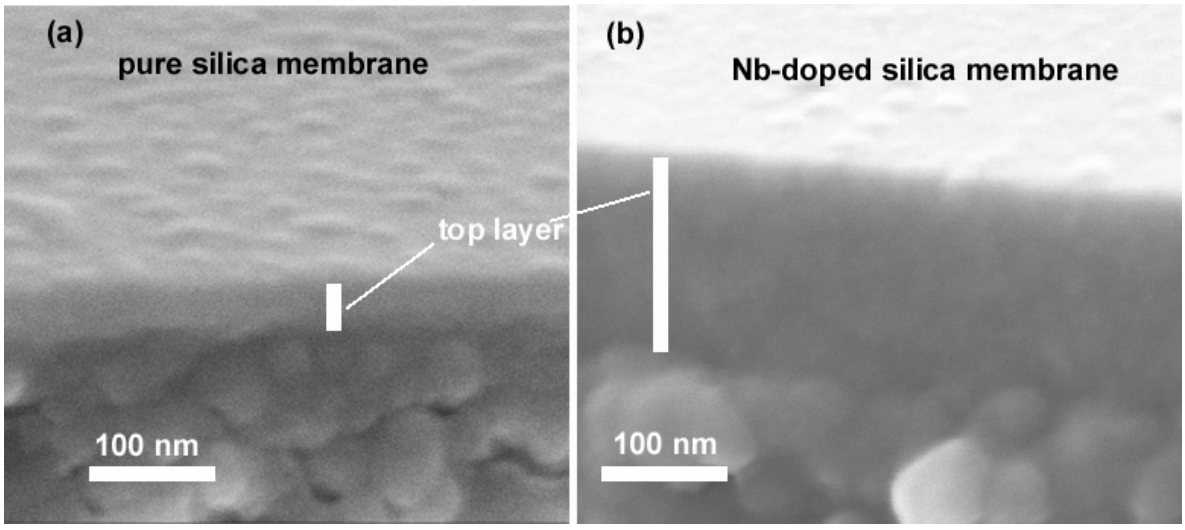

Figure 2. SEM images of cross sections of the pure silica microporous top-layer (a) and of the NS gas selective layer (b).

Table 6.1. Single-gas permeance of silica membrane before and after the first (HT150) and second (HT200) hydrothermal treatment.# The ideal hydrogen to X permselectivity is reported for every set of measurements.

molecule	d_k [12] [nm]	Fresh sample		After HT150		After HT200	
		F^*	$F_{H2/X}$	F^*	$F_{H2/X}$	F^*	$F_{H2/X}$
He	0.26	$6.1 \cdot 10^{-7}$	1.0	$3.7 \cdot 10^{-7}$	0.85	$3.7 \cdot 10^{-7}$	0.75
H_2	0.29	$6.3 \cdot 10^{-7}$	1	$3.1 \cdot 10^{-7}$	1	$3.0 \cdot 10^{-7}$	1
CO_2	0.33	$1.3 \cdot 10^{-8}$	46	$9.5 \cdot 10^{-9}$	33	$6.3 \cdot 10^{-9}$	47
N_2	0.36	$4.2 \cdot 10^{-9}$	$1.5 \cdot 10^{2}$	$2.2 \cdot 10^{-9}$	$1.4 \cdot 10^{2}$	$2.1 \cdot 10^{-9}$	$1.4 \cdot 10^{2}$
CH_4	0.38	$1.1 \cdot 10^{-9}$	$5.6 \cdot 10^{2}$	$1.5 \cdot 10^{-9}$	$2.0 \cdot 10^{2}$	$1.1 \cdot 10^{-9}$	$2.7 \cdot 10^{2}$
SF_6	0.55	$\leq 1 \cdot 10^{-10}$	$\geq 10^{3}$	$\leq 1 \cdot 10^{-10}$	$\geq 10^{3}$	$\leq 1 \cdot 10^{-10}$	$\geq 10^{3}$

Table 6.2. Single-gas permeances of NS membrane before and after the first (HT150) and second (HT200) hydrothermal treatment.# The ideal hydrogen to X permselectivity is reported for every set of measurements.

molecule	d_k [12] [nm]	Fresh sample		After HT150		After HT200	
		F^*	$F_{H2/X}$	F^*	$F_{H2/X}$	F^*	$F_{H2/X}$
He	0.26	$7.2 \cdot 10^{-8}$	0.54	$5.2 \cdot 10^{-8}$	0.71	$4.0 \cdot 10^{-8}$	0.68
H_2	0.29	$3.9 \cdot 10^{-8}$	1	$3.7 \cdot 10^{-8}$	1	$2.7 \cdot 10^{-8}$	1
CO_2	0.33	$8.5 \cdot 10^{-10}$	46	$8.2 \cdot 10^{-10}$	45	$8.3 \cdot 10^{-10}$	33
N_2	0.36	$6.2 \cdot 10^{-9}$	6.3	$6.2 \cdot 10^{-9}$	6.0	$6.7 \cdot 10^{-9}$	4.0
CH_4	0.38	$5.4 \cdot 10^{-9}$	7.2	$5.8 \cdot 10^{-9}$	6.4	$5.4 \cdot 10^{-9}$	5.0
SF_6	0.55	$2.9 \cdot 10^{-9}$	13	$2.9 \cdot 10^{-9}$	13	$3.0 \cdot 10^{-9}$	9.0

The data here reported were not corrected for the resistance of the support.
* Permeance (F) is expressed in $mol \cdot s^{-1} \cdot m^{-2} \cdot Pa^{-1}$.

These data allow estimation of the pore size distributions. Assuming that the membrane behaves as a size-based sieve, a low permeance for a certain species corresponds to a small number of pores that is accessible for that species. Single gas permeation measurements were performed at 200 °C with 6 gases. The kinetic diameters of the probe molecules used in this experiment are listed in the second left columns of Table 6.1 and 6.2. In general, a gradual decrease of membrane permeance was observed when the kinetic diameter of the probes increased. Except for the couple hydrogen/helium, the permeance of the fresh silica membranes decreased with increasing kinetic diameter, as shown in Table 6.1. The helium atom has a kinetic diameter smaller than the hydrogen molecule. The fact that the permeance of helium at 200 °C is lower than the permeance of hydrogen can be explained by considering the contribution of Knudsen transport in the pores of the support to the total transport. Helium (M=4 g/mol) has twice the mass of hydrogen (M=2 g/mol). Thus, in the Knudsen regime the permeance of the membrane for hydrogen is higher than for helium, as shown in Equation 3.1 on page 38 [5].

The permeance of the silica membrane to sulfur hexafluoride was so low that it was not possible to measure it. From the data in Table 6.1, we can conclude that the majority of pores in the silica gas-selective top layer have a diameter between 0.3 and 0.4 nm, and a negligible number of pores have a diameter larger than 0.55 nm.

In Table 6.2 the permeation data of the niobia-silica membrane are listed. The helium permeance of the fresh NS membrane was almost twelve times larger than that of nitrogen. This suggests that a large fraction of pores has dimensions smaller than the size of nitrogen (0.36 nm). However, in contrast to the silica membrane, the NS membrane was also somewhat permeable to SF_6 (kinetic diameter 0.55 nm). This suggests the presence of a fraction of pores (or defects) larger than ~0.55 nm. As was already noted, the NS membrane exhibits a moderate sieving capacity for apolar gases, and a high retention towards CO_2. This suggests that the larger pores through which SF_6 diffused are most likely in the microporous size range, because the presence of

mesoporous or larger defects would have to result in much lower retentions of CO_2.

The single gas permeances after each hydrothermal treatment are also listed in Table 6.1 and Table 6.2, where the abbreviations HT150 and HT200 are used to indicate the data acquired after the first and second hydrothermal treatment, respectively. H150 and HT200 were done at a steam partial pressure of 0.56 bar. The net effect of exposure to steam is densification of the microporous material, which results in a reduced permeance of the membrane to hydrogen and helium. Table 6.1 shows that the densification of the pure silica membrane was significant after the first treatment at 150 °C, and less pronounced after hydrothermal exposure at 200 °C. After HT150, the permeance of larger molecules did not increase, and it neither did so after HT200. This does not suggest the presence of cracks, because it has already been mentioned in Chapter 1 that the formation of microcracks as a result of hydrothermal degradation is an unpredictable event, which may occur after many days of exposure to steam. In this respect, it is also relevant to note that the H_2/He permselectivity became smaller than 1 after HT150, while it was larger than unity for fresh membranes. This change can be explained by considering that hydrogen, being the lighter molecule, has a higher Knudsen translation rate than helium. If the relative contribution of Knudsen transport to the total flux decreases upon densification and pore shrinkage resulting from hydrothermal exposure, then this strongly suggests the closing of larger pores. We can therefore conclude that, during the relatively brief period of hydrothermal treatment, i.e., two times 70 h, the porous structure of silica became denser, but no cracks or defects were formed.

The He permeance of the niobia-silica membrane decreased from $7.2 \cdot 10^{-8}$ to $5.2 \cdot 10^{-8}$ mol·(Pa·m^2·s)$^{-1}$ after HT1 and to $4.0 \cdot 10^{-8}$ mol·(Pa·m^2·s)$^{-1}$ after HT2, as reported in Table 6.2. The decrease of hydrogen permeance was less pronounced than that of helium after HT2. The permeance of the other molecules with a larger kinetic diameter remained almost unaffected by steam exposure. The decrease of ideal selectivity of the membrane towards mixtures

containing hydrogen and other gases can thus be attributed to the decline of hydrogen permeance upon exposure to steam.

To compare the hydrothermal stability of the two materials it is necessary to determine the actual permeance of the gas-selective layer in each membrane. This can be done by considering the membrane as a series of layers, each having a certain resistance to the gas flow. By definition, the resistance of each layer is the reciprocal of the permeance. The permeance of the gas selective layer can thus be determined from the total permeance and the permeance of the support via [4]:

$$(6.1)\ \frac{1}{F_{tot}} = \frac{1}{F_{top}} + \frac{1}{F_{Sup}},$$

where F_{tot} is the total permeance and F_{top} and F_{sup} are the permeances of the top layer and the support, respectively. The permeance of the support to different probes at diverse temperatures has been reported in Chapter 3.

By applying Equation 6.1, a hydrogen permeance of $1.6 \cdot 10^{-6}$ mol·(Pa·m^2·s)$^{-1}$ for the silica membrane and of $3.8 \cdot 10^{-8}$ mol·(Pa·m^2·s)$^{-1}$ for the NS membrane at 200 °C were calculated. This implies that the hydrogen permeabilities, at this temperature were $4.5 \cdot 10^{-14}$ mol·(Pa·m·s)$^{-1}$ for silica and $5.7 \cdot 10^{-15}$ mol·(Pa·m·s)$^{-1}$ for NS. Here permeability id defined as permeance per unit membrane thickness. The relatively low permeability of NS is probably reated to the fact that the niobia-silica sol was synthesized at lower hydrolysis and acid ratios than the silica sol. Therefore, the incorporation of unreacted precursor molecules or small silica clusters into the NS layer may have resulted in a relatively dense material after consolidation and calcination.

The fact that the permeability of NS is lower than the permeability of silica can also be due to the incorporation of the Nb ions in the microporous network. For instance, in the previous chapter the permeability of NS3 was found to be lower than that of NS. NS3 was obtained from a sol with a nominal Si : Nb atomic ratio of 1.25, while the nominal atomic ratio Si:Nb in NS was 3. This suggests a trend according to which the permeability decreases with increasing Nb concentration in the network.

The hydrothermal stability of silica and NS are compared in Figure 6.3. The influence of HT150 and HT200 on the permeances of both types of top layers are shown. Hydrothermal densification is most prominent for silica. The helium permeance was reduced to 21% of its initial value, and the hydrogen permeance to 27%, after only 70 h of exposure to 0.56 bar steam at 150 °C. After HT200, no further significant decrease of helium and hydrogen permeance was measured. In the case of niobia-silica, the decrease of permeance was less pronounced. After HT150, the hydrogen permeance was reduced by about 5%, while the helium permeance was reduced by 32%. This suggests that only a small fraction of ultramicropores of NS underwent densification upon hydrothermal treatment, namely those pores that were small enough to be accessible to He but not to H_2. Further hydrothermal treatment at 200 °C caused an overall reduction of permeance of 32% for hydrogen and 53% for helium. Apparently, the introduction of niobium ions in

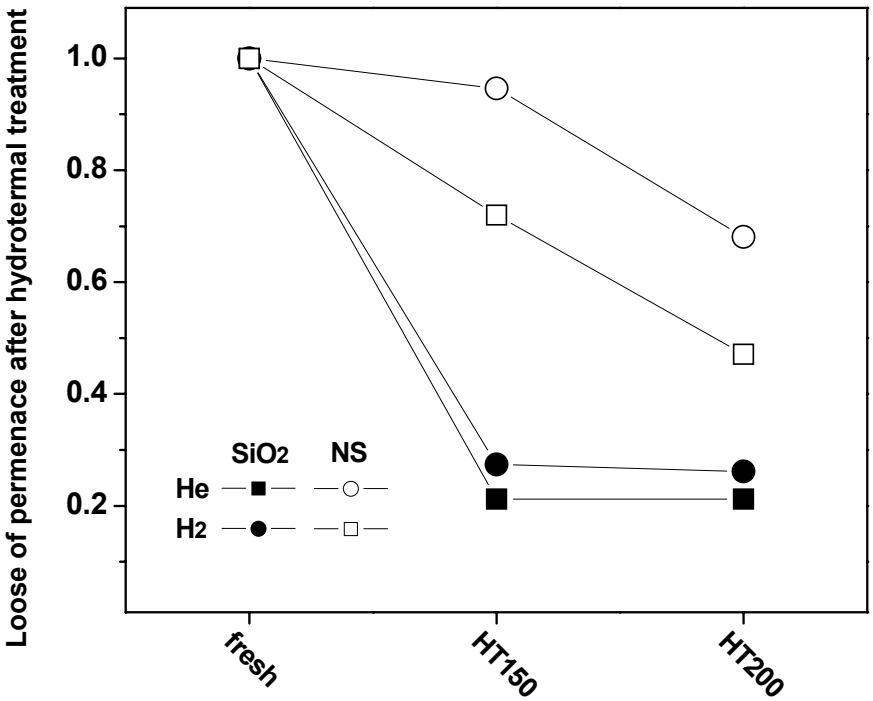

Figure 6.3. Reduction of the permeance of hydrogen and helium after HT150 and HT200 in the pure silica membrane (black symbols) and in the NS membrane (white symbols). The values were corrected for the support resistance, i.e., they refer to the top layer only.

the silica framework yielded a material that was more stable than pure silica is. The effect of Nb on hydrothermal stability is evident after treatment at 150 °C. After the second treatment, the structural change of niobia-silica was more substantial. The stabilization caused by the Nb ions is probably only kinetic, since as stated in the introduction, microporous amorphous structures are not thermodynamically stable and are prone to densification. Longer-term stability tests are required to understand in which extent Nb ions can stabilize the silica framework from steam. The higher stability of NS may also have been caused by the fact that the first one had larger pores than the latter one. Indeed, pores with higher curvature (smaller dimension) are more sensitive to hydrothermal degradation than large pore with small curvature. From the data presented here, it is not possible to estimate to which extent these two effects contribute to the stability of the NS layer.

Effect of hydrothermal modification on activation energy of permeance

It is possible that the structural reorganization of the material upon hydrothermal treatment affects the gas transport mechanism. Gas transport in a microporous regime occurs essentially according to a thermally activated surface diffusion mechanism. The transport rate can be expressed in terms of a modified Fick law [9], here rephrased as:

(6.2) $$F = F_0 \exp\left\{-\frac{E_a}{RT}\right\}.$$

Here F is the membrane permeance (flux per unit of driving force), E_a is the apparent activation energy, and F_0 is a temperature independent parameter that has the dimensions of permeance. The value of F_0 depends on the interaction between membrane surface and gas molecule, thickness of the gas-selective layer, and on pore shape and tortuosity.

A change of transport mechanism is usually reflected in a change of activation energy. The Arrhenius plots of the hydrogen and helium permeances of the top layers are shown in Figure 6.4 and Figure 6.5, The data were calculated using Equation 6.1. The gray lines in the picture show the linear fits to the data using Equation 6.2.

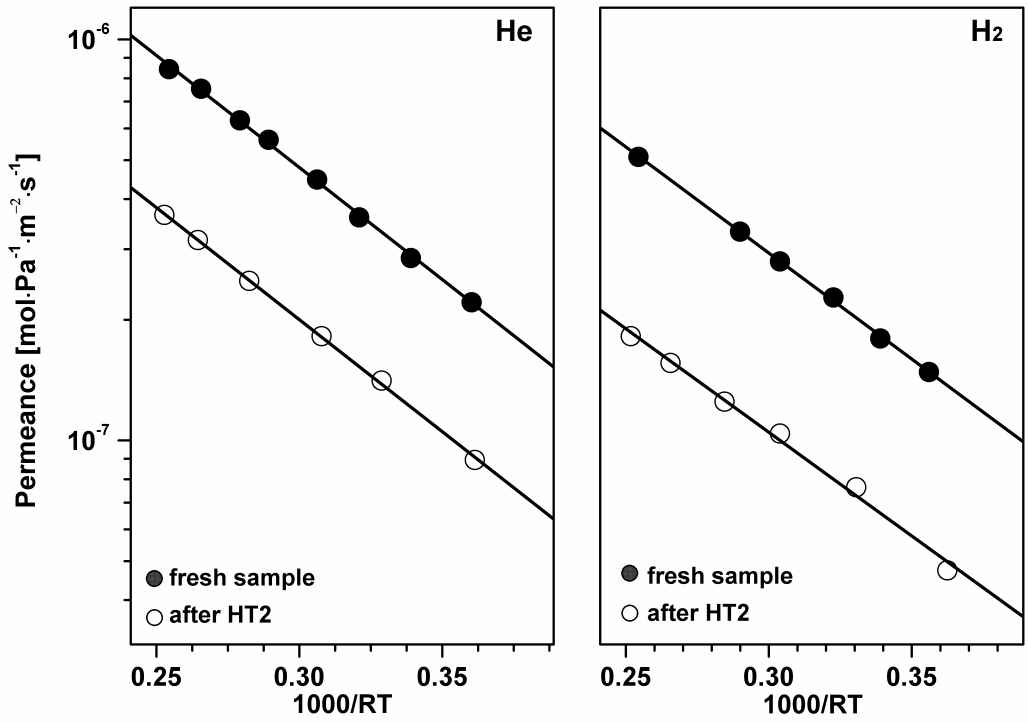

Figure 6.4. Arrhenius plot of the silica membrane, both fresh and after HT2. The data refer to the permeance of the top layer only.

The permeance of the silica membrane had an apparent activation of 12.8±0.3 kJ·mol^{-1} for helium and 12.2±0.2 kJ·mol^{-1} for hydrogen. After HT200, the activation energies were 12.9±0.1 kJ·mol^{-1} for helium and 11.9±0.4 kJ·mol^{-1} for hydrogen. These data provide no indication for a mechanistic change.

As can be seen in Figure 6.5, the experimental data of both hydrogen and helium for NS deviated from the exponential behavior predicted by Equation 6.2 in the lower temperature range. This may be attributable to the existence of two parallel transport paths. One path goes via micropores, the other path via larger pores. The latter path is probably associated with a Knudsen-type diffusion mechanism [5]. Knudsen diffusion does not depend strongly on temperature; its rate is proportional to $T^{0.5}$. The relative contribution to the overall flow of a parallel path that is dominated by Knudsen diffusion will therefore increase with decreasing temperature. At low

temperatures, it may even become the dominant path, as seems to be the case for NS at low temperatures.

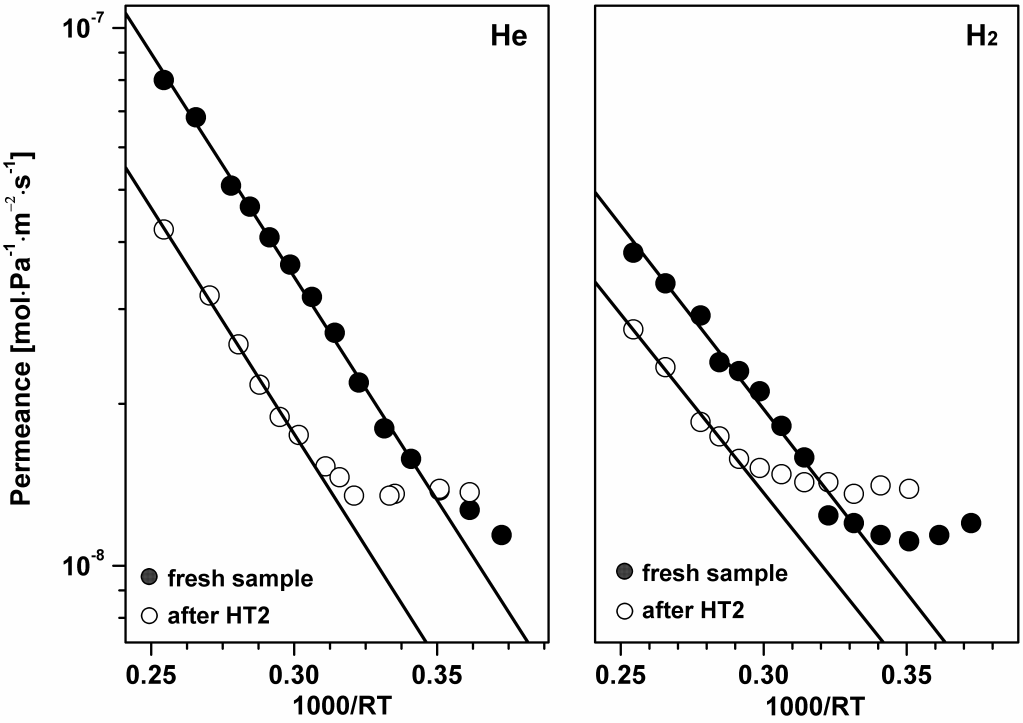

Figure 6.5. Arrhenius plot of NS membrane fresh and after HT2. The data were corrected for the resistance of the support.

The trend is also consistent with the fact that the deviation from Equation 6.2 was not observed in the silica membrane, where gas permeation experiments had already indicated the absence of large pores. The threshold temperature, $T_{Kn,}$ below which the permeance of the NS membrane deviated significantly from the predictions of Equation 6.2 were 70 and 90 °C for He and H_2, respectively. After hydrothermal exposure, T_{Kn} of hydrogen shifted from 90 to 130 °C and T_{Kn} of helium shifted from 60 to 115°C. Activation energies of 19.1±0.3 kJ·mol^{-1} for helium and 15.3±0.7 kJ·mol^{-1} for hydrogen were calculated from the permeance data of the fresh NS membrane in Figure 6.5. After HT2, the activation energies were found to be 19.3±0.6 kJ·mol^{-1} for He and 15.3±0.7 kJ·mol^{-1} for hydrogen. Thus, He and H_2 activation energies remained unchanged upon hydrothermal exposure of the NS membrane. A

similar observation was made by De Vos, who reported an apparent activation energy for hydrogen permeance of about 8 kJ·mol^{-1} for silica membranes calcined at different temperatures [4]. Silica membranes that had been calcined at 600 °C were found to be denser and have smaller pores than those calcined at 400 °C [4,7], but no change in activation energy was observed.

Hydrothermal densification as studied by nanopermporometry

The pore size distribution of a membrane can be also measured by permporometry. This technique was developed in the 1990s to analyze pore size distributions of mesoporous membranes [8]. More recently, Tsuru developed a permporometry technique that is able to assess the microporous regime [9,10]. Unfortunately, the interpretation of data collected with a nanopermporometer is much more complex than in conventional permporometry of mesoporous films. The Kelvin [11] and Knudsen [5] equations are not valid in the microporous regime [9], and simple alternative models have not yet been developed. Tsuru et al. therefore defined the average pore size as the Kelvin diameter at which the permeance of the vapor-containing gas was half of the permeance of the dry gas [9].

The setup shown in Figure 6.1 can be used as a nanopermorometer, since the relative pressure of water on the feed side can be controlled with a high degree of precision by the mass flow controllers MFC1 and MFC2. In the present study, the degradation of pure silica was analyzed with nanopermporometry. The permeability of the NS layer was too low to acquire sufficiently accurate data by nanopermporometry in our set-up. The Kelvin and Knudsen equations were used to calculate the corresponding Kelvin radii from the experimental data. Although the assumptions underlying these equations are not valid in the microporous regime, they allow qualitative and/or semi-quantitative comparison of pore size distributions of membranes, and are therefore suitable parameters to monitor the degradation of membranes. The Kelvin radii should not be taken directly as values with physical significance. Equation 5.1 [13] was used to analyze the permporometry curve shown in Figure 6.6.

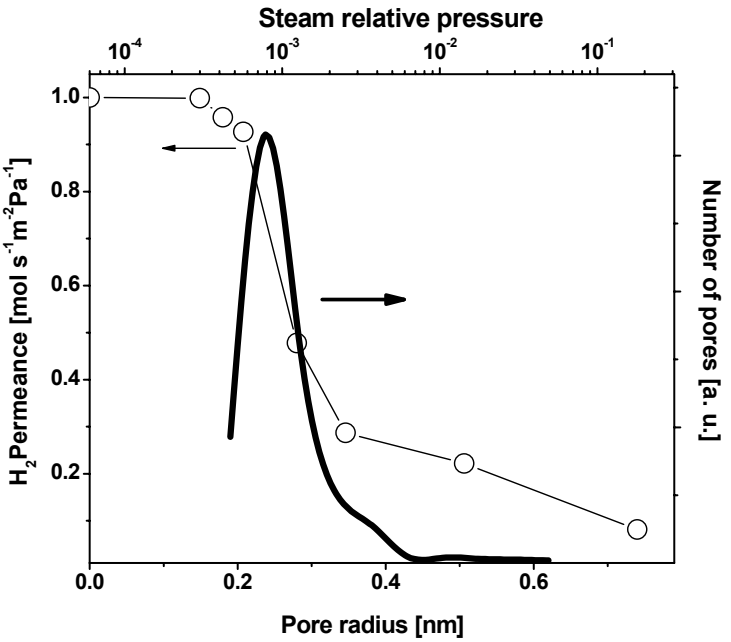

Figure 6.6. Analysis of microporous silica membrane by nanopermporometry. Measurement was done at 90 °C by using hydrogen as permeant and water as condensable vapour. The H_2 permeance was measured as a function of the relative pressure of steam (thin line). The pore size distribution (thick line) was calculated from Equation 5.1.

Figure 6.6 shows the variation of hydrogen permeance of silica as function of the partial pressure of steam in the feed. A strong reduction of hydrogen flux was observed when the relative pressure of steam was increased from $1.1 \cdot 10^{-2}$ to $7.0 \cdot 10^{-2}$, so most of the micropores were closed by capillary condensation of water. Beyond this point, the reduction of hydrogen permeance with relative pressure of water was less pronounced. At a relative pressure of about 0.2, the hydrogen permeance was less than the 10% of its initial value. Figure 6.6 also shows the pore size distribution of the silica membrane as calculated from Equation 5.1. The curve indicates a monomodal distribution with an average Kelvin diameter ($2r_k$) of about 0.5 nm. Figure 6.7 illustrates the permeance as function of the kinetic diameter of the gas probe molecules, after correction for the support resistance. In contrast to the interpretation of the nanopermporometry data, the qualitative pore size distribution that is obtained from this experiment is empirical. The effective pore size distribution obtained with nanopermporometry is shown for the sake of comparison.

Application of Equation 5.1 seems to lead to an overestimation of the pore diameter by about 0.2 nm in this case. However, it could also be equally well possible that an appreciable permeance only occurs in pores that are at least 1-2 Å larger than the kinetic diameter of the permeating molecule. This would imply that nanopermporometry cannot assess pores smaller than 0.4-0.5 nm, since the water, hydrogen and helium molecules used in that experiment have a kinetic diameter of about 0.2-0.3 nm.

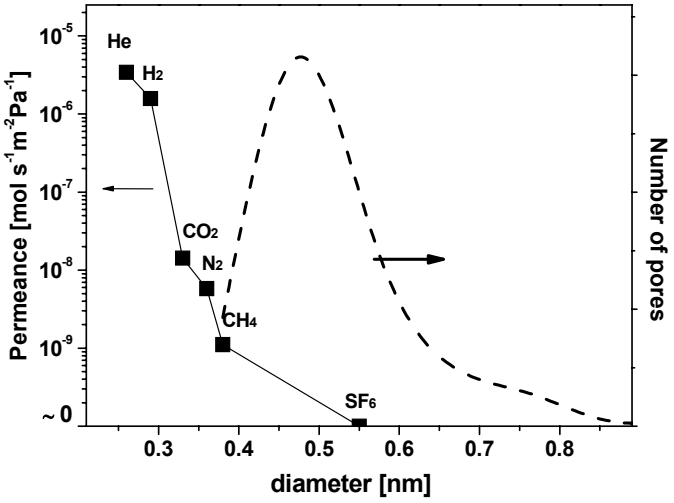

Figure 6.7. Permeance of silica top layer as function of the kinetic diameter of the probe molecule (solid line) and pore size distribution obtained by nanopermporemetry (dashed line). The permeances were corrected for the support resistance.

We applied nanopermporometry to characterize degradation phenomena in microporous silica membranes by investigating changes in the pore size distributions of the gas selective top layers after hydrothermal treatment.
Results are depicted in Figure 6.8. The data obtained with this method support the trends shown by single gas permeation measurements. As can be seen in Figure 6.8b, the fraction of pores larger than 0.6 nm decreased after hydrothermal treatment. Apparently, densification narrowed all pores indiscriminately, reducing both the permeance of the membrane and the

number of large pores. The change of pore size is more pronounced during the first hydrothermal treatment at 150 °C. This is in agreement with the results of the single gas permeation experiments.

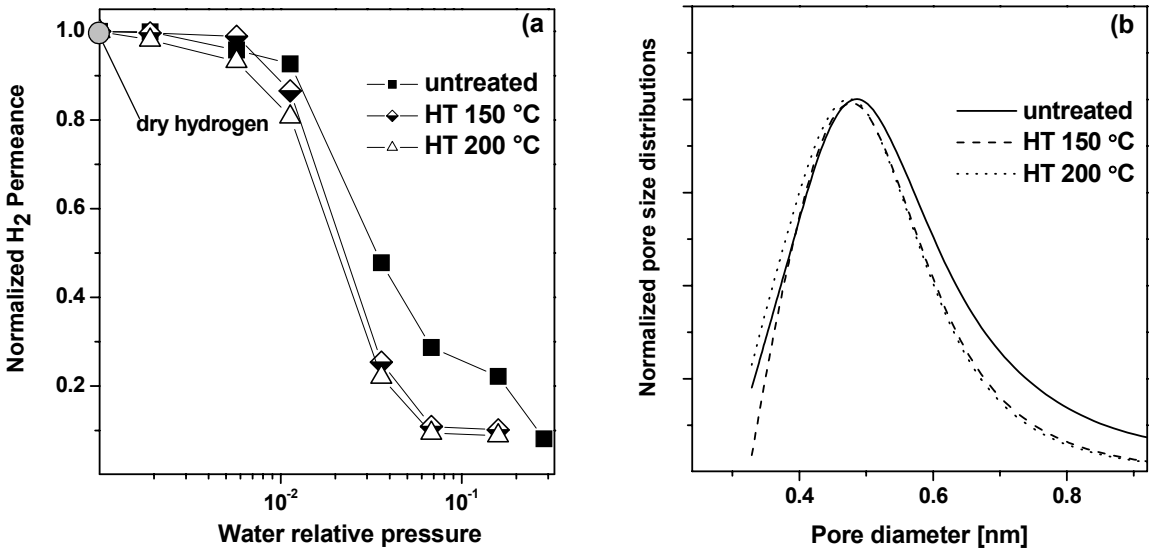

Figure 6.8. Densification process in silica membrane as observed by nanopermporometry. (a) Normalized permeance and (b) pore size distribution.

As was already mentioned, due to the low permeability and small membrane area, it was not possible to perform permporometry measurement on the NS membrane.

Hydrothermal modification mechanism

A possible mechanism for the modification of pore structure upon hydrothermal treatment is schematically illustrated in Figure 6.9. The pore structure of microporous silica [14], and probably of NS too, roughly resembles that of a sponge. The pores with larger curvature, i.e., ultramicropores and bottlenecks, are more vulnerable to hydrothermal attack than pores with smaller curvature, such as micropores and mesopores. According to the densification mechanism proposed here for the NS material, only a small fraction of the porous structure was densified during the limited time of

exposure to hydrothermal conditions. Bottlenecks in the microporous thin layer became blocked, thereby increasing the actual length of the transport path of small molecules through the membrane. This may explain why the reduction of hydrogen and helium permeance was substantial, while no variation of activation energy could be detected.

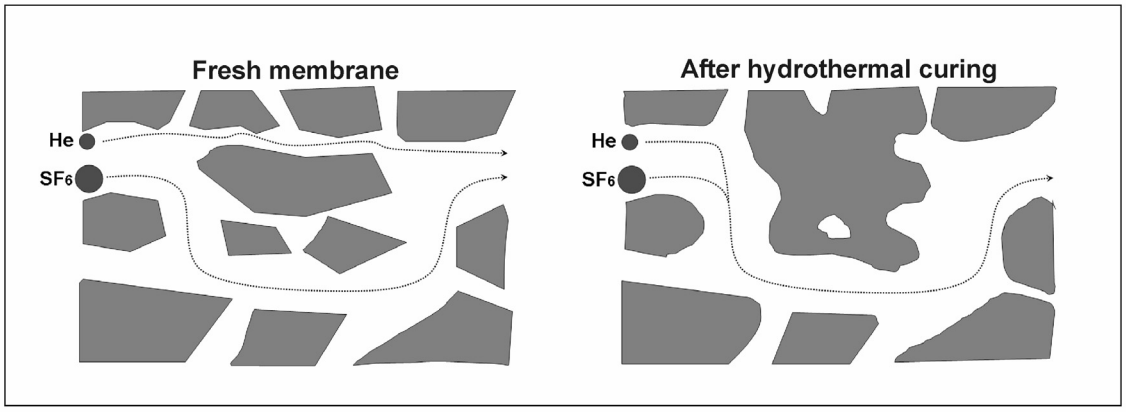

Figure 6.9. Scheme of the possible hydrothermal modification of the NS microporous structure. The effective path length of a helium molecule through the membrane is increased after steam exposure, while the permeation of sulfur hexafluoride in the larger pores of the NS membrane is not affected or mildly positively affected by the hydrothermal treatment.

Densification of the silica base structure upon steam exposure also causes large pores to become larger. This is in qualitative agreement with the data reported in Table 6.2. The permeance of larger molecules like CH_4 and SF_6, which are mainly transported through the largest pores of the membrane, either remained the same or increased after HT1 and HT2. Nanopermporometry analysis and the permeation experiments showed that only ultramicropores were present in the pure silica membrane, and not the larger pores that are represented in Figure 6.9. Hydrothermal curing of silica therefore caused a reduction of permeance for all probe molecules that were able to permeate through the membrane.

The proposed densification mechanism can also explain why the shift of T_{Kn} after HT2 was more pronounced for helium than for hydrogen. The pores that were only accessible to He and not to H_2 are expected to be the first to be

occluded during hydrothermal treatment, while defects and large pores are expected to remain unaffected by steam exposure.

6.4. Conclusions

The NS membrane appeared to be more hydrothermally stable than the silica membrane under the testing conditions. The data reported here suggest that NS membranes can be applied up to 150 °C under hydrothermal conditions with a reduction of the hydrogen permeance of only 5%. Longer stability tests will reveal to which extent the presence of Nb ions can stabilize the microporous network by slowing down the kinetics of densification.

By comparing the data from single gas permeation measurements with the pore size distribution obtained by nanopermporometry, it was shown that the latter technique can be applied to estimate the pore size distribution of microporous layer in a semi-quantitative way. Hence, in principle, this fast and non destructive technique may be applied to a large number of systems where a comparison among membranes is required.

6.5. References

[1] D.W. Lee, B. Sea, K.Y. Lee, K.H. Lee, Ind. Eng. Chem. Res., 41 (2002) 3594.

[2] A. Brunetti, G. Barbieri, E. Drioli, T. Granato, K.H. Lee, Chem. Eng. Sci. 62 (2007) 5621.

[3] M. Asaeda, Y. Sakou, J.H. Yang, K. Shimasaki, J. Membr. Sci. 209 (2002) 163.

[4] R.M. de Vos, H. Verweij, J. Membrane Sci. 143 (1998) 37.

[5] R.R. Bhave, "Inorganic Membranes: Synthesis, Characteristics and Applications", Van Nostrand Reinhold, New York, 1991, p. 338.

[6] V. Boffa, J.E. ten Elshof, A.V Petukhov, D.H.A. Blank, Adv. Funct. Mater. submitted.

[7] R.M. de Vos, H. Verweij, Science 279 (1998) 1710.

[8] G.Z. Cao, J. Meijerink, H.W. Brinkman, A.J. Burggraaf, J. Membr. Sci. 83 (1993) 221.

[9] T. Tsuru, T. Hino, T. Yoshioka, M. Asaeda, J. Membr. Sci. 186 (2001) 257.

[10] T. Tsuru, Y. Takata, H. Kondo, F. Hirano, T. Yoshioka, M. Asaeda, Sep. Purification Tech. 32 (2003) 23.

[11] D.D. Do, Adsorption Analysis: Equilibria and Kinetics, vol 1, Imperial College Press, London, 1998, p.115

[12] D.W. Breck, Zeolite Molecular Sieves-Structure, Chemistry, and Use, John Wiley & Sons, New York, 1974, p. 636.

[13] V. Boffa, J.E. ten Elshof, D.H.A. Blank, Mesoporous Microporous Mat. 100 (2007) 173.

[14] T. Yoshioka, T. Tsuru, M. Asaeda, Mol. Phys 102 (2004) 191.

CHAPTER 7

Templated Silica Membranes onto a α-Alumina Support*

Abstract

A simple method for depositing mesoporous silica films directly on macroporous α-alumina supports is reported. A polymeric silica sol was prepared by hydrolysis of tetraethylorthosilicate in acid propanol at the presence of hexadecyltrimethylammonium bromide as template. The rheology of the sol was changed by a modified urea-based thixotropic agent, which was used in a concentration range between 2% and 10% on volume. The dynamic viscosity of the sol was measured as a function of shear rate. The rheology modifier was found to increase the viscosity of the sol and confer at the same time a thixotropic behavior to it. Long range order in the unmodified and modified materials was analyzed by XRD on powders after calcination at 500 ºC. It was found that the pore size increased with increasing concentration of additive, while the degree of order decreased until eventually, at high concentrations, the ordered porous structure collapsed completely. The gradual pore size increase at lower concentration is thought to be caused by swelling of the surfactant micelles by the rheology modifier.

The modified sols were deposited via dip-coating on α-alumina disks. The morphology of the silica top layers was characterized by SEM. Pore size distributions and permeances of the prepared membranes were assessed by permporometry and single gas permeation measurements, respectively. The membranes had narrow pore size distributions, with an average diameter of about 2 nm. Permeabilities of H_2, He, CH_4 and O_2 were compared. Hydrogen permeances up to $6 \cdot 10^{-7}$ mol·s^{-1}·m^{-2}·Pa^{-1} were measured at 473 K. The gas flux across the membrane follows a Knudsen-type mechanism, as shown by the permselectivities.

* published on V. Boffa, J.E. ten Elshof and D.H.A. Blank, Microporous Mesoporous Mater. 100 (2007) 173.

7.1. Introduction

With the aim to increase the permeability of the membranes, γ-alumina was substituted by templated mesoporous silica. Indeed templated silica is one of the most attractive materials for those applications in which a high specific surface area and a narrow pore size distribution in the mesoporous range are required [1,2]. Among all the organic molecules that can be used to tailor the pore structure of the silica matrix, surfactants are the most flexible ones. Silicon oxides with lamellar, hexagonal or cubic pore structure can be obtained under different synthetic conditions by using non-ionic or cationic surfactants as templates [3,4]. The interest in this new class of materials grew when it was discovered that glasses with regular porous structure were formed in the presence of quaternary ammonium surfactants (M41S materials) [5-6]. It was directly recognized that these materials may be applicable in a large number of fields beside heterogeneous catalysis; for example as membranes, sensors and in nano-electronics [7,8]. The two main requirements for a membrane are high selectivity and high permeate flux [9]. Thus, templated glasses, which have a high porosity and a regular pore structure, are really attractive materials for the preparation of selective ceramic membranes [10].

In the first report in which a surfactant templated silica layer was applied in a stacked membrane, it was used as a spacer [11] between the mesoporous sub-layer and the microporous top layer of a ceramic gas separation membrane. The spacer prevented penetration of the top layer into the sub-layer during deposition. In later works templated silica has also been used to replace the conventional mesoporous intermediate layers [12-14]. However, the application of templated silica films directly on a macroporous support is not trivial. Indeed both sol synthesis and membrane coating procedure are critical steps.

In the first years after the discovery of ordered mesoporous oxides the focus was mainly on the preparation of powders and thin films on dense substrates [5,15]. However, the recipes that were developed for these cases are often not suitable for preparing membranes. Only a stable silica sol, with polymeric particles in the nanometer-size region, can yield a gas-selective

membrane. Highly ordered M41S powders can be prepared easily at basic pH via strong electrostatic interaction between the cationic ammonium salt (S^+) and the negatively charged silica particles (I^-) [16,17]. The S^+I^- type interaction is commonly used for making powders. However, in order to synthesize a stable polymeric sol, a high degree of control over the condensation reaction is required. At basic pH the rapid condensation of silica particles would lead to fast precipitation or gelation. But when the pH is slightly below the silica isoelectric point at pH 2-2.5 [18], the condensation rate is at a minimum and it is possible to obtain transparent sols that are stable for many days even at room temperature. Nevertheless, under such conditions the interaction between the cationic surfactant and the slightly positively charged silica particles (I^+) is weaker and it is mediated by the surfactant counterion (X^-). Under such conditions, which are generally described as $S^+X^-I^+$ interactions, it is more difficult to obtain an ordered structure [16]. Furthermore, coating the sol onto a porous support is far more difficult because of the perturbing effect of the substrate on the drying film. Substrate roughness and capillary forces exerted by the substrate pores can easily result in film cracking or distortion of the ordered mesostructure [19]. The coating of a templated silica gel on a macroporous substrate such as α-alumina differs from the coating of traditional colloidal sols like boemite [20], titania [21] or zirconia [22]. In the latter cases the sol is formed by dense particles that have a size between 20 and 50 nm. Large quantities of binder such as polyvinyl alcohol (PVA) are added to change the rheological properties of the sols and the viscoelastic properties of dried uncalcined films. The coating of polymeric silica sols onto α-alumina supports is complicated by the fact that the polymeric silica sol is formed by particles that are far smaller (only a few nm [23]) than the pores of the support, which are often larger than 80-100 nm diameter. Furthermore, binders can be used only in small concentrations in order not to affect the supramolecular ordering of the surfactant micelles. The necessity to work in a restricted range of synthetic conditions, the difficulty to coat a polymeric sol onto a macroporous support, and the impossibility to use ordinary binders

makes the coating of mesoporous silica films on porous substrates a challenge. Templated silica membranes applied directly on α-alumina substrates were successfully made by Roy Chowdhury et al. via dip coating [12,13], and by Huang et al. via casting [14]. Solvent transport through membranes prepared by Roy Chowdhury et al. showed behavior which is typical for truly mesoporous systems. On the other hand, the XPS depth profiles implied the absence of a real silica layer after calcinations [12]. The concentration of aluminium at the surface of the membrane was larger than that of silicon, which suggests that the membrane was constituted by silica penetrated into the substrate [13,24].

In recent years two solutions to this problem have been proposed. The most common way for preparing templated silica membranes is via hydrothermal growth of the material on top of a substrate. The substrate is immersed in a mixture containing surfactant, solvent and an organic or inorganic silica precursor [25,26]. Water and a base are present to promote the hydrolysis and condensation reactions that lead to the formation of silica. Membranes obtained with this procedure were gas selective and applicable in nanofiltration processes [27]. In spite of that, silica grew both inside and on top of the support, forming a resistive thick layer. An alternative procedure has been introduced by Boissière et al. [28]. A tubular support was impregnated by an aqueous solution of NaF. NaF catalyzes the condensation reaction of the silica precursor. In this way the growth of the selective silica layer was restricted to the area on top of the support. In order to be reproducible this procedure requires a high degree of control over all the parameters involved in the preparation.

Here a different approach to deposit templated mesoporous silica membranes directly on macroporous supports is proposed. It involves tuning of the rheological properties of the sol to render it a thixotropic behavior, so that it can be coated directly on a macroporous substrate. I modified the rheological properties of a polymeric silica sol by adding BYK-420 (kindly provided by BYK-Chemie, Wesel, Germany), which consists of a modified urea solution. BYK-420 is a commercial additive used in aqueous coatings to improve anti-

sagging properties or as anti-settling agent for pigments. This product is able to increase the viscosity of a suspension, conferring thixotropy at the same time. The thixotropy inhibits penetration into the pores of the α-alumina substrate during the drying stage of the silica film. This behavior can simplify the processing of polymeric sols in the preparation of silica membranes.

7.2. Experimental part

Sol synthesis

Aqueous nitric acid (0.05 N) was dropped under vigorous stirring in a conical flask containing a solution of tetraethylorthosilicate (TEOS, 98% purity, Aldrich), in 1-propanol (analytical grade, Acros). After 5 minutes the templating agent cetyltrimethylammonium bromide (CTAB, ≥99% purity, Aldrich) was added. The molar ratio of the final mixture was TEOS/CTAB/1-propanol/H_2O/HNO_3 = 1/0.13/15/15.5/0.14. All reagents were mixed under nitrogen atmosphere in order to avoid the hydrolysis of TEOS before the reaction started.

The mixture was heated at boiling temperature for 2 hours under reflux; then it was allowed to cool down. The transparent sol was kept at 5 °C for a few days until it was used for sample preparation.

Thin film deposition and powder preparation

α-Alumina disks were used as macroporous supports for film deposition. They were prepared as described at page 24.

Varying amounts of BYK-420 (BYK-Chemie, Wesel, Germany) were added to the aged silica sol and the mixture was stirred for a few hours. The alumina macroporous supports were then dip-coated in the solution under class-1000 clean room conditions. The samples were dried at 40 °C in air (60% relative humidity) for 3 hours. The membranes were then fired at 500 °C for 3 h (heating/cooling rates of 0.5 °C/min). After deposition of the first layer macropores in the support could still be detected by permporometry in all

samples, irrespective of BYK-420 concentration. In order to cover these defects a second coating layer was applied, followed by calcination.

Table 7.1. Coating solutions (S) used in this work for the preparation of powders (P) and membranes (M).

Coating solution	BYK-420 volume fraction	Name of unsupported sample	Number of layers	Name of membrane
S00	0.00	P00	*	*
S02	0.02	P02	2	M02
S06	0.06	P06	2	M06
S10	0.10	P10	2	M10

*No membranes were obtained without BYK-420.

Powders were prepared by drying the same sols as used for thin films in plastic Petri-dishes. Table 7.1 lists the different concentrations of additive used for preparing powders and thin films. For the sake of simplicity I will refer to the samples following to designations listed in Table 7.1.

Characterization

The viscosity of the coating sols were measured by a Brookfield DV-II+ Programmable Viscometer (Brookfield Engineering Laboratories, Middleboro, MA, USA). The instrument was calibrated using Brookfield Fluid 5 (Brookfield Engineering Laboratories, Middleboro, MA, USA) as standard. The viscosity of this fluid is 4.8 mPa·s at 25 °C. The temperature was kept constant at 30 °C by a thermostatic water bath. The viscosity was measured using a 90 mm long cylinder with a diameter equal to 25 mm and a weight of 78.5 g. The cylinder was stirred in 25 ml of sample contained in a metallic tube. Data were recorded with increasing angular speed, ranging from 1.0 to 10.5 s^{-1}, followed by stepwise decreasing the speed to 1.0 s^{-1}.

All data on powders and films reported in this Chapter concern calcined samples. XRD patterns of powders were recorded using a Philips SR5056 with Cu Kα radiation. Nitrogen sorption measurements were performed at 77 K on calcined silica, using a porosimeter (Micromeretics, ASAP 2400). Pore size distributions of templated silica membranes were measured by permporometry

using the type of set-up described by Cao et al. [29,30]. In the permporometer the flux of oxygen across the membrane was measured by a Varian 3300 gas chromatograph (Varian, Palo Alto, CA, USA). Scanning Electron Microscopy (SEM) images were taken on a LEO 1550 FEG. Single gas permeation measurements were carried out in a death-end mode permeation set-up [31]. The gas flow was measured with a soap film flow meter.

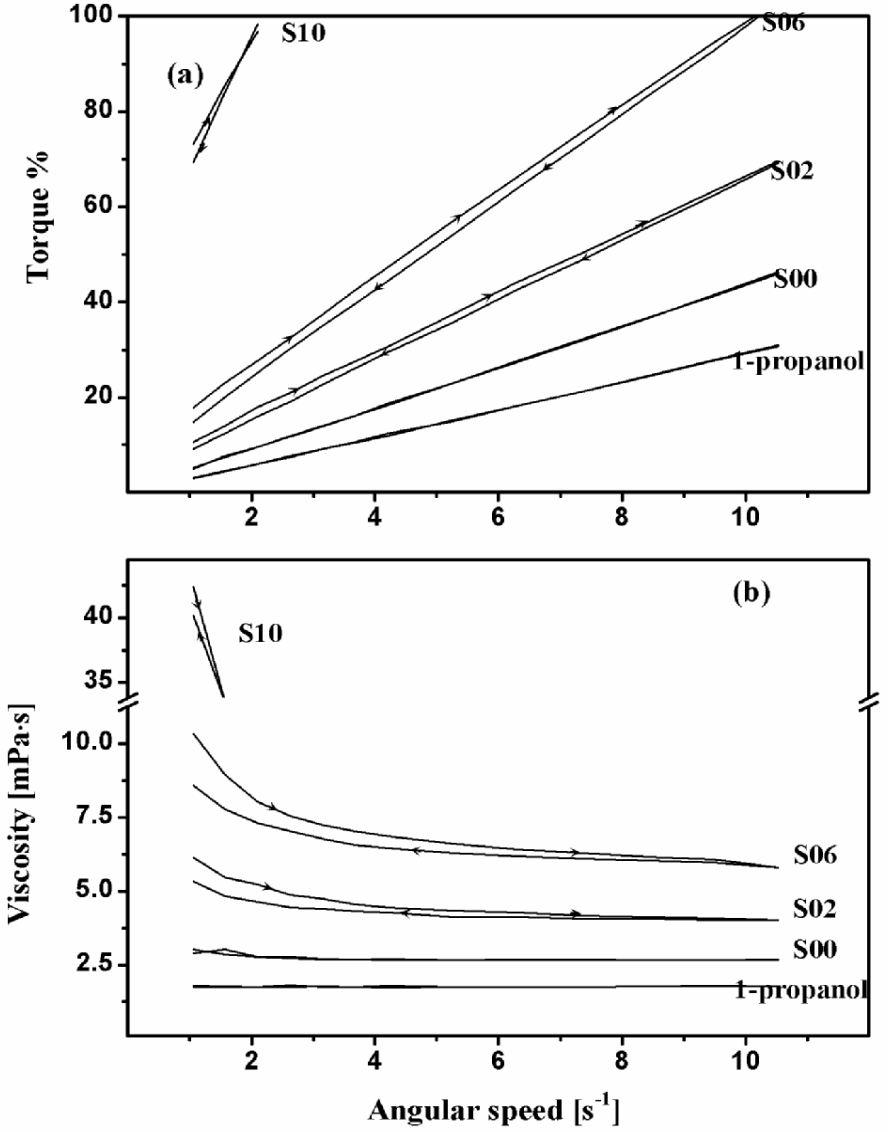

Figure 7.1. Rheological properties of solvent and silica sols, before and after being modified with BYK-420. (**a**) Torque stress against the cylinder angular speed; (**b**) viscosity versus angular speed. The names of the samples are indicated on the right side of the graphs.

Hydrogen, helium, methane and oxygen permeances were measured on different samples at 200 °C, with a pressure of 4 bar on the side of the feed and atmospheric pressure on the retentate side. Since atmospheric water can condense in the pores of the silica matrix, all membranes were dried at 200 °C in a hydrogen flow for at least 16 h before measurements were done. In a typical series of measurements, the permeation rate of different gases was determined starting from the one with the lower molecular mass, and equilibrating at least two hours each time a new gas was introduced into the set-up.

7.3. Results and discussion

Sol modification

BYK-420 is a pale yellow solution and 52% of the total weight is non-volatile material. It is constituted by modified urea, which is stabilized in solution by N-methylpyrrolidone. Once the product has been added to the final coating solution the modified urea crystallizes in the ethanol-based solution, yielding thin fibers which result in a tridimensional network. This network confers pseudo-plastic behavior to the coating mixture. BYK-420, like other products with similar composition, is effective at 1-3% in volume, but cannot be applied to all sols. In very polar or highly non-polar systems the active component precipitates in the form of white powder.

The rheological properties of the modified sols are shown in Figure 7.1. Prior to measurement, the coating solutions were prepared by stirring 50 ml of silica sol with an adequate amount of additive for 2 h. Figure 7.1a shows the torque versus angular speed of different solutions. The viscosities of solvent and sols shown in Figure 7.1b were calculated from these data according to the formula reported at page 27.

As can be seen in Figure 7.1b, the viscosity of both solvent and unmodified sol is independent of shear rate, which indicates that they behave as Newtonian fluids. The viscosity of 1-propanol was measured to be 1.76 mPa·s, which is in

agreement with the literature value of 1.72 mPa·s at 30 °C [32]. The viscosity of the unmodified coating sol S00 was measured to be 2.71 mPa·s.

After addition of the modifier the viscosity increased over the whole range of shear rates. The increasing viscosities at lower shear rates shown in Figure 7.1b indicate the occurrence of pseudo-plasticity in the sols. After leaving the sols undisturbed for a while it was seen that the viscosity at the onset of a measurement increased to values higher than 5 mPa·s for sample S02. The sol also became thixotropic after addition of BYK-420, since it was observed that the high viscosity of the coating solution is partially reduced upon prolonged stirring. These observations show that BYK-420 can be a suitable rheology modifier to tune the visco-elastic properties of silica sols. The appearance of S10 was turbid. Turbidity usually implies that it is not suitable for preparation of a defect-free membrane coating. A membrane was however prepared with this sol and its permporometry profile will be shown below. Concentrations of additive higher than 10 vol% on total volume resulted in unstable silica sols in which precipitation occurred rapidly.

Powder analysis

Templated silicon oxides were prepared as powder with the aim to analyse the intrinsic properties of the material and to study the effect of the rheological additive on the mesoporous structure. The XRD profile of P00 in Figure 7.2 after calcination at 500 °C shows a broad peak at 2.7° 2θ, indicating the presence of long range order.

Figure 7.2 also shows the XRD patterns of 3 powders prepared with different concentrations of BYK-420, and calcined at 500 °C. The XRD peak of P02 is broader but more intense than the one obtained from P00. The increased peak intensity can probably be explained by the longer drying time of sol S02, which is due to the presence of the slow evaporating cosolvent N-methylpyrrolidone. As a result the micelles have more time to form an ordered mesostructure. In general, we found that the rheological additive had a perturbing effect on the degree of order in the templated microstructure: from P00 to P06 the peak

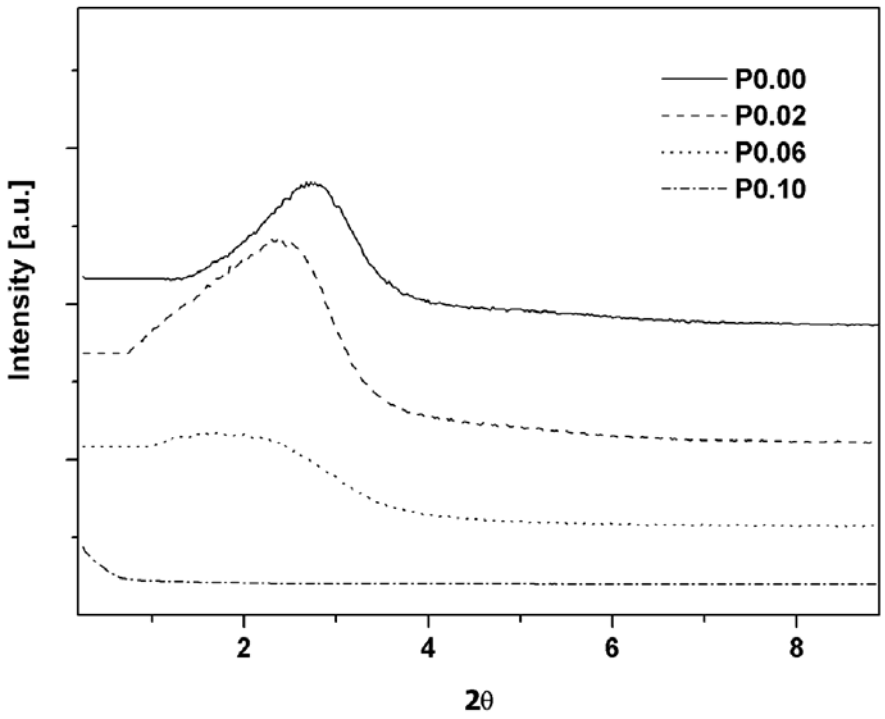

Figure 7.2. XRD patterns of powders obtained with different concentrations of BYK-420 after calcination at 500 °C.

became progressively wider and in the case of P10 it had disappeared completely. We may suppose that at least one of the components of BYK-420 is strongly interacting with the surfactant and perturbing the formation of micelles. Both solvent [33] and organic modifier [34,35] may cause the micelles either to swell or shrink, leading to larger or smaller pores in the final oxide. However, it has been noticed that the degree of long range order is higher when no perturbing agents are present [3]. Anderson et al [36], for instance, monitored by XRD the long range order in templated silica obtained by hydrolysis of tetramethoxysilane in aqueous methanol. The long-range order of the material decreased as the methanol concentration increased, while at concentrations higher than 70 wt% a disordered arrangement of pores was observed. In Figure 7.2, the shift of the reflection signal from 2.7° for P00 to about 2° for P06 suggests that BYK-420 causes an enlargement of the surfactant micelles. Indeed, similar XRD results have been obtained, for

instance, by adding decane as swelling agent to a silica sol in the preparation of MCM-41 [37].

These considerations are supported by the sorption curves in Figure 7.3 and the data listed in Table 7.2. The increase of the concentration of rheology modifier led to the formation of a denser material, with lower specific surface area and porosity, and larger pores. Comparison of the sorption curves of P00 and P02 indicate that a small amount of additive BYK-420 does not change the total porosity of the material considerably, but it does increase the degree of mesoporosity, as illustrated by the BJH pore sizes in Table 7.2. At higher concentrations of BYK-420 the specific surface area decreased and the pores became larger. In the case of P10 a hysteresis loop appeared in the sorption-

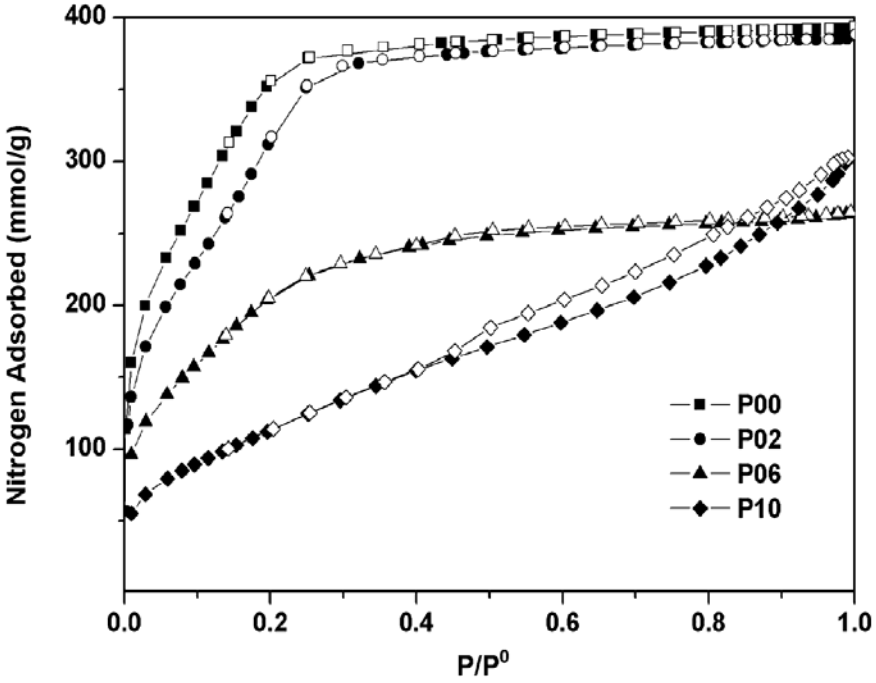

Figure 7.3. Nitrogen sorption isotherms at 77 K for four samples prepared with various BYK-420 concentrations: adsorption (black bullets) and desorption (white bullets) isotherms are shown.

desorption cycle. The specific surface area was reduced from 1220 $m^2 \cdot g^{-1}$ in P02 to 423 $m^2 \cdot g^{-1}$ in P10, while the average pore diameter of P10 was 4.2 nm, more than double of that measured for P00. It is stressed that the average pore diameter was calculated from the BET pore volume and specific surface area.

While the pore size distributions of P00, P02 and P06 were narrow, the pore size distribution of P10 was broad. Hence, although P10 has an average pore diameter of about 3.9 nm, this value is not so relevant in view of the broadness of the distribution.

Table 7.2. BET surface area, pores fraction and average pore width as obtained from nitrogen sorption data.

	BET Surface area [m^2/g]	Porosity	BET average pore width [Å]
P00	1380	0.61	18
P02	1220	0.60	20
P06	790	0.40	21
P10	420	0.44	42[#]

[#] Average value of pores smaller than 650 Å. This is an average value of a broad distribution.

SEM images

Figure 7.4a and b show SEM pictures of doubly coated and calcined M02 at different magnifications. The templated silica layer is seen to completely penetrate the support, without forming a continuous layer on top. Penetration into the support was inhomogeneous and was at least a few micrometers in depth. Upon increasing the concentration of the rheological additive to 6 vol%, a continuous flat layer was obtained as shown in Figure 7.4c. The layer covered the rough support, yielding a thin film with a long range modulation of ~1 μm period. In Figure 7.4d a close-up of an α-alumina grain covered by the silica film is shown.

The picture shows how the grains of the support are responsible for the modulation of the silica film. After the second coating a smoother layer was obtained, as shown in Figure 7.4e. Thickness and morphology of the first and the second coated layer after calcination can be compared in Figure 7.4f. In the figure the different layers are marked by white bars. The thickness of the first layer is inhomogeneous along the membrane surface, depending on whether it covers voids or α-alumina grains. In contrast, the second layer is about 170 nm

thick over the entire surface area of the membrane. The surprising difference in morphology between the first and second coated silica layers is noted. The second coated layer looks more compact and is more regular than the first one. Indeed it is well known from literature that the morphology of the support plays an important role in the development of morphology of templated silica films [42,43].

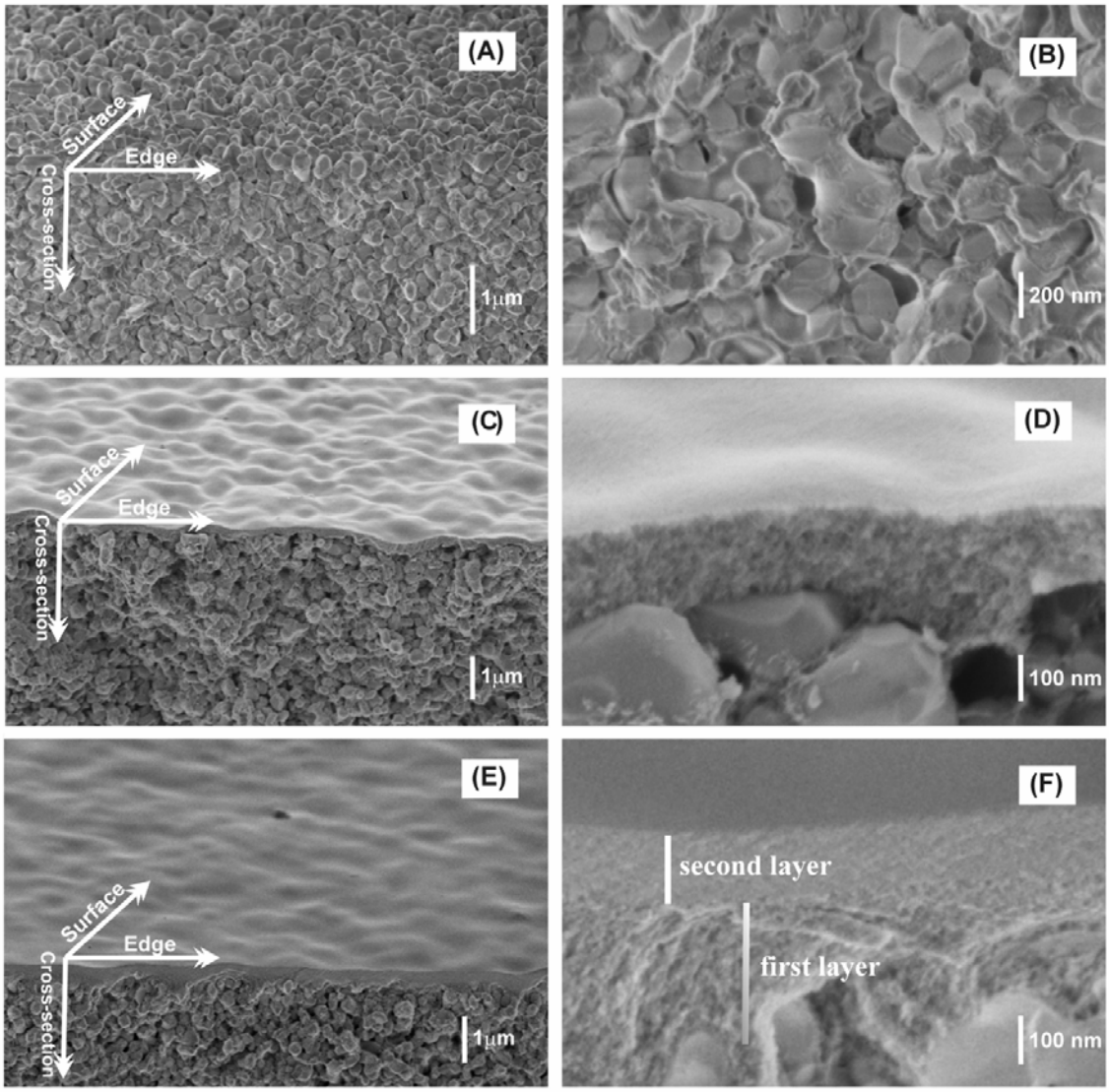

Figure 7.4. SEM pictures of membranes prepared with different binder concentrations. (**A**) M02 twice coated: cross section and surface. (**B**) M02: penetration of the silica sol inside the pores of the support. (**C** and **D**) M06 after the first coating. (**E** and **F**) M06 after the second coating.

Permporometry

The results of permporometry measurements are reported in Figure 7.5a. In order to calculate the pore size distributions it was assumed that gas diffusion occurred in the mesoporous regime; therefore the transport across the membrane can be expressed by the Knudsen equation [41]. This assumption is justified by the fact that in literature Knudsen flow has been reported for silica membranes that had been prepared with CTAB micelles as templates [42].
For this reason Equation 2.4 was used to calculate the pore size distribution of M06 in the different stages of its preparation, as shown in Figure 7.5b. The distributions were normalized to unity. The support has pores with Kelvin radii larger than 40 nm. After the first deposition of S06 two different kinds of pores were detected (see Figure 7.5b): a distribution of pores with main radius equal to 1.3 nm, which is a typical value for CTAB-templated silicas [25], and larger pores, which may be the macropores of the support that are only partially occluded by the deposited layer. After the second coating the average pore Kelvin radius was about 1 nm and no defects were detected. As we already mentioned, we were not able to prepare a defect-free membrane based on just one dip-coated layer. For this reason a second coating was applied on all samples presented in this chapter.
M02 and M06 showed similar permporometry profiles, but M02 was more permeable to oxygen. Despite the fact that no layer was observed with SEM (see Figure 7.4a), in M02 the deposited templated silica film appeared to form a selective barrier with pores smaller than 5 nm. Therefore we may conclude that the membrane is defect-free. In Figure 7.5c the pore size distributions of the powder and the membrane obtained from S02 are compared. In the case of the powder the distribution was calculated by nitrogen desorption at 77 K using the BJH method. Although pores with radius smaller than 2 nm cannot be assessed with this method, the assumptions on which the calculation is based are similar to those that have been used above for the determination of a distribution from the permporometry measurement, namely (1) pores in the mesoporous regime, (2) validity of the modified Kelvin equation and (3)

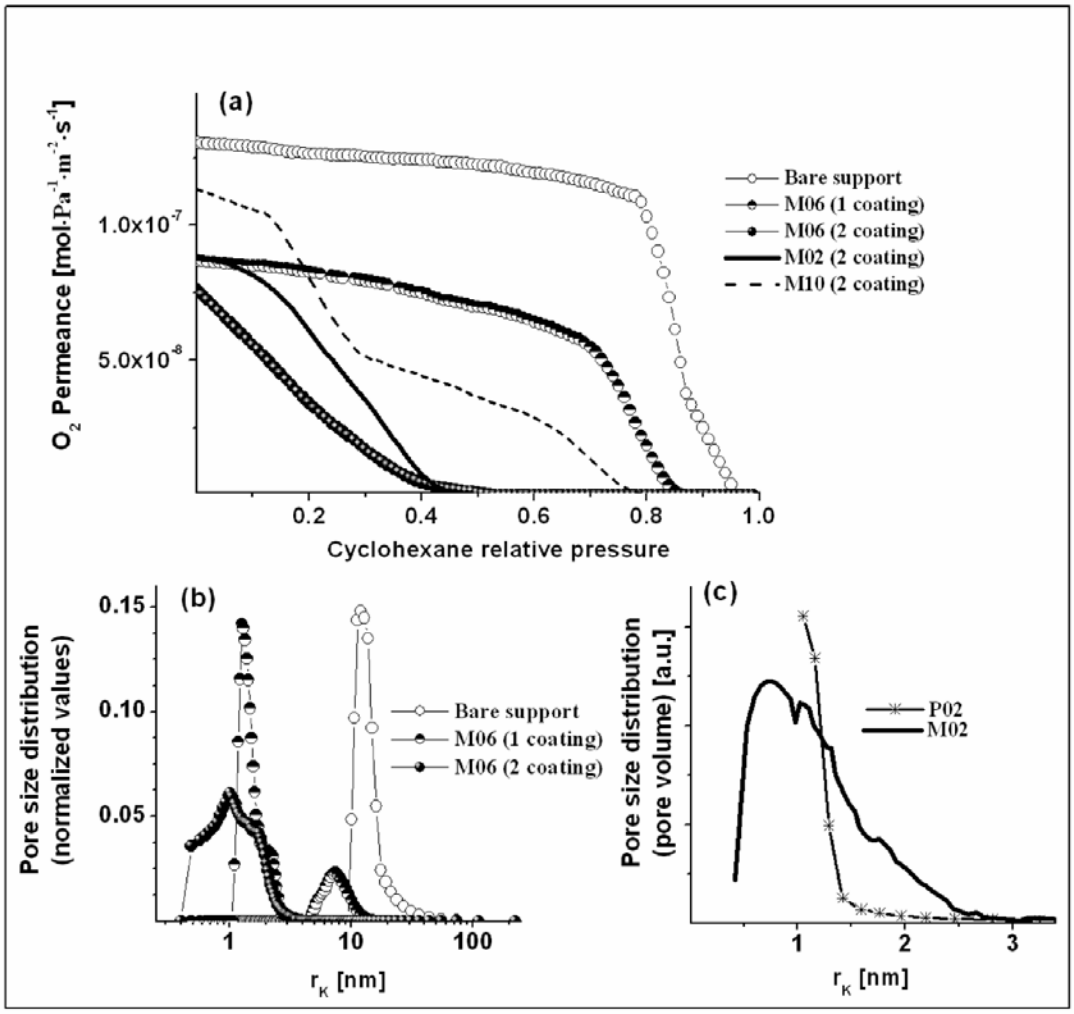

Figure 7.5. Permporometry analysis of support and membranes: (**a**) oxygen permeance as function of the cyclohexane relative pressure; (**b**) evolution of the pore size distribution of M06 in the different stages of the membrane preparation, calculated according to the Equation 4; (**c**) comparison between the pore size distributions of powder (N_2 desorption, BJH method) and supported film (permporometry, desorption mode) obtained from the sol S02.

cylindrical pore shape. Hence direct comparison of the two curves, which are derived from materials obtained from the same sol, is allowed. The average pore diameter of supported silica M02 was calculated from the distribution in Figure 7.5c and was found to be 1.8 nm. This value is comparable with the one obtained for P02, which was 2.0 nm. Despite the fact that the main pore width is almost the same for the two samples, the pore size distribution of the supported film seems to be broader than that one of the powder, and it also has a consistent number of larger pores. This difference can be attributed to the

lower shrinkage of the supported material during calcination as a result of being clamped to a rigid support. Furthermore, the drying rate of thin films is much faster because of the higher surface/volume ratio and the effect of solvent drainage by the porous support. The rate of drying can affect the structure of the sol since longer drying times provides more time for the sol to condense into a more regular mesostructure.

At a cyclohexane pressure equal to zero, M10 was more permeable to oxygen than M02 (Figure 7.5a). Nevertheless, oxygen permeated through the membrane already at a relative pressure of about 0.75, which corresponds to pores with a Kelvin radius of about 8 nm. This observation is in agreement with what was measured by nitrogen sorption on P10, a measurement in which pores larger than in the other samples were observed. S10 yielded more permeable membranes, but these are less selective in processes in which particles/molecules with sizes below 10 nm are involved.

Gas permeation

In Chapter 2 different transport mechanism were described. As a general rule the flow of a gas permeating through macroporous media can be described in terms of viscous flow. Knudsen diffusion is typical for transport of gases in mesopores, and for micropores the transport rate is generally described in terms of activated transport [42]. We suppose that Knudsen transport is dominant in our material; indeed the sorption data in Table 3.2 show that the prepared materials are mesoporous.

From Equation 2.9 it follows that in mesoporous regime the permeance is proportionally inverse to the square root of the gas molecular mass. In the system under consideration here, a mesoporous thin film is supported by a macroporous α-alumina support. Permselectivities below the Knudsen limit indicates a defective mesoporous layer, i.e., a membrane with a significant contribution of non-selective viscous flow on the overall rate of molecular transport. Therefore, gas permeation measurements not only give a direct indication of the performance of a membrane in terms of flux and selectivity,

but may also provide a proof of either the presence or absence of macroscopic defects in the silica layer. As reported in Figure 7.6, Knudsen-type selectivity was observed for M02 and M06. This means that all support macropores are filled or covered with a templated silica layer, and the layer does not have measurable defects.

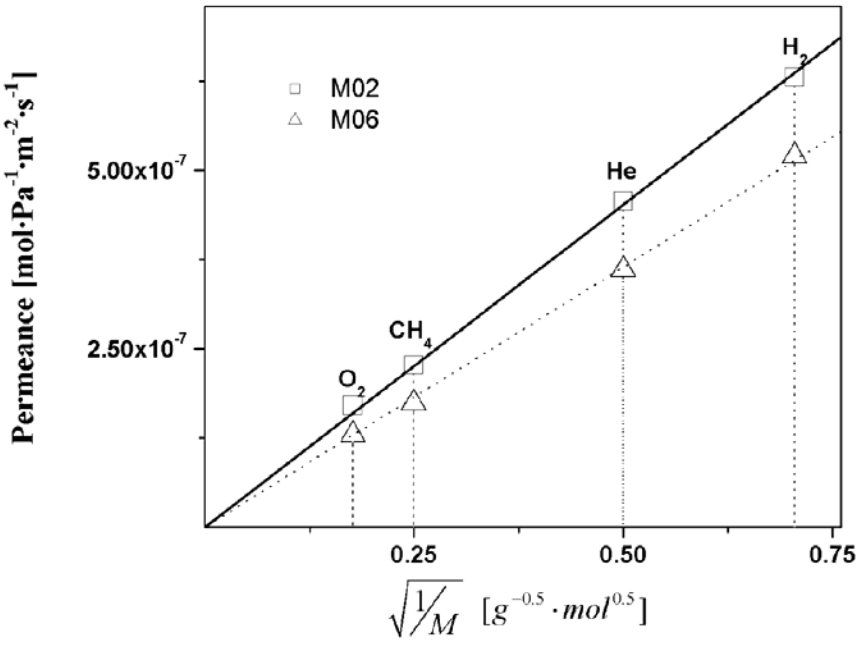

Figure 7.6. Single gas permeance of templated silica membranes M02 and M06 as function of the molecular mass of the probe molecules. The Knudsen behavior of M02 and M06 is stressed respectively by a continuous line and a dotted line.

A "defect free" templated silica membrane can be defined as a film with the selectivity of a mesoporous layer. This definition is often used in membrane technology in cases in which membrane selectivity is more important than the intrinsic structural quality of the separating layer. Gas permeation and permporometry, which are methods based on the measurement of membrane performance, have been used as a proof for the absence of defects in the top-layer. This is certainly true for mesoporous layers obtained by deposition of colloidal sols, where penetration is negligible and membrane performance is determined by the quality of the top layer. On the other hand, in the case of

membranes obtained by polymeric sols the penetrated material also plays a role. The most representative case is membrane M02: although Knudsen separation was observed for this membrane and its pore size distribution was in the mesoporous range, Figure 7.4a clearly demonstrates that a top layer that is as such recognizable is completely absent. Hence, gas permeation measurements are not an exhaustive proof of the existence of a continuous porous film obtained from a polymeric sol. The high resistance to gas transport of M06 suggests a comparable degree of penetration of silica into the α-alumina support. In the case of M06 some degree of penetration is visible in Figure 7.4c. BYK-420 is an effective additive in order to obtain silica membrane on a macroporous α-alumina. Nevertheless it is not possible with this method to avoid penetration in the support completely. In Figure 7.4c silica on the α-alumina grains is still visible in a region deeper than 1 μm.

The permeance values reported in Figure 7.6 are higher than those obtained by Nishiyama et al. [25] with membranes that had been prepared by hydrothermal treatment on commercial alumina plates (NGK Insulators, Ltd). The hydrogen permanence of those membranes was about $2.7 \cdot 10^{-7}$ mol·Pa^{-1}·m^{-2}·s^{-1} at 295 K, while that of the asymmetric supports was $1.1 \cdot 10^{-4}$ mol·Pa^{-1}·m^{-2}·s^{-1} at a temperature of 295 K and an overpressure of 2.7 bar. These commercial substrates had on the top a pore size of about 0.1 μm, which is similar to that of the home-made supports utilized by us. The supports that we used were prepared by colloidal filtration from a suspension of alumina powder in water. Commercial supports are usually asymmetric systems with smaller pores located on the side where the coating is deposited, and pores of a few microns width on the opposite side. Commercial supports have gas resistances smaller than 10^5 Pa·m^2·s·mol^{-1} (expressed as the reciprocal of permeance), but often a high number of defects is present on their surface. The symmetric supports prepared by us have a ten times larger resistance. On the other hand their surface is very well defined. The roughness depends only on the alumina grains, which have dimensions of a few hundred nanometers. Defects like scratches or holes are not detectable by optical

analysis. For this reason we chose them as support for lab testing and preliminary studies. The next step of this research is to test this procedure on commercial tubular supports, which will eventually yield membranes with enhanced permeances.

7.4. Conclusions

Templated silica membranes were successfully prepared by direct coating of a thixotropic polymeric sol onto a macroporous support. BYK-420 was able to confer a thixotropic behaviour to the sol at relatively low concentrations. As result the penetration of the sol into the support during the coating procedure was strongly inhibited. Doubly coated membranes showed no indications of defects and pores larger than 5 nm were not detected, while the main pore width was about 1.8 nm. Membranes with such pore size distribution can be applied in many industrially relevant processes directly as molecular sieves, or as support for microporous silica or Nb-doped silica. Moreover they can be used in nanofiltration, for instance, to separate homogenous catalysts [43] or drugs [44,45] from their reaction mixtures.

7.5. References

[1] S. Mann, S.L. Burkett, S.A. Davis, C.E. Flower, N.H. Medelson, S. D. Sims, D.W. Walsh, N.T. Whilton, Chem. Mater. 9 (1997) 2300.

[2] V.V. Guliants, M.A. Carreon, Y.S. Lin, J. Memb. Sci. 235 (2004) 53.

[3] N.K. Raman, M.T. Anderson, C.J. Brinker, Chem. Mater. 8 (1996) 1682.

[4] I. Honma, H.S. Zhou, D. Kundu, A. Endo, Adv. Mater. 12 (2000) 1529.

[5] C.T. Kresge, M.E. Leonowicz, W.J. Roth, J.C. Vartulli, J.S. Beck, Nature 359 (1992) 710.

[6] J.S. Beck, J.C. Vartulli, W.J. Roth, M.E. Leonowicz, C.T. Kresge, K.D. Schmitt, C.T.W. Chu, D.U. Olson, E.W. Sheppard, S.B. McCullen, J.B. Higgins, J.L. Schlenker, J. Am. Chem. Soc. 114 (1992) 10834.

[7] H. Yang, N. Coombs, I. Sokolova G. A. Ozin, J. Mater. Chem. 7 (1997) 1285.

[8] D.M. Antonelli, J.Y. Ying, Curr. Opin. Colloid Interface Sci. 1 (1996) 523

[9] M. Mulder, Basic principles of membrane technology (2nd edition), Kluwer Academic Publisher, Dordrecht, 1996.

[10] L.G.A. van de Watera, T. Maschmeyera, Top. Catal. 29 (2004) 67.

[11] C-Y Tsai, S-Y Tam, Y Lu, C. J. Brinker, J. Membr. Sci. 169 (2000) 255.

[12] S.R. Chowdhury, R. Schmuhl, K. Keizer, J.E. ten Elshof, D.H.A. Blank, J. Memb. Sci. 225 (2003) 177.

[13] S.R. Chowdhury, K. Keizer, J.E. ten Elshof, D.H.A. Blank, Langmuir 11 (2004) 4548.

[14] L. Huang, S. Kawi, K. Hidajat, S.C. Ng, Micropor. Mesopor. Mater. 88 (2006) 254.

[15] M. Ogawa, J. Am. Chem. Soc 116 (1994) 7941.

[16] P.T. Tanev, T.J. Pinnavia, Chem. Mater. 8 (1996) 2068.

[17] J.M. Kim, S.K. Kim, R. Ryoo, Chem. Comm. 2 (1998) 259.

[18] A.C. Pierre, Introduction to Sol-Gel Processing, Kluwer Academic Publisher, Dordrecht., 1998.

[19] A.J. Burggraaf, L. Cot., Fundamentals of Inorganic Membrane Science and Technology, Elsevier, Amsterdam, 1996, p. 294.

[20] A.F.M. Leenaars, K. Keizer, A.J. Burggraaf, .J. Mater. Sci. 19 (1984) 1077.

[21] J. Sekulic, A. Magraso, J.E. ten Elshof, D.H.A. Blank, Micropor. Mesopor. Mater. 79 (2004) 49.

[22] X.S. Ju, P. Huang, N.P. Xu, J. Shi, J. Memb. Sci. 166 (2000) 41.

[23] B.N. Nair, J.W. Elferink, K. Keizer, H. Verweij, J. Sol-Gel Sci. Technol. 8 (1997) 471.

[24] S.R. Chowdhury , A.M. Peters, D.H.A. Blank, J.E. ten Elshof , J. Memb. Sci. 279 (2006) 276.

[25] N. Nishiyama, D. Huy Park, A. Koide, Y. Egashira, K. Ueyama, J. Memb. Sci. 182 (2001) 235.

[26] D.H. Park, N. Nishiyama, Y. Egashira, K. Ueyama, Micropor. Mesopor. Mater., 66 (2003) 69.

[27] N. Nishiyama, H. Saputra, D. Huy Park, Y. Egashira, K. Ueyama, J.

Memb. Sci. 218 (2003) 165.

[28] C. Boissiere , M.U. Martines ,A. Larbot, E. Prouzet, J. Memb. Sci., 251 (2005) 17.

[29] G.-Z. Cao, J. Meijerink, H.W. Brinkman, A.J. Burggraaf, J. Memb. Sci., 85 (1993) 221.

[30] G.-Z. Cao, H.W. Brinkman, J. Meijerink, K.J. de Vries, A.J. Burggraaf, J. Am. Ceram. Soc. 76 (1993) 2201.

[31] R.M. de Vos, H. Verweij, J. Memb. Sci., 143 (1998) 37.

[32] Handbook of Chemistry and Physics (55th Edition), CRC Press, Cleveland, Ohio.

[33] M.T. Anderson, J.E. Martin, J.G. Odinek, P.P. Newcomer, Chem. Mater.10 (1998) 311.

[34] Y. Di, X. Meng, S.G. Li, F.S. Xiao, Micropor. Mesopor. Mater. 82 (2005) 121.

[35] C. Boissiere, M.A.U. Martines, M. Tokumoto, A. Larbot, E. Prouzet, Chem. Mater. 15 (2003) 509.

[36] Anderson MT, Martin JE, Odinek JG, Newcomer PP, Chem. Mater. 10 (1998), 1490.

[37] J.L. Blin, C. Otjacques, G. Herrier, and B.-L. Su, Langmuir 16 (2000) 4229.

[38] Miyata, H.; Kuroda, K. J. Am. Chem. Soc. 121 (1999) 7618.

[39] R. Bandyopadhyaya, E Nativ-Roth, R. Yerushalmi-Rozen, O. Regev, Chem. Mater. 15 (2003) 3619.

[40] R.R. Bhave, Inorganic Membranes: Synthesis, Characteristics and Applications, Van Nostrand Reinhold, New York, 1991, p.158.

[41] This thesis, Chapter 2, p.

[42] N. Nishiyama, D.H. Park, Y. Egashira, K. Ueyama, Sep. Purif. Technol. 32 (2003) 127.

[43] P.T. Witte, S. Roy Chowdhury, J.E. ten Elshof, D. Sloboda-Rozner, R. Neumann, P.L. Alsters, Chem. Commun. (2005) 1206.

[44] D.L. Oatley, B. Cassey, P. Jones, W.R. Bowen, Chem Eng. Sci.60 (2005) 1953.

[45] W.R. Bowen, B. Casseyb, P. Jonesc, D.L. Oatleya, J. Membr. Sci. 242 (2004) 211.

CHAPTER 8

Hydrothermal stability of mesoporous layers

Abstract

Mesoporous templated silica has a lower hydrothermal stability than La-doped γ-alumina and no higher stability than γ-alumina. The hydrothermal stability of templated silica was therefore improved by doping the material with zirconium ions. Doping was performed by adding Zr acetylacetonate to a silica sol. Samples were prepared with Zr : Si molar ratios equal to 0, 0.017, 0.034 and 0.081, respectively. In all samples the (Si+Zr)/surfactant ratio was kept constant. Samples with Zr : Si up to 0.034 had a BET surface area larger than 1000 $m^2 \cdot g^{-1}$, which is comparable to the surface area of pure templated silica. The sample with Zr : Si = 0.081 had a surface area of 940 $m^2 \cdot g^{-1}$. XRD analysis showed a broad peak between 2θ 2-3° in all samples. This was attributed to the presence of long range order in the pore structure of the material. By increasing the zirconium loading, the peak gradually shifted to smaller angles. The thickness of the pore walls was found to increase upon Zr doping.

BET analysis of samples after exposure to 0.56 bar of steam at 300 °C for 1000-2000 min showed that the doped samples were more stable than the undoped one. After the second hydrothermal treatment at 300 °C, the reduction of surface area was about 15% for the Zr-doped materials, while it was 27% for undoped silica. Hence, Zr-doping significantly increased the hydrothermal stability of the material. A Zr:Si molar ratio of 0.017-0.034 appears to be optimal to prepare hydrothermally stable and highly porous templated silica membranes.

8.1. Introduction

Templated silica thin films need to be stable under conditions at which separation is performed, regardless of whether they are used as interlayer in the preparation of supported gas sieves, or applied directly as selective membrane layers. Hydrothermal stability and, in general, chemical stability are important aspects of many mesoporous materials. For instance, γ-alumina is an easy to process material, but it has a poor stability under hydrothermal conditions and at low pH. In recent years a lot of research efforts were focused on the development of mesoporous membranes from materials other than γ-alumina. Indeed doped γ-alumina [1,2], titania [3-5] and zirconia [3,6] mesoporous membranes have been prepared and their chemical and hydrothermal stability was shown to be higher than that of γ-alumina.

Titania and zirconia membranes are stable in a large range of pH, but they are not stable at temperatures above 450 and 600 °C, respectively, due to the occurrence of kinetically hindered phase transitions, which have relevant rates at these temperatures. La-doped γ-alumina is hydrothermally more stable than pure γ-alumina and membranes thereof can be prepared more easily than from titania or zirconia. For this reason, this material was selected for use in the mesoporous interlayer of supported membranes in Chapter 3-6. However, when this material is exposed to particularly harsh conditions, such as in simulated ambient steam reforming atmosphere (SASRA), important structural changes were observed in its porous structure [1].

It is well known that templated silica is not so stable in hydrothermal conditions and that the ordered mesoporous structure has a tendency to collapse already when treated in boiling water for 12 h [7]. It has already been reported that the hydrothermal stability of templated silica can be improved by zirconia doping [8,9]. Powders with different ZrO_2 loadings were obtained by adding Zr-acetylacetonate to sols prepared as described in section 7.2. This precursor was chosen because it is not hydrated and is stable in the sol mixture, so that it is not reacting with silica before the coating; although this precursor was not well soluble in the silica sol. After calcination the

hydrothermal stability of the bulk materials were analyzed by nitrogen sorption and compared with the stability of undoped material. To illustrate the potential of Zr-doped mesoporous silica as a replacement of γ-alumina for separation under hydrothermal conditions, a parallel study was carried out on pure and doped γ-alumina and mesoporous silica.

8.2. Stability of mesoporous layers: a permporometry study

Figure 8.1 depicts the gradual modification of templated silica, γ–alumina and 6% doped γ–alumina membranes as monitored by permporometry [10,11] analysis. The pore size distribution of these three membranes was measured by permporometry on both fresh samples, and on samples after exposure to 0.56 bar of steam at varying temperatures. Following each treatment the membranes were dried at 100 °C in vacuum for one day, and they were then characterized by permporometry.

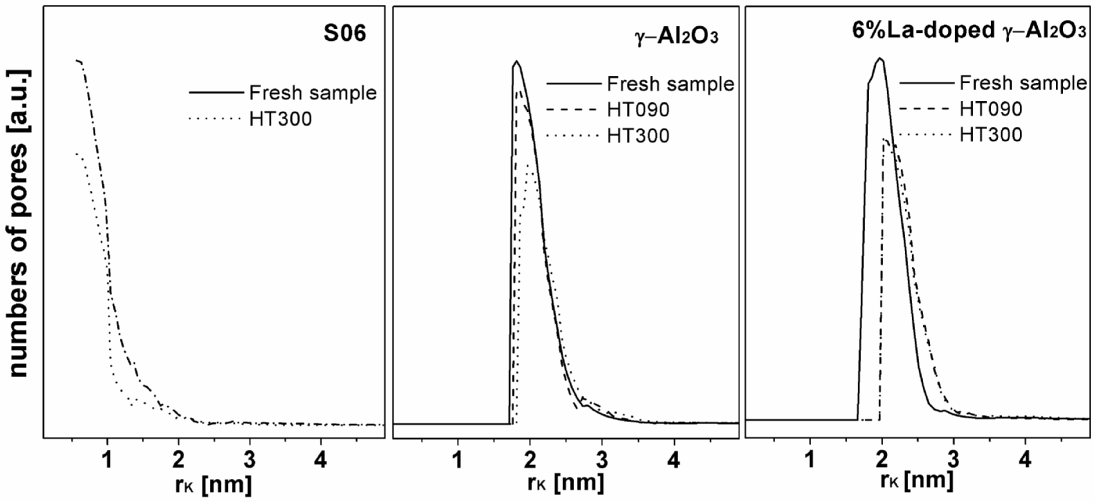

Figure 8.1. Hydrothermal modification of pore size distributions of S06, γ-alumina and 6% La-doped γ-alumina membranes, as measured by permporometry. The instrument measured the oxygen permeance as function of cyclohexane relative pressure, while nitrogen was used as sweep gas. The samples were treated at 90 °C (HT090) and then at 300 °C (HT300) for 1000 minutes. For the sake of comparison the maxima of the distributions of the fresh samples of all three materials, were normalized to the same value.

The preparation of S06 was described in the previous chapter. The γ-alumina

membranes were prepared by dip coating of sols as described on page 24. According to the permporometry analysis, S06 has narrower pores than the mesoporous alumina membranes. The γ-Al_2O_3 membrane had pores with Kelvin diameter (r_k) between 1.7 and 4 nm. Pores with r_k wider than 4 nm were also detected, but their population was less than 1% of the total number of pores. The 6% La-doped γ-alumina membrane had a slightly broader pore size distribution than the undoped sample.

Both the alumina membranes underwent modification after the first exposure to steam at 90 °C. In both cases, modification resulted in a reduction of the number of smaller pores and a small increase of the fraction of largest pores. As was already illustrated in Chapter 6, hydrothermal densification is comparable to a sintering process, in which small pores, which have higher degree of curvature, are closed while wider pores are enlarged [12]. The structural modification appeared to be more prominent in the 6 at% La-doped γ-alumina membrane than in the pure γ-alumina membrane. However, after the first exposure the pore size distribution of the 6 at% La-doped γ-alumina remained unchanged upon treatment at 300 °C, while for the undoped γ-alumina membrane the number of pores with Kelvin diameter (r_k) smaller than 2 nm decreased further with each treatment, and the number of pores with r_k larger than 3 nm increased. Despite the fact that no long-term exposure measurements were done, these data indicate that 6 at% La-doped γ-alumina may be a hydrothermally stable interlayer material for gas selective membranes. However, calcination in steam or hydrothermal pretreatment is desirable to fabricate a product that does not change its properties once it is operating in hydrothermal conditions.

Sample S06 showed rather poor hydrothermal stability like γ-alumina. After hydrothermal treatment the concentration of all pores had decreased. The phenomenon was particularly significant for the smallest pores with the highest degree of curvature. Since the permporometry set-up used here is suited to measure mesoporous layers, the analysis of templated silica is rather complicated, due to the fact that a large number of micropores is present in

this material. The maximum of the distribution was centered at r_k = 0.6 nm, since the set-up does not allow measurement of smaller pores. The height of the maximum was reduced by about 25% after hydrothermal treatment at 300 °C. Probably the ultramicropores present in the material underwent even more densification than the detectable pores shown in Figure 8.1. The experiment showed that the hydrothermal stability decreases in the order 6 at% La-doped γ-alumina > γ-alumina , S06.

The fact that templated silica has a hydrothermal stability equal to or lower than γ-alumina implies that its stability requires improvement before it can be applied in molecular separations in the presence of steam. It was chosen to improve the hydrothermal stability of mesoporous templated silica by doping the material with zirconium ions, and to study the influence of doping on microstructure by N_2 sorption experiments on powders, in order to obtain the most detailed information about changes of pore shape and size distribution.

8.3. Experimental

Sample preparation

The conformation of the porous structure of MCM materials depends on the type of micelles that the surfactant forms when the sol transforms into the consolidated state. CTAB (cetyltrimethylammonium bromide) can form different liquid crystals depending on temperature and concentration. Hence, a variation in the metal/CTAB ratio can cause large differences in the alignment and interconnectivity of the templated pore channels in the resulting solid material. For this reason this ratio was kept constant in samples prepared with different Zr loadings. For the sake of simplicity all powdered samples will be designated according to the abbreviations listed in Table 8.1.

Sample S00 is the undoped silica sol described in Chapter 7. It is therefore designated here using the same abbreviation. Samples Z1 and Z2 were prepared with CTAB : Zr ratios of 8 and 4, respectively. These ratios were chosen because literature suggests that CTAB has a preferential interaction

with zirconium compared to silicon [13]. As a consequence the introduction of zirconium in the sol may result in a preferential pore surface coating, rather than in structural doping of the silica bulk. Z3 contains the highest concentration of Zr ions of the sols reported here. At the concentration used for Z3, the Zr acetylacetonate was not completely soluble in the mixture. The final Z3 sol was not completely transparent.

γ-Alumina samples were prepared as described in Chapter 2, on page 23. The 6 at% La-doped powder was prepared by adding a proper amount of lanthanum nitrate hexahydrate (99.99% Aldrich) to the coating solution just before coating the membrane or drying the sol to prepare the powdered samples.

Table 8.1. Composition of silica and Zr-doped silica sols used in the preparation of samples presented in this chapter.

Sample	TEOS	$Zr(acac)_4$	CTAB	0.05M HNO_3	1-propanol
S00	16.0 ml (72.0 mmol)	-	3.5 g (9.6 mmol)	20 ml	80 ml
Z1	15.8 ml (70.8 mmol)	0.59 g (1.2 mmol)	3.5 g (9.6 mmol)	20 ml	80 ml
Z2	15.4 ml (69.6 mmol)	1.18 g (2.4 mmol)	3.5 g (9.6 mmol)	20 ml	80 ml
Z3	15.8 ml (66.6 mmol)	2.62 g (5.4 mmol)	3.5 g (9.6 mmol)	20 ml	80 ml

Silica sols were synthesized as follows: a mixture containing tetraethylorthosilicate (TEOS, 98% Aldrich) and 1-propanol was prepared under inert atmosphere to avoid hydrolysis of the silica precursor. 20 ml of 0.05 M HNO_3 in water was added to the solution under vigorous stirring. After adding 3.5 g CTAB (99%, Aldrich) the mixture was heated for 2 h at boiling temperature under reflux. After that a variable amount of zirconium acetylacetonate (98%, Aldrich) was added. Then the mixture was stirred for 10 min, poured in a Petri dish and dried in air. The resulting powders were calcined at 500 °C. Zirconium acetylacetonate was not well soluble in the

reaction solution, and the final Z2 and Z3 sols were not completely transparent. Z3 was also rather viscous compared to the other sols.

Hydrothermal treatment

Hydrothermal treatment was carried out in a tubular furnace in a quartz glass cell. The samples were exposed to a moisture-containing air flow of about 10 ml/min at atmospheric pressure. Steam was introduced in the air feed by bubbling air in a water bath that was kept at a temperature of 85 °C. This generated a water vapor partial pressure of 0.56 bar.

Characterization

X-Ray Diffraction (XRD) patterns were recorded using a Philips SR5056 with Cu Kα radiation. In all measurements at low angles, the zero point was centered by moving the sample vertically until the diffracted total intensity was about half of the direct beam intensity.
BET measurements were performed at 77 K on a Micromiretics ASAP 2400. Permporometry profiles were obtained using the same set-up as for the determination of pore size distributions of membranes in the previous chapter.
X-ray Photoelectron Spectroscopy (XPS) measurements were carried out on a PHI Quantera Scanning ESCA Microprobe with a monochromatic AlKα X-ray source (1486.6 eV) at pressures below $8 \cdot 10^{-6}$ bar.

8.4. Results and discussion

Morphology of Zr-doped silica samples

The structural modification of the material as consequence of the introduction of Zr^{4+} ions in the silica framework was investigated by XRD and nitrogen sorption as shown in Figure 8.2, Table 8.2, and Table 8.3. The XRD pattern of S00 was compared with the patterns of Z1, Z2 and Z3 in Figure 8.2. The bulk material was x-ray amorphous, independent of the Zr loading. Long-range

order in S00 was demonstrated by the presence of a peak at 2.7° 2θ, as shown in Figure 7.2. The associated *d*-spacing is normally considered to indicate the distance between the centers of two adjacent pores [14]. By increasing the zirconium loading, the peak gradually shifted down to 2.2° 2θ in Z3. The shift to lower 2θ values implies that the distance between the centers of two neighboring pores is enlarged. This can be ascribed either to larger templated pores [15], or to the fact that the pore walls become thicker upon introduction of Zr ions in the material. In Table 8.3 the surface area and pore volume of the four samples are listed as calculated from the BET method. The average pore size was not reported, indeed it was calculated to be 1.8 nm for S00 and 1.82 nm for the Zr-doped samples, so the difference was presumably within the experimental error of the measurement and method. Due to the relatively large number of micropores present in these materials, the errors were relatively large.

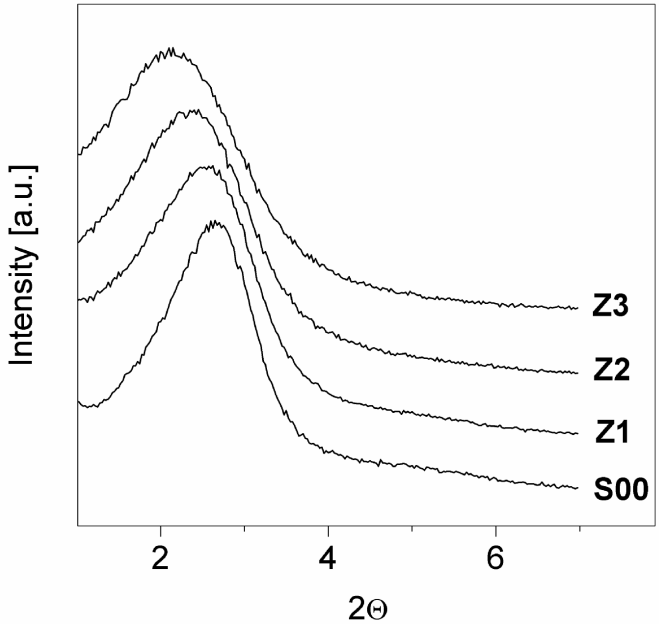

Figure 8.2. Low angle XRD patterns of pure and Zr-doped silica samples.

Table 8.2. Parameters of the low angle peak of silica and Zr-doped silica samples.

sample	max. [2θ]	width [2θ]
S00	2.7°	1.0°
Z1	2.6°	1.0°
Z2	2.4°	1.4°
Z3	2.2°	1.6°

The fact that Z3 has a smaller surface area than S00, while these two materials have similar pore sizes, suggests that the change in *d*-spacing

observed by XRD analysis does not correspond to an enlargement of the pores in Z3, but rather to an increasing thickness of the pore walls. For this reason, we may assume that the incorporation of zirconium ions in Z3 occurred both in the bulk and on the pore surface. Information on the degree of long range order within the material can be acquired by analysis of the broadening of XRD peaks. Because the peaks were asymmetric due to disturbance of the primary beam at small 2θ, the full width at half maximum intensity (FWHM) [16] was calculated by doubling the width of the right side of the peak. As listed in Table 8.2, the XRD peak width increased gradually from 1.0° for S00 to 1.6° 2θ for Z3. This is an indication that Zr-doping reduced the degree of long range order in the material.

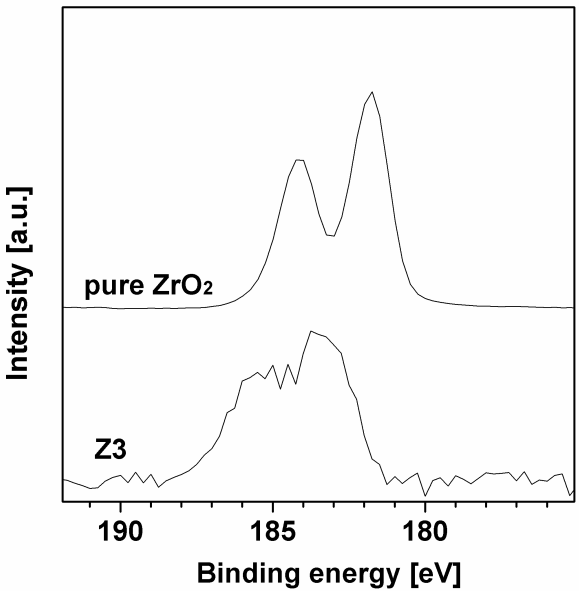

Figure 8.3. XPS spectrum of S00 and Z3. showing binding energy region of Zr 3*d*.

In Figure 8.3 the binding energy of the 3*d* state of zirconium in Z3 is compared with a reference sample consisting of pure zirconia powder (TZ-8YS, Tosoh, Japan). The variation in binding energy of about 2 eV is an indication that the zirconium atoms have different chemical surroundings in the two samples. This suggests that Zr was homogeneously incorporated into the silica framework, without forming any zirconia domains. The fact that all Zr-doped samples were x-ray amorphous is in agreement with these findings.

Stability in hydrothermal conditions: time effect.

Table 8.3 lists the BET surface area (S_{BET}), pore volume (V_p) and pore width D_{BJH} (calculated according the BJH model) of powders after treatment in air in the presence of 0.57 bar of steam at 300 °C for 1000 and 2000 min, respectively. From the data shown in Table 8.3 it can be seen that the stability

of 6 at%-La doped γ-alumina is higher than that of pure γ-alumina. Before treatment the surface area of the undoped sample was 274 m^2/g and the area

Table 8.3. BET surface area S_{BET}, pore volume V_p and pore diameter D_p at 300 °C as function of hydrothermal exposure time. The percentages between brackets indicate values relative to that of the fresh sample.

Sample	Treatment time [min.]	S_{BET} [$m^2 \cdot g^{-1}$]	V_p [$cm^3 \cdot g^{-1}$]	D_{BJH} [nm]
Al_2O_3	0	274	0.39	5.6
	1000	243 (88.7%)	0.35 (89.7%)	5.9
	2000			5.0
6%La-doped Al_2O_3	0	224	0.32	5.7
	1000	242 (107%)	0.32 (100%)	5.2
	2000			5.2
S00	0	1379	0.61	
	1000	1070 (77.5%)	0.48 (78.7%)	
	2000	1006 (72.9%)	0.45 (73.8%)	
Z1	0	1408	0.61	
	1000	1240 (88.1%)	0.55 (90.2%)	
	2000	1188 (84.4%)	0.53 (86.9%)	
Z2	0	1254	0.54	
	1000	1136 (90.6%)	0.50 (92.6%)	
	2000	1056 (84.2%)	0.46 (85.2%)	
Z3	0	939	0.43	
	1000	876 (93.3%)	0.40 (93.0%)	
	2000	811 (86.4%)	0.38 (88.4%)	

of the doped sample was 224 m^2/g. After the first exposure to steam, the pore volume and surface area of the undoped γ-alumina decreased by about 10%, while the pore volume of 6 at%-La doped γ-alumina remained unchanged upon

steam exposure and only the surface area increased slightly.

Since the main effect of steam exposure is the densification of silica, the increment of surface area was not expected. Despite the fact that fresh Al_2O_3 initially had a larger surface area and a larger pore volume than the doped sample, they showed similar parameters after the second treatment at 300 °C. This is an indication that La-doped γ-Al_2O_3 has a higher hydrothermal stability than pure γ-Al_2O_3. It is possible that longer aging times in steam at 300 °C will result in doped samples with larger pore volumes and larger surface areas than the pure γ-alumina sample. Table 8.3 also illustrates the positive effect of Zr-doping on the hydrothermal stability of the templated silica mesophase. The numbers between brackets indicate the degree with which the surface area and pore volume vary as a consequence of hydrothermal exposure. As can be seen from the table, the degree of variation became less pronounced with increasing Zr loading. After the second treatment, the decrease of surface area was about 30% for S00 and less than 15 % for Z3. All three Zr-doped silica samples showed higher structural stability than S00, and after the second treatment at 300 °C the reduction of surface area and pore volume (relative to the fresh sample) was similar for Z1, Z2 and Z3. However, the surface area and pore volume of Z3 were smaller than the other samples already after calcination in air. After hydrothermal exposure its pore volume was only 0.38 cm^3/g, smaller than any of the other silica powders and comparable to γ-alumina. For this reason, Zr loadings in the range between Z1 and Z2 seem to be optimal levels.

Zr-doped silica appears to be a material with sufficient stability for application in processes such as water-gas-shift reaction. However, it turned out to be very difficult to prepare mesoporous Zr-doped silica layers on macroporous supports. Attempts to deposit Zr-doped silica films on flat α-alumina discs, following the procedure described in the previous chapter, mainly failed due to the incompatibility of the Zr-doped silica sols and the rheology modifier BYK-420. Addition of the rheological additive to Zr-doped silica sols resulted in a gelly precipitate in the solution.

Thin layers were fabricated by dip-coating the Z2 sol directly on α-alumina discs. The Z2 sol was filtered and the dip-coating procedure performed as described in the previous chapters. After drying, extensive microcracking occurred, which ultimately led to complete delamination from the support.

8.5. Conclusions

The stability of templated silica was improved by the introduction of a small amount of Zr ions in its framework. Nevertheless there is an upper limit to the amount that can be introduced; high levels of dopant yielded a material that was denser and thus less suitable for application as a membrane. In all the analyzed samples the hydrothermal modification was found to be more pronounced during the first treatment than during the second one, similar to what was observed on a microporous membrane in Chapter 6. It is reasonable to assume that some of the oxygen-metal bonds formed during calcination at 500-600 °C had a less favourable conformation, e.g., because of strained bond angles. Especially these locations in the structure are prone to degradation by steam, and will be the first to be broken upon hydrothermal exposure.

8.6. References

[1] A. Nijmeijer, H. Kruidhof, R. Bredesen, H. Verweij, J. Am. Ceram. Soc. 84 (2001) 136.

[2] Md.H. Zahir, K. Sato, H. Mori, Y. Iwamoto, J. Am. Ceram. Soc. 89 (2006) 2874.

[3] C.-H. Chang, R. Gopalan, Y.S. Lin, J. Membrane Sci. 91 (1994) 27.

[4] J. Sekulic, A. Magrasso J.E. ten Elshof, D.H.A. Blank, Micropor. Mesopor. Mater. 2004, 72, 49.

[5] T. Van Gestel, C. Vandecasteele, A. Buekenhoudt, C. Dotremont, J. Luyten, R. Leysen, B. Van Der Bruggen, G. Maes, J. Membrane Sci. 207 (2002) 73.

[6] T. Van Gestel, H. Kruidhof, D.H.A. Blank, H.J.M. Bouwmeester, J.

Membrane Sci. 284 (2006) 128.

[7] M Kruk, M Jaroniec , A Sayari, Micropor. Mesopor. Mater., 27 (1999) 217.

[8] M. Selvaraj, P.K. Sinha, K. Lee, I. Ahn, A. Pandurangan, T.G. Lee, Micropor. Mesopor. Mater. 78 (2005) 139.

[9] J.M. Liu, S.J. Liao, G.D. Jiang , X.L. Zhang, L. Petrik, Micropor. Mesopor. Mater. 95 (2006) 306.

[10] G.-Z. Cao, J. Meijerink, H.W. Brinkman, A.J. Burggraaf, J. Membrane Sci., 85 (1993) 221.

[11] G.-Z. Cao, H.W. Brinkman, J. Meijerink, K.J. de Vries, A.J. Burggraaf, J. Am. Ceram. Soc. 76 (1993) 2201.

[12] R. Leboda, E. Mendyk, Mater. Chem. Phys. 27 (1991) 189.

[13] M.S. Wong, H.C. Huang J.Y. Ying, Chem. Mater. 14 (2002) 1961.

[14] J.E. Martin M.T. Anderson, J. Odinek, P. Newcomer, Langmuir 13 (1997) 4133.

[15] V. Boffa, J.E. ten Elshof and D.H.A. Blank, Micropor. Mesopor. Mater. 100 (2007) 173.

[16] C. Hammond, The Basics of Crystallography and Diffraction, Oxford, New York, p. 147.

CHAPTER 9

Microsieve-supported ultrathin membranes

Abstract

A method for preparing self-standing 100-200 nm thick mesoporous silica membranes. Mechanical strength is provided by silicon nitride-based microsieve supports with circular perforation of 0.5-1.2 μm diameter and depth ~1 μm dept. The application of the film as a gateable interconnect for microfluidic device technology is demonstrated. The presence of a small number of microdefects defect do not allow applying these layer as gas-selective membranes, yet.

9.1. Introduction

The stacked layer architecture of the membrane described in this thesis allow preparing supported defect-free membranes which have a thickness of about 30 nm and can stand several bars of pressure. However, the support, which is several millimeters thick, often has a non-negligible resistance to gas flow. This resistance is of the same order of magnitude as that of the selective top layer. For instance, in the pure silica membrane shown in Chapter 6, the resistance of the silica top layer to hydrogen flow was comparable to the resistance of the γ-alumina/α-alumina support. Hence the resistance of the support to gas flow sets an intrinsic upper limit to the permeability of membranes. Moreover, these macroporous supports are usually made of α-alumina. These supports cannot be fabricated easily with a lower than 10^{-4} m^2 membrane area. Their application is therefore impossible in the emerging lab-on-a-chip technologies, where they could find good use in principle.

For this reason membranes were prepared by depositing a ceramic film on silicon nitride microsieves. These sieves have an extremely low resistance to fluid flow, because of the high density of perforations and the thickness of only 1 μm [1]. Schmuhl et al. deposited a MCM-48 layer by spin coating, yielding a silica film which covered the entire sieve [2,3]. The final thickness of the membrane was ~1 μm, similar to that of the microsieve.

The aim of this study was to develop a methodology to deposit thin silica films on top of the perforated microsieves, without any penetration of silica into the perforations of the support. This should result in a substantial reduction of layer thickness. We employed a sacrificial layer approach [4] to accomplish this. Mesostructured silica was chosen as model material, but the same strategy should also be possible with other materials.

These porous films deposited on silicon nitride perforated chips, may be used for molecular separation but could also lead to enabling microchip-based technologies for separation, detection and dosing [4-9]. The so-prepared mesoporous silica membranes were tested in two different setups. They were

tested in single-gas permeation experiments of the type depicted in Chapter 7. Their possible utilization in microfluidic devices was investigated by model experiments proposed earlier by Schmuhl et al. [2].

9.2. Membrane preparation

Materials

The silica sol was synthesized by hydrolysis of tetraethyl-orthosilicate (≥99%, Aldrich) with 1-propanol in an acid medium, to which nitric acid (ca. 65% solution in water, Acros) and the templating agent cetyltrimethylammonium bromide (CTAB, ≥99% purity, Aldrich) were added, as described in Chapter 7 and elsewhere [10]. The microsieves (Aquamarijn Micro Filtration B.V.) had a functional surface area of 5 mm^2 and circular perforations of 500 nm diameter in hexagonal setting.

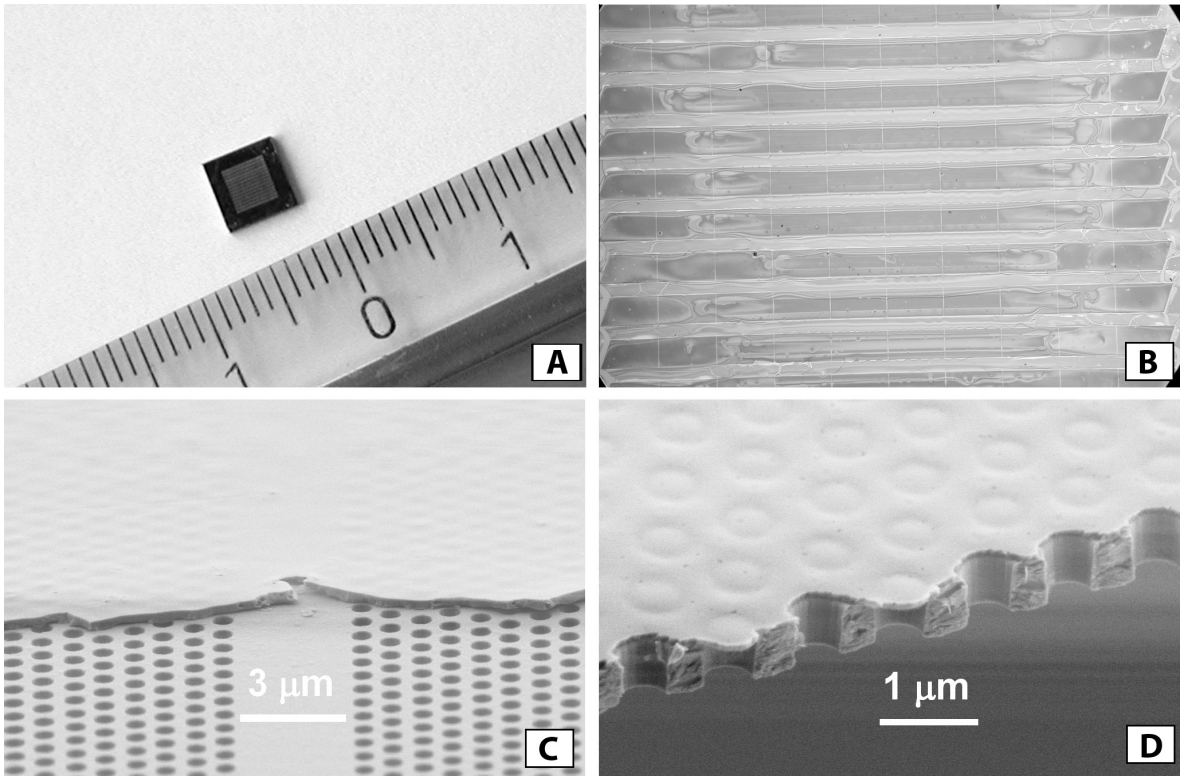

Figure 9.1 Images of the microsieve. (A) Picture of the microsieve. (B) Optical microscope image of the microsieve with the silica membrane after calcination. (C) SEM image of the microsieve with a self-standing silica membrane after the calcination. (D) SEM image of the self-standing silica membrane do not plugged into the pores, high magnification.

A picture of a sieve is shown in Figure 9.1a. The perforations are located in the orange areas in the optical microscope picture in Figure 9.1b. A SEM magnification of these perforations is shown in Figure 9.1c, in the part of the sieve which is not covered by the silica membrane.

Film deposition

The process developed for the formation and transfer of a silica film onto a perforated microsieve is shown schematically in Figure 9.2. In the first step, the perforations of the sieve were filled to avoid penetration of the silica sol in the subsequent film deposition step.

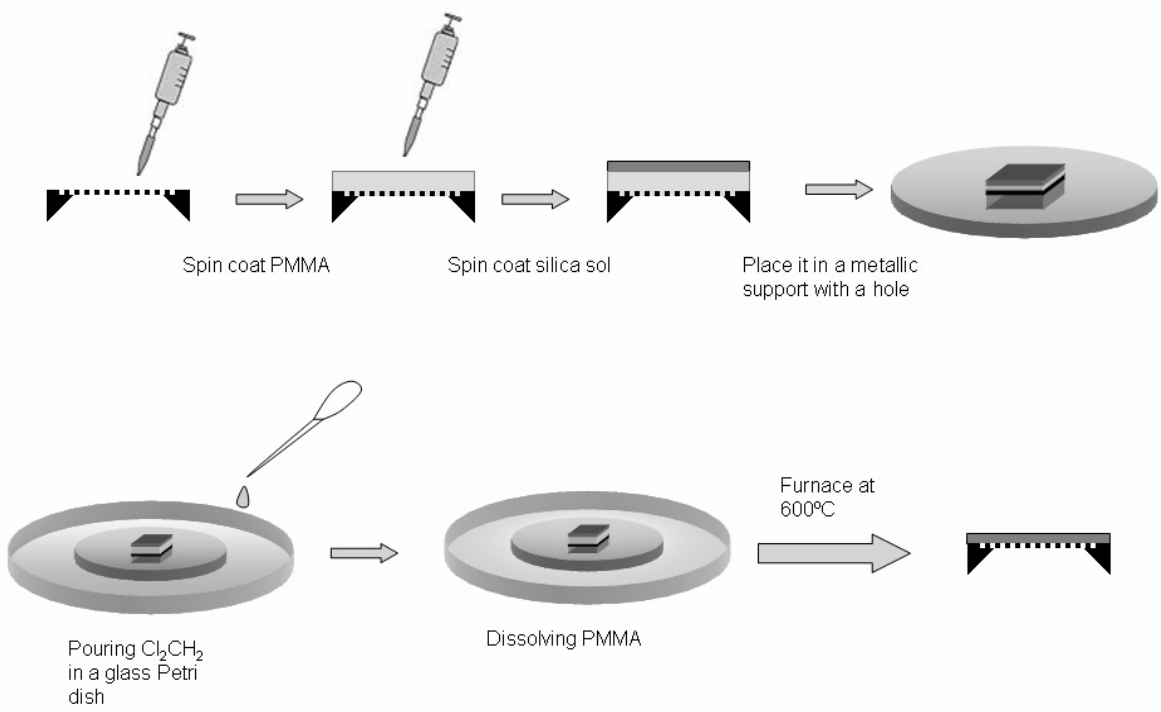

Figure 9.2 Scheme showing the procedure used for depositing self-standing silica membranes on high permeable porous microsieves.

We infiltrated the perforations with a polymeric solution of appropriate viscosity. A solution containing 10 wt% polymethylmethacrylate (PMMA, M_w=120 kg/mol) in acetyl acetone with a viscosity of 3.8 cP at 25 ºC was found

to be optimal. Solutions with a lower viscosity did not fill the pores properly, while more viscous solutions were comparatively thicker and harder to remove in later processing stages. Prior to infiltration, the microsieves were oxygen-plasma treated to remove residual organics. This improved the homogeneity of the PMMA film. PMMA was deposited by spin-coating 100 µl of polymer solution at 2000 rpm for 120 s. After drying, the deposition step was repeated. The microsieve was then heated to 80 ºC for 15 min to evaporate the solvent completely. In the next step, 50 µl of silica sol was spin-coated at 2000 rpm for 60 s and dried overnight in a furnace at 50 °C to allow condensation of the sol. This increased the coherence of the silica film and avoided crack formation in the next step. This procedure yielded a 100-200 nm thick silica membrane, which is noticeably thinner than the width of the perforations of the sieve. In the next step, the PMMA phase was removed by dissolving it in dichloromethane (Merck) [11]. To this end, the microsieve was placed on a metallic disk with a small hole which was located below the sieve. The hole provided entrance for the solvent to dissolve PMMA from the bottom up, and avoided unnecessary direct contact and possible flooding of the silica layer by the solvent. The main PMMA layer was dissolved during 20 min at 40 ºC. Residual traces of PMMA were eliminated from the microsieve in the following steps. The membrane was finally annealed in air at 600 ºC for 2 h (heating and cooling rates 0.5 ºC/min). The resulting templated silica layer is shown in Figure 9.1c-d. It has a porosity of ~60% and a pore radius r_p of ~1 nm, as described in Chapter 7.

9.3. Gateable interconnects for microfluidics

These novel membranes are attractive tools to insert in microelectronics or microfluidic devices. As an example, the thin film was used as an electrophoretic gate to demonstrate its potential applicability in microfluidic device technology. Doubly charged methyl viologen ions (MV^{2+}) were

transported through the interconnect under the influence of a concentration gradient and/or an electrical field as driving forces.

The experimental set-up for ion transport experiments is depicted in Figure 9.3. It consists of two halves of a U-shaped tube between which the membrane is clamped. The membranes were positioned in such a way that the oxide layer was in direct contact with the so-called feed side of the membrane. Aqueous electrolyte solutions (250 ml total volume) were added to the feed and receive side cells and both cells were stirred vigorously. The pH was kept constant at 7.2 using phosphate buffer solutions prepared from mono- and dibasic potassium phosphate salts.

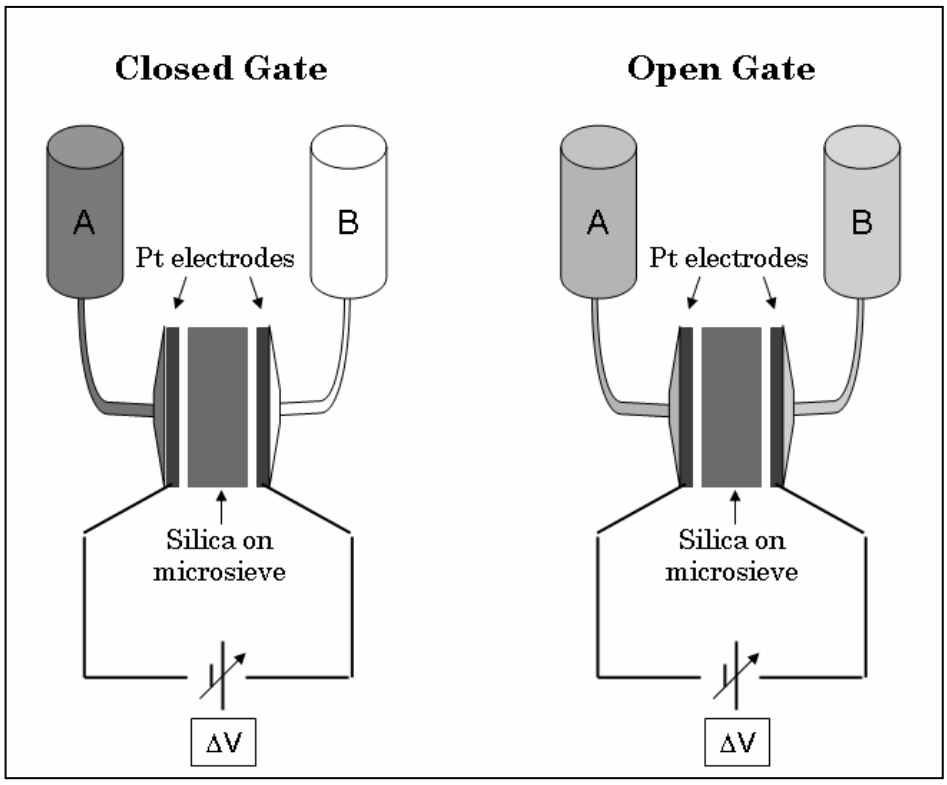

Figure 9.3 Schematic representation of the set-up used for the ion transport experiment. A UV-active methyl viologen (MV^{2+}) or fluorescein (Fl^{2-}) containing solution is placed in vial A. When the gate is kept closed the diffusion of MV^{2+} trough the membrane is blocked. When the gate is open, MV^{2+} can diffuse and/or migrate to vial B.

A dc potential difference ΔV could be imposed over the interconnect using a potentiostat and external Pt gauze electrodes separated by 20 mm. Here ΔV is defined as $\Delta V = V_{receive} - V_{feed}$, with V_{feed} and $V_{receive}$ the electrode potentials at

the feed and receive side, respectively. ΔV was kept between –2 and +2 V to prevent substantial electrolysis of water. All experiments were performed at room temperature. The fluxes were calculated from the concentration changes in the receive side cell B with time, after reaching steady state conditions. Prior to the experiment the membranes were left for 12 h in the receive side electrolyte solution to ensure complete wetting of the oxide layer. Ion transport experiments were carried out with fluorescein Fl^{2-} as divalent anion, and methylviologen (MV^{2+}) as divalent cation. Analysis of MV^{2+} was carried out by UV spectroscopy (Agilent Technologies) at 257 nm.

In the first part of the experiment, methyl viologen dichloride hydrate (98%, Aldrich) was added at the silica side of the membrane to a concentration of 0.77 mM. The influence of electrical field and ionic strength on methyl viologen transport rate was investigated. The results are listed in Table 9.1. In Table 9.1 a negative potential difference over the membrane indicates that the electrode with lower potential was located in the permeate side of the membrane.

At low ionic strength, i.e., I=0.045 M, the diffusional flux of methyl viologen was 17 μmol m^{-2} s^{-1}. When an additional potential difference of –2 V was applied over the membrane, the flux increased by a factor of 4, while almost no flux was observed when the field direction was reversed. This clearly indicates that transport of MV^{2+} through the membrane can be modulated by an external field. The response of the flux on ΔV suggests that the dominant modes of ion transport are Fick diffusion and ion migration.

Table 9.1. Effect of variation of potential difference ΔV and ionic strength I on flux of MV^{2+} ions through the interconnect.

Exp.	I (mM)	κ^{-1} (nm)	ΔV (V)	MV^{2+} flux (μmol m^{-2} s^{-1})
1	45	2.0	–2	66
2	45	2.0	0	17
3	45	2.0	+2	<2
4	1200	0.4	0	146

In another experiment the ionic strength was increased to I = 1.2 M. No field was applied and the concentration gradient remained the same. Nevertheless, the MV^{2+} flux increased by a factor of 8. The increase of flux can be attributed to the vanishing effect of diffuse double layer

overlap, which retarded the translation of charged species inside the pores. The thickness of the double layer can be estimated from the Debye length:

$$(9.1)\ \kappa^{-1} = \sqrt{\frac{\varepsilon k_B T}{2eI}}$$

with ε the permittivity of the solution, k_B the Boltzmann constant, T the temperature, and e the elementary electron charge. Estimated values of κ^{-1} are shown in Table 9.1. When $\kappa r_p > 1$, with r_p the pore radius, the double layer is confined to a small region near the pore wall. This is the case in the experiment with high ionic strength. The centre of the pore was electrically uncharged and both anions and cations could diffuse freely. However, when $\kappa r_p < 1$, as was the case in the other experiments, the dimensions of the pores approach the length of the double layers and double layer overlap occurs from opposite sides of the pore. Under these conditions the pore becomes less permeable for ions. Ions of the same charge are rejected, while those with opposite charge are accumulated inside the pore. However, the latter ones are retarded in their mobility due to attractive interactions between the probe and the pore wall. At pH 7, silica is negatively charged, so the membrane should be predominantly permeable to cations. This prediction is in agreement with the fact that we observed no significant transport of negatively charged fluorescein ions (fluorescein disodium, Fluka) through the membrane under conditions of double layer overlap at pH 7.

In summary, free-standing sol-gel thin films deposited on silicon nitride microsieves can be used as tunable gates for the selective permeation of ions in fluids, thus they are potentially functional component in certain types of microfluidic devices.

9.4. Defects in the silica layer

The above described preparation protocol allowed deposition of templated silica films on microsieves with a high degree of reproducibility. The single gas permeation experiments reported on page 133 of Chapter 7 were carried out

with three of these devices to show that they can be employed in principle to separate gases and to asses the absence of defects in the silica layers. The microsieve-supported silica membranes were glued with a silicone-based glue to a steel disk with the same dimensions as the α-alumina disk used for ceramic membrane fabrication. The disk had a hole to host the microsieve and to allow the gas permeating from one side of the disk to the other, via the microsieve. The single-gas permeation measurements were performed on the same set-up as used for the characterization of ceramic disk membranes. H_2, He, CH_4, and O_2 were used as probes. A flux proportional to the (molecular mass)$^{-0.5}$ would be an indication of the absence of defects in the templated silica thin film.

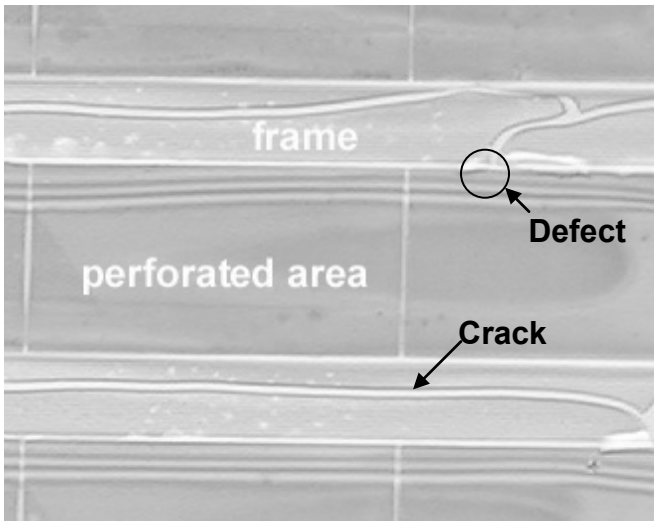

Figure 9.4. Optical microscope picture of a templated silica layer on a microsieve A possible defect of the silica layer is evidenced on the edge of the microsieve perforated area.

Hydrogen permeabilities up to 10^{-5} mol·Pa^{-1}·m^{-2}·s^{-1} were measured; however Knudsen-type selectivity was never reached in any of these experiments. Analyses by optical microscopy did not reveal any defects on the perforated areas. However, occasionally, the templated silica layers cracked on locations directly above the frame mechanically supporting framework of the microsieve, as shown in Figure 9.4. Generally these cracks run along the direction of the frame of the microsieve and they do not influence the selectivity of the membrane, since the effective permeating membrane surface area is located on the perforations of the microsieve. However, at some locations the cracks in the silica layer reached an area below which the support was perforated. This is indicated in Figure 9.5. As a consequence, a few perforations were probably not covered by the silica layer. Since gas separation is very sensitive for defects, the devices did not show gas selectivity.

9.5. Conclusions

A methodology to deposit free standing sol-gel thin films on silicon nitride microsieves was developed, and its potential applicability as a functional component in certain types of microfluidic devices was demonstrated. Single-gas permeation experiments revealed the presence of defects in the layers. However, the density of defects in the silica layers was low, as indicated by the fact that the membranes were functional as mesoporous layers in the liquid phase ion transport experiments. The cracks in the microporous layers were probably located on non-perforated areas of the microsieve. Hence, they may have been formed as a result of the uneven dissolution of PMMA, or during calcination because of the low adhesive strength of the silica layer on silicon nitride. For this reason it is most likely that these cracks can be avoided by further development of the procedure used to clean the microsieves before coating and deposition of the PMMA layer.

9.6. References

[1] S. Kuiper, C.J.M. van Rijn, W. Nijdam, M.C. Elwenspoek. J. Membr. Sci., 1998, 150, 1-8.

[2] R. Schmuhl, W. Nijdam, J. Sekulic, S. Roy Chowdhury, C. J. M. van Rijn, A. van den Berg, J. E. ten Elshof, D. H. A. Blank,. Anal. Chem., 77 (2005) 178.

[3] R. Schmuhl, J. Sekulic, S. Roy Chowdhury, C. J. M. van Rijn, K. Keizer, A. van den Berg, J. E. ten Elshof, D. H. A. Blank, Adv. Mater., 16 (2004) 900.

[4] M. Hashizume, T. Kunitake. Soft Matter,2 (2006) 135.

[5] J. Jin, Y, Wakayama, X Peng, I. Ichinose. Nature Mater., 6 (2007) 686.

[6] T.-C. Kuo, L.A. Sloan, J.V. Sweedler, P.W. Bohn, Langmuir, 17 (2001) 6298.

[7] T.-C. Kuo, D.M. Cannon jr., M.A. Shannon, P.W. Bohn, J.V. Sweedler, Sensors Actuators A, 102 (2003) 223.

[8] J.J. Tulock, M.A. Shannon, P.W. Bohn, J.V. Sweedler. Anal. Chem., 76 (2004) 6419.

[9] S. Roy Chowdhury, R. Schmuhl, K. Keizer, J. E. ten Elshof, D.H.A. Blank, J. Membrane Sci., 225 (2003) 177.

[10] V. Boffa, J.E. ten Elshof and D.H.A. Blank, Microporous Mesoporous Mater. 100 (2007) 173.

[11] Q. Hang, D.A. Hill, G.H. Bernstein.J. Vac. Sci. Technol. B, 21 (2003) 91.

CHAPTER 10

Conclusions and recommendations

The asymmetric structure depicted in Figure 1.2 on page 4 represents a typical silica membrane for gas separation. Such membranes enable, for example, the separation of hydrogen from methane with extremely high separation factors. Thanks to the stacked layer structure it is possible to operate these gas selective films which have a thickness of a few tens of nanometers, in gradients of several bars of pressure difference. The state of the art silica membrane reached its pinnacle in 1998 when De Vos reported the fabrication of pure silica membranes with a H_2/CH_4 ideal separation factor > 4000 at 200 °C, and hydrogen permeances in the order of 10^{-6} mol·Pa^{-1}·m^{-2}·s^{-1} (R.M. de Vos, H. Verweij, Science, 279 (1998) 1710).

Despite their good performance in separating gas mixtures, microporous ceramic membranes have not found industrial use yet. This is because microporous silica membranes have some intrinsic limitations, which make them unattractive for real applications. These limitations were already mentioned in preceding chapters in this thesis:

1. Microporous silica membranes act as extremely effective molecular sieves by retaining the largest molecules of mixtures. However, in some separations the chemical properties of the gases, rather than their dimensions, should be exploited to enable separation.
2. Microporous silica membranes have limited hydrothermal stability; this limits their use to the separation of dry gases, while most of the relevant industrial processes imply the presence of high pressure steam.
3. Not many materials are suitable to be incorporated into a structure as represented in Figure 1.2. The coating of the mesoporous interlayer is problematic. The applied sol for a mesoporous layer should have some specific viscoelastic properties in order not to crack during deposition, consolidation and calcination. Furthermore, the size of the sol particles should be really well defined. The sol that is applied on α-alumina should have particles large enough to no penetrate into the underlying macropores.

4. The macroporous supports are usually made of α-alumina. Stainless steel is rarely used instead of alumina These supports are expensive compared to polymeric supports, so that their introduction in large industrial processes is generally difficult. On the other hand, these supports cannot be fabricated easily with a membrane surface area below 10^{-4} m^2, so that they cannot be used in the emerging lab-on-a-chip technologies.
5. The support, which is some millimeters thick, often poses a resistance to hydrogen flow which is of the same order of magnitude as the resistance of the selective top layer. Hence, the support resistance to gas flow presents an intrinsic upper limit to the realization of more permeable membranes.

In Chapter 3 of this thesis it was shown how specific CO_2 retention was achieved by introducing Nb^{5+} ions into a microporous silica framework by sol-gel synthesis. The modification of separation selectivity of these niobia-silica membranes suggests the screening of aliovalent ions other than Nb into the silica matrix to promote specific molecular separations. Such doped silica thin films may have catalytic properties, thus they could be applied in catalytic membrane reactors as combined separating layer and catalyst.
The introduction of specific functionalities in membranes will surely be of importance for this field. This can be done not only by doping silica with transition metal ions, but also by introducing metallic nanoparticles in silica to enhance its hydrogen permeability, or by creating hybrid organic-inorganic materials. Due to the huge number of organic moieties that could be included in the silica matrix, this specific subject will receive increasing attention in the next years; even if these hybrid material cannot reach the same high temperatures as the pure inorganic membranes because of the sensitivity of the organic moieties.

In hydrothermal conditions the microstructure of amorphous microporous silica has a tendency to change into the thermodynamically more stable denser state. The data presented in Chapter 6 showed that the hydrogen flux trough a

silica layer reduced by about 73% after exposure to 0.56 bar of steam for 70 h at 150 °C. Slower kinetics of densification were observed in the NS membrane. In that system a hydrogen flux reduction of 5% was observed after exposure to the same experimental conditions. However, a reduction of 32% in hydrogen flux was observed after further exposure to 0.56 bar of steam for 70 h at 200 °C. Substantial densification of microporous silica occurs on a time scale of hours and of niobia-silica in a time scale of days. Commercialization of ceramic membranes requires stability on a timescale of years. In view of the results obtained in this thesis, it is improbable that this can be achieved simply by doping.

Hydrothermally stable membranes can presumably be prepared by using crystalline materials like zeolites. In this case the microporosity is an intrinsic property of the crystalline structure. The cavities of zeolites are commonly 0.5-0.6 nm, larger than pure silica membranes. The acidic sites of zeolites can be used for specific separations. Despite that, it is difficult to prepare thin layers made of zolites, due to the impossibility to grow single crystals on large surface areas. For this reason zeolite membranes are commonly prepared as multicrystalline films that are hydrothermally grown on mesoporous supports. It is difficult to cover the surface area of a membrane with a zeolite layer thinner than 1 μm and hence they are generally more resistive than pure silica layers.

The preparation of hydrothermally stable microporous thin films is probably the most critical issue to be solved in order to realize commercially feasible microporous membranes.

In Chapter 7 it was shown that a polymeric sol, which was made of silica nanoparticels, can be coated on 80-90 nm larges pores, simply by varying its rheological properties. The method presented in Chapter 7 allowed the preparation of a templated silica membrane directly on macroporous α-alumina in a facile way. However, due to the penetration of silica particles in the support, the prepared layers were not more hydrogen permeable than

γ-alumina.

In Chapter 9, a method was presented to cover about 1 μm wide pores with a self-standing silica film. A sacrificial polymeric layer was used and no penetration was observed. Thin layers prepared according to the method described in Chapter 9, do not permit gas separation yet, due to the presence of a small number of defects. Despite that, this flexible method allowed to overcome the structure represented in Figure 2.1. No interlayer was used in the membrane separation and the resistance of the support to the gas flow was negligible, because of the high perforation density and the modest perforation thickness (~ 1 μm).

The method presented in Chapter 9 for the deposition of templated silica can in principle used for a large number of materials, since the coating is performed on a dense polymeric sacrificial layer and thus particle size is not so important as it is when the coating is performed on a porous layer. Also the material of the perforated layer (here silicon nitride) can in principle be replaced by a ceramic material or by a polymer that is not soluble in the solvent in which the sacrificial layer is removed. In principle, the deposition method described in Chapter 9 can satisfy a large number of fabrication requirements. For this reason, these microsieve supported membranes can be used in a large number of applications: sensing, microreactors, microfluidic devices, etc….

In future this method could be tested for supports with larger perforations than the one used here. These should have an even lower resistance to gas flow. Thinner films can be applied with the same method, and microporous materials could also be made. However, from the technological point of view, it will be also important to maintain sufficient mechanical strength in the deposited film. This is function of film thickness and perforation width.

In Chapter 4 and 5, it was shown that SAXS is a powerful technique for screening a large number of samples. However, R_g and D_f are mean values of a

distributions of particles with different sizes and fractal dimensions. The polydispersities of these samples cannot be obtained from the experimental data, nor can any information on the chemical homogeneity of the composition of the cluster be extracted. In Chapter 3 a different composition between the NS sol and the NS membrane was reported. This was attributed to the presence of unreacted or poorly condensed silicon oxide species in the NS sol, which were drained into the support upon dipcoating. These species are not detectable by SAXS. Hence, the full characterization of metal oxide sols will require the use of more techniques to asses all components of a sol. For instance, dynamic light scattering (DLS), mass spectroscopy, and NMR could be used together with SAXS to get a full chemical and microstructural characterization of a sol.

Acknowledgements

At the end of this thesis I would like to acknowledge my promotor, Professor Dave Blank, and my supervisor, Dr. André ten Elshof, for their guidance during these four years. I would like to thank all the colleagues of the IMS group: I am sure this is one of the best research groups to work in. I would like to express my deepest thanks to Ruben, Niels, Riaan and Hessel for their contribution to the work reported in this thesis.

These four years in the Netherlands have been a great experience for me not only from a scientific point of view. Thus, I just want to thank all the friends for making my stay in the Netherlands as enjoyable as it was.

Un grande grazie a Domenica e Maurizio.